# EXPERIMENTAL STUDIES ON 2D FLUID SYSTEM

by

**Ildoo Kim**

M.S in Physics, Yonsei University, Seoul, Korea, 2004

B.S in Physics, KAIST, Daejeon, Korea, 2002

Submitted to the Graduate Faculty of

the Department of Physics and Astronomy in partial fulfillment

of the requirements for the degree of

Doctor of Philosophy

University of Pittsburgh

2011

UNIVERSITY OF PITTSBURGH

DEPARTMENT OF PHYSICS AND ASTRONOMY

This dissertation was presented

by

Ildoo Kim

It was defended on

December 7, 2010

and approved by

Xiao-Lun Wu, Ph.D, Department of Physics and Astronomy

David Jasnow, Ph.D, Department of Physics and Astronomy

Jeremy Levy, Ph.D, Department of Physics and Astronomy

Vladimir Savinov, Ph.D, Department of Physics and Astronomy

Stephen Garoff, Ph.D, Department of Physics, CMU

Dissertation Director: Xiao-Lun Wu, Ph.D, Department of Physics and Astronomy

**EXPERIMENTAL STUDIES ON 2D FLUID SYSTEM**

Ildoo Kim, PhD

University of Pittsburgh, 2011

A von Kármán vortex street is two rows of counter-rotating vortices which is observed behind an obstacle in a uniform flow. In two-dimensional soap films, laminar vortex streets were generated using obstacles of various shapes. The Strouhal number $\text{St} = fD/U$, where $f$ is the shedding frequency, $D$ is the size of the obstacle and $U$ is the mean flow speed, is measured and compared to a recently proposed St-Re relationship, $\text{St} = 1/(A + B/\text{Re})$, where the Reynolds number $\text{Re} = UD/\nu$, where $\nu$ is the kinematic viscosity of the fluid. Our measurements show that in the asymptotic limit ($\text{Re} \to \infty$), $\text{St}_\infty = 1/A \simeq 0.21$ is constant independent of rod shapes. This suggests that the potential flow is dominant at high Re and that the potential flow around different shaped rods are all strongly affected by the dipolar field. Another coefficient $B$, which is connected to the thickness of the boundary layer, remains shape-dependent, indicating that for intermediate Re, the St-Re relation is effected by the geometric shape of the rod.

An interaction between a soap film and a droplet is also studied. When a micron-sized water droplet impacts on a soap film with speed $v_i$, there exists a critical impact velocity of penetration $v_C$. Droplets with $v_i < v_C$ merge and flow with the film after impacts, whereas droplets with $v_i > v_C$ tunnel through it. In all cases, the film remains intact despite the fact that the droplet radius ($R_0 = 26\,\mu\text{m}$) is much greater than the film thickness ($0 < h \lesssim 10\,\mu\text{m}$). The critical velocity $v_C$ is measured as a function of $h$, and interestingly $v_C$ approaches a non-zero value $v_{C0} \simeq 520\,\text{cm/s}$ in the limit $h \to 0$. This indicates that in addition to an inertial effect, a deformation or stretching energy of the film is required for penetration.

# LIST OF TABLES

# LIST OF FIGURES

ix

**PREFACE**

First, I would like to offer my gratitude to Dr. Xiao-Lun Wu, who patiently guided me throughout my study. I remember my fourth or fifth day in the group when he was teaching me an experiment. He made a vortex street on a soap film, then turned to me and asked: "Isn't it beautiful?" I confess that it was not beautiful at all in my eyes on that day. After four years of his guidance, however, I now fully appreciate its beauty.

I am grateful to Dr. Walter Goldburg for his valuable advice. As I worked in his lab, I learned much from him - not only physics but also perseverance. I thank other committee members. The work could not be complete without their constructive criticisms. I thank past and present group members for numerous help that they offered: Dr. Yonggun Jun, Dr. Mahesh Bandi, Dr. Matthew Shtrahman, Dr. Suddhashil Chattopadhyay, Dr. Tuan Tran, Tuba Altindal, Li Xie, Rory Cerbus and Aaron Meyer, Thanks!

I thank my Korean friends in Pittsburgh, Changsoo, Seunghwan, Min Kyung, Junsung, Sangeun, Yun Seong, Judong, Kwang Won and many others, for walking together this long way of degree-seeking and encouraging me to stay on track. I deeply thank Eunice, who has been my best friend since we met, especially for teaching me some statistics and helping me to have some life. Finally, I thank my parents and sister in Korea for their enduring support and encouragement.

# List of Symbols

**Chapter 1, 3, 4**

| | |
|---|---|
| $A, B$ | Parameters in Roushan-Wu St-Re relation |
| $a, b$ | Parameters in Rayleigh's St-Re relation |
| $a', b'$ | Parameters in Williamson's St-Re relation |
| $U$ | The typical velocity scale |
| $D$ | The typical length scale |
| $W$ | The width of a rod facing the flow |
| $H$ | The height of a rod |
| $r_a$ | The aspect ratio, $r_a \equiv H/D$ |
| $f$ | The shedding frequency |
| $\eta$ | The viscosity |
| $\nu$ | The kinematic viscosity |
| St | The Strouhal number, $\mathrm{St} \equiv fD/U$ |
| Re | The Reynolds number, $\mathrm{Re} \equiv UD/\nu$ |
| $\mathrm{Re}_C$ | The onset of the vortex street |
| $\mathrm{Re}_{C2}$ | The onset of the type 2 vortex street |
| $v_{st}$ | The velocity of a vortex street in Eulerian frame |
| $c$ | $v_{st}/U$ |
| $h$ | The transverse spacing between vortices |
| $\lambda'$ | The longitudinal spacing between vortices |
| $y$ | The downstream distance |
| $y_0$ | The expansion length scale of the vortex street |
| $\lambda$ | $\lambda'$ when $y \to \infty$ |
| $\lambda_0$ | $\lambda'$ when $y \to \infty$ and $D \to 0$ |
| $\alpha$ | $\lambda/D$ when $D \to \infty$ |
| $s_i$ | The distance from the rod to where the potential region that separates two rows of a vortex street appears |
| $\Delta s$ | The length of the potential region that separates two rows of a vortex street |

| | |
|---|---|
| $\delta$ | The boundary layer thickness |
| $M$ | Mach number |
| $\phi$ | The potential function |

## Chapter 2

| | |
|---|---|
| $\rho_a$ | The density of air |
| $\rho_w$ | The density of water |
| $R_0$ | The radius of the droplet |
| $m$ | The mass of the droplet |
| $h$ | The thickness of a soap film |
| $\sigma$ | The surface tension |
| $l_x$ | The distance between the droplet injection point to the film |
| $v_i$ | The impact velocity |
| $v_C$ | The critical velocity |
| $E_C$ | The critical energy, $E_C \equiv \frac{1}{2}mv_C^2$ |
| $E_{min}$ | $E_C$ when at zero film thickness |
| $v_x, v_y$ | The velocity of the droplet after the impact |
| $V_F$ | The flowing speed of the soap film |
| $\varepsilon$ | $v_y/V_F$ |
| $C_S$ | The soap molecule concentration |
| $g$ | The gravitational acceleration |
| $v_t$ | The terminal velocity |
| $v_w$ | The wave propagation speed |

## Chapter 5

| | |
|---|---|
| $W$ | The width of a soap film |
| $\tau$ | The coarse graining time unit |
| $\tau_0$ | The sampling time interval |
| $m$ | The length of a subset to be compared |

## 1.0 INTRODUCTION

One of the fundamental difficulties of the fluid dynamics is that the governing equation, the Navier-Stokes equation, is hardly solvable. The Navier-Stokes equation is, in a non-dimensional form,

$$\frac{\partial \vec{v}}{\partial t} + (\vec{v} \cdot \nabla) \vec{v} = -\nabla p + \frac{1}{\text{Re}} \nabla^2 \vec{v}, \tag{1.1}$$

with Reynolds number $\text{Re} = UD/\nu$, where $U$ and $D$ are characteristic velocity and length scales in the system and $\nu$ is the kinematic viscosity. There are two complicating factors in the equation. The first is the nonlinearity. The inertial term $(\vec{v} \cdot \nabla) \vec{v}$, originated from the momentum transport, is proportional to $v^2$, and this nonlinearity makes the equation complex and mathematically difficult to solve. The other difficulty is that when Re is high, i.e., the viscosity effect is much smaller compared to the inertia effect, the equation becomes a *singular* perturbation problem.

A perturbation theory is usually characterized by a small parameter in the problem. In a regular perturbation theory, as the small parameter gets smaller, the solution approaches to the solution that is acquired by setting the small parameter to zero. In contrast, in a singular perturbation problem, the solution acquired by setting the parameter at zero is not accurate. This usually happens when the coefficient of the highest order derivative is such a small parameter. For example, an initial value problem [49]

$$\varepsilon \frac{du}{dx} + u = x \tag{1.2}$$

with a boundary conditions $u(0) = 1$ can be considered. This ordinary differential equation has an exact solution

$$u(x) = (1 + \varepsilon)e^{-x/\varepsilon} + x - \varepsilon. \tag{1.3}$$

In the limit $\varepsilon \to 0$, an approximate solution of Eq. (1.2) can be obtained by setting $\varepsilon$ to zero. When $\varepsilon \ll 1$ and $x \gg \varepsilon$, the approximate solution $u(x) = x$ may be considered as a good approximation,

however it does not satisfy the boundary condition. For $x \sim O(\varepsilon)$, the "inner" solution must be considered. Such a solution can be obtained by rescaling $x$ to $x/\varepsilon$ and writing the equation as

$$\frac{du}{d(x/\varepsilon)} + u = \varepsilon \frac{x}{\varepsilon}. \tag{1.4}$$

In this case the right hand side of the equation can be ignored and the solution is $u = e^{-x/\varepsilon}$.

The exact solution is compared to two approximated solutions in Fig. 1. The singular perturbation problem is usually associated with multiple regions of variables. In the example above, the "outer" region where $x > \varepsilon$ and the "inner" region where $x < \varepsilon$ are very well separated, and the approximations are different in different regions.

Equation (1.1) is a second order differential equation whose highest order derivative is the viscous damping term $\frac{1}{\text{Re}}\nabla^2 \vec{v}$. When $\text{Re}^{-1} \to 0$ (or the viscosity approaches to zero), the problem becomes a singular perturbation problem. In other words, the viscosity cannot be ignored even though it is diminishingly small. This was articulated in the classical literature by Jean le Rond d'Alambert's as a paradox in fluid dynamics [18, 19]. He proved that an incompressible and inviscid fluid flowing past a circular body has symmetric upstream and downstream, thus no drag force on the body, which is in direct contradiction to our observation in daily life. This was solved when Prandtl discovered the boundary layer [55, 49]. He derived the boundary layer equation by rescaling the Navier-Stokes equation with a factor $1/\sqrt{\text{Re}}$. He showed that when a fluid passes by a thin plate, an inviscid solution works only beyond a certain distance from the plate, in other words, outside *the boundary layer*. Within such a boundary layer, viscosity effect cannot be neglected. The flow is separated into two regime. One is near the static surface where the inner solution of the boundary layer equation applies, the other is far from the surface where the inviscid outer solution is valid. This result is striking considering that huge airplanes such as Boeing 747 and Airbus A380 could not be lifted in air without existence of the thin boundary layer ($\sim 10\,\mu$m) between the wing and air.

Here we will discuss a physical phenomenon in which multiple length scales are involved. When a free stream of fluid encounters an obstacle, e.g., a cylindrical rod of size $D$, with a flow speed $U$, various flow patterns are observed downstream depending on Re. When $\text{Re} < 1$, as the inertia effect is not so large compared to the viscous effect, the so-called Stokes flow (or creeping flow) is observed. In this regime, the inertia term in the Navier-Stokes equation can be ignored,

2
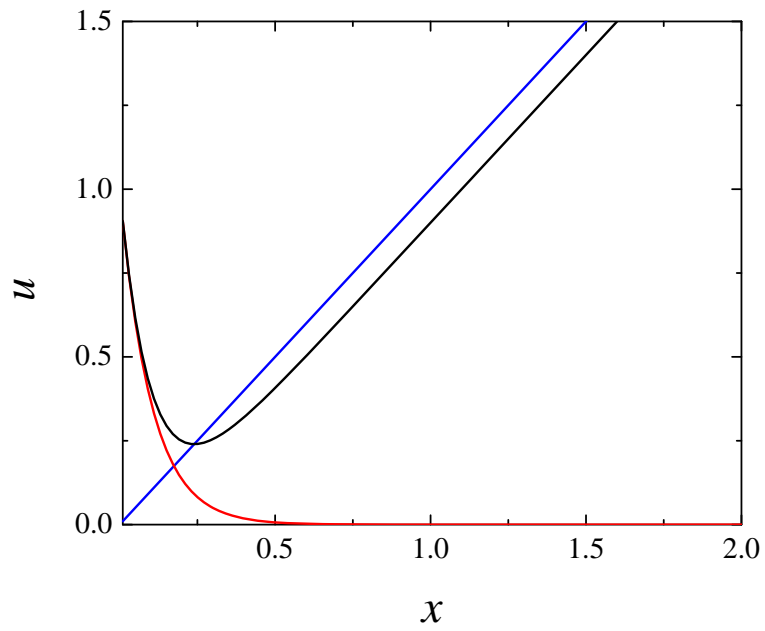
Figure 1: The exact solution of Eq. (1.2) (black) when $\varepsilon = 0.1$. The outer solution (blue) is not accurate when $x \sim \varepsilon$ and does not satisfy the boundary condition. For $x \lesssim \varepsilon$, the inner solution (red) is more suitable.

and the equation can be linearized. Between $10 \lesssim \text{Re} < 50$, a stable pair of vortices is observed in downstream side of the obstacle. In this regime, the separation of the flow occurs about $90°$ from the stagnation point and the flow is stable (see Fig. 2). As Re increases beyond 50, the pair of vortices becomes unstable, and discharged into the flow, forming two staggered rows of counter-rotating vortices. The pattern of the periodic wake in this regime is called von Kármán vortex street, named after a Hungarian physicist Theodore von Kármán.

The study of the vortex street may date back to 19th century. In 1878, V. Strouhal studied Aeolian tone, which is the sound generated by a thin wire moving in air. In the study, he first introduced the Strouhal number $\text{St} = fD/V$, where $f$ is the shedding frequency, $D$ is the size and $V$ is the speed of the wire, and he found that this non-dimensional frequency is independent of $V$ [79]. In 1911, von Kármán [86] observed two staggered rows of vortices behind a cylinder in a flow tank, and in the following year, he performed the stability analysis by assuming that vortices are shed from each sides of the cylinder alternatively and they occupy infinitesimal area in fluid [87]. Considering two infinite rows of pre-deposited point vortices in a perfect inviscid and incompressible fluid, he concluded that only a vortex street with

$$h/\lambda = 0.28, \tag{1.5}$$

would be stable, where $h$ is the distance between two rows and $\lambda$ is the distance between vortices in a row. This so-called Kármán's ratio was compared to experiments, most of which report somewhat larger value between 0.28 and 0.5. The discrepancy may be due to the fundamental limitation of the point vortex model in which a fluid is assumed to be completely irrotational and the vortex street is only characterized by $h$, $\lambda$ and $\kappa$, where $\kappa$ is the strength of individual vortices. Therefore the finite viscosity or a finite vortex patch size must be considered [73, 74].

Inspired by early experimental observations, in 1915, Lord Rayleigh [58] associated the Aeolian tones to the vortex street. Based on a hydrodynamic similarity hypothesis, he postulated that St would only depend on Re. Given that $\text{Re}^{-1} \ll 1$, he wrote a Taylor series expansion in terms of $\text{Re}^{-1}$. He proposed a St-Re relation as the first order correction to St, yielding

$$\text{St} = a\left(1 - \frac{b}{\text{Re}}\right), \tag{1.6}$$
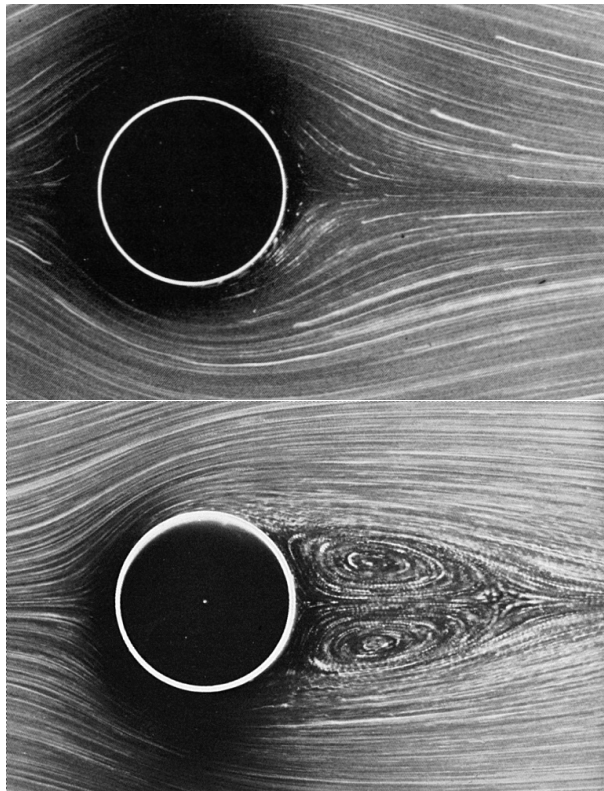
Figure 2: Flow past a cylinder (top) Re=1.54 and (bottom) Re=24. Images are from Ref. [85].

where $a$ and $b$ are constants. After his proposal, $a \simeq 0.2$ and $b \simeq 20$ were determined for a cylinder in three-dimensional (3D) fluids by many experiments among which Roshko's [63] is the one most cited, and Eq. (1.6) has been used for many decades. As experimental techniques became better, more accurate data has been accumulated, and discrepancy between Eq. (1.6) and data has been revealed near the onset of the vortex street. To fill the discrepancy, in 1998, Williamson and Brown [93] and Fey *et al.* [28] independently suggested a St-Re relation using the $Re^{-1/2}$ expansion rather than $Re^{-1}$, hinted by the boundary layer theory. In 2005, another proposed St-Re relation is suggested by Roushan and Wu [67], for circular cylinders in two dimensions (2D),

$$ St = \frac{1}{A + B/Re}, \tag{1.7} $$

where $A$ and $B$ are constants. This relation is based on the observation that the spatiotemporal motion of a vortex street behaves like a wave so that the linear dispersion relation $v_{st} = f\lambda$ holds. Observations also show that such a wave of a vortex street propagates with a velocity $v_{st}$ that is a constant fraction of the mean flow speed $U$, i.e., $c = v_{st}/U$, and has a wavelength that is linear in $D$, the size of the object, with a proportionality constant $\alpha$ and a non-zero intercept $\lambda_0$, i.e., $\lambda = \lambda_0 + \alpha D$. Equation (1.7) then can be obtained with $A = \alpha/c$ and $B = \lambda_0 U/(cv)$. It is noteworthy that when the right-hand side of Eq. (1.7) is expanded, it becomes an infinite Taylor series in $Re^{-1}$, with coefficients that are combinations of $A$ and $B$. In this sense, Eq. (1.6) is the truncation of Eq. (1.7). The most interesting part in these observations is perhaps the relation $\lambda = \lambda_0 + \alpha D$. Here $\lambda_0$ divides the vortex shedding into two regime. One is $D \gg \lambda_0$, where $\lambda \simeq \alpha D$ is a good approximation, and the other is $D \lesssim \lambda_0$, where such an approximation cannot be used. Even though $\lambda_0 \ll \alpha D$ for most of regime, $\lambda_0$ cannot be ignored and is related to the constant $B$. The behavior is reminiscent of the singular perturbation discussed earlier.

In this thesis, we study vortex streets generated using rods of different cross-sectional shapes with a desire to address physical natures of the two coefficients $A$ and $B$ in Eq. (1.7). In chapter 3, we will show that a special parametrizing scheme of length scale $D \equiv \{$the diameter of the circle enclosing the cross-sectional shape of the rod$\}$ gives rise a universal behavior that $A$ is independent of shapes at the high Re. The selection of the definition of $D$ is based on following reasons:

1. The vortex street in 2D soap film can be successfully modeled as an irrotational flow with vortex patches which occupies finite area in fluid[1].

2. As Re increases, such vortex patches become small relative to the rod. When Re is large enough, the effect of vortex patches is localized, allowing us to idealize the system to potential flow past a rod of a certain shape, which is a solution of the Laplace equation with boundary conditions.

3. The solutions of the potential flow past non-circular rods are similar to that of the potential flow past a circular rod and strongly affected by the dipolar field[2].

Thus the apparent universal behavior of $A$ at high Re can be interpreted as the flow being successfully approximated as potential without downstream singularity. In contrast, $B$, which is connected to $\lambda_0$, remains shape-dependent, indicating that for intermediate Re, St-Re relation is effected by the boundary layer whose thickness varies with the geometric shape of the rod.

The study of vortex streets is also important for engineering. Early studies include the practically useful measurements of $C_D$ and $C_W$, the drag coefficient and the base suction pressure, respectively [27, 64, 6, 20]. As the vortex street can be observed at scale from a thin radio antenna to as large as an island in the middle of an ocean, this wake structure became a concern in designing various structures, such as a submarine periscope, overhead electric power lines and skyscrapers [33]. Such importance may be best illustrated by a catastrophic event occurred on November 1st, 1965 in Pontefract, UK. A coal-powered power station, named "Ferrybridge C", had eight cooling towers, arranged in two rows of four. Three of these then the world's largest cooling towers were collapsed by a wind of 85 mph ($\simeq 38\,\mathrm{m/s}$). The towers were supposed to withstand wind speed up to 200 mph. However, unfortunately, this figure was calculated by assuming the wind speed to be static. It was witnessed that the vibration of the towers in the second row, induced by the towers in the first row, produced a high pitched whine [25]. After a formal investigation, it was documented that vortex streets generated by cooling towers in the first row were responsible for the collapse of three towers in the second row [23].

In contrast to the destructive case of the Ferrybridge plant, some creatures on the earth utilized vortex shedding in their favor. In contrast to the case where the trailing vortex street is a source

---

[1]See Appendix C and Ref. [73] for detail.
[2]See Appendix C for detail.

Figure 3: Collapsed cooling towers in Ferrybridge C power plant. On 1 November 1965, the wind of 85 mph was blowing from the right to the left side of the photo.
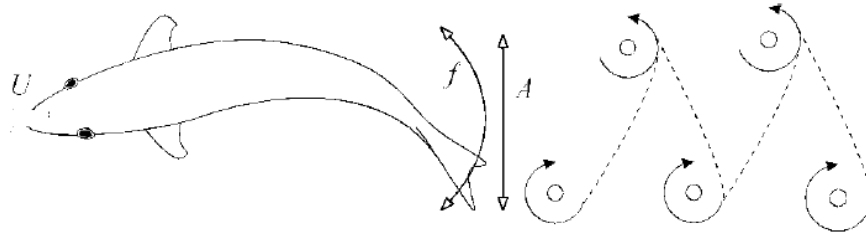
Figure 4: How do fish swim: a fish reverses the rotational direction of the wake behind it by oscillating its fin. The reversed vortex street is associated with thrust generation [76].

of the drag force for a passive object [87], fish create a reversed vortex street by moving their tail fin at a certain frequency range (see Fig. 4) and transforms a drag-producing vortex street to a thrust-producing one [76]. Insects are also known to utilize vortices produced during a stroke of wings in their maneuvering. With recent developments of bio-inspired robots [32], the vortex control became one of important problems in engineering.

As of today, the understanding of the subject still remains incomplete as Roshko pointed out in his review [65]:

> "After over a century of effort by researchers and engineers, the problem of bluff body flow remains almost entirely in the empirical, descriptive realm of knowledge." - A. Roshko (1993)

Understanding of a vortex street is demanding as it is also being a fundamental question in turbulence [51, 38, 56], along with practically significant topics such as vortex induced vibration [94] and vortex control [76, 32].

Throughout the thesis, we used a soap film as a 2D fluid medium. Soap films are practically 2D as their thickness is several microns and much smaller than other dimensions which are some tens of centimeters. In fluid dynamics, both theoretically and experimentally, a 2D fluid does not behave like a mere projection of a 3D fluid. The most notable difference may be that the vorticity is much more persistent in 2D than in 3D. By using a 2D fluid medium, a *laminar* vortex street could be studied over much broader range of Re than achievable in 3D.

Despite the fact that it is only recently that soap films have been exploited as a 2D fluid medium for scientific research, such as the investigating of low-dimensional turbulence [46, 5, 89] and wake

structures [68], soap films have been studied for many years due to their appealing appearance. There have been many theoretical and experimental studies of their physical properties, including Mysels' early investigation of marginal regeneration [47] and Lucassen's earlier theoretical work [44, 14]. These studies provided crucial insight about soap films and allow them to be used in scientific purposes, but some problems, like the stability of the film, are yet to be understood. We raise an interesting question about how the film would react upon an external impact. In a similar context, the feasibility of large liquid films in space was speculated about by Zheng and Witten [99]. Using an energy analysis that is introduced by Taylor and Michael [83], they concluded that such a film may be very fragile as even a meteor of a hundred nanometer in size can potentially be hazardous to it. In contrast, the recent observation [16] shows that a big object, such as a tennis ball, can pass through a micron thick soap film without breaking it, indicating that the simple energy analysis would not be appropriate in describing such a physical process.

In chapter 2, we will present the experimental data showing that a liquid droplet of radius $26\,\mu$m can tunnel through soap films of thickness less than $10\,\mu$m without breaking the film. To explain this "tunneling" process, the deformation of a soap film must be taken into account. We also show that experimental data are hardly understood without assuming that the droplet captures a finite portion of the soap film and increases its mass. The observation may be also crucial to applications such as a gene gun [43] and a lab-on-chip device [24].

## 2.0 TUNNELING OF MICRON-SIZED DROPLETS THROUGH SOAP FILMS

### 2.1 INTRODUCTION

When a liquid droplet impinges on a surface of liquid or solid, a variety of phenomena occurs. When a droplet is falling on the surface of the same liquid, that has a finite but large depth, the impact causes splashing, creating a crown-like structure that had become an iconic piece of Edgerton's then newly invented strobe photography in the late 30's [22]. If the impact velocity is not fast enough to produce a splashing, the droplet is merged into the underlying liquid as a van der Waals force brings two free surfaces closer and the surface tension minimizes the surface area of the coalesced liquid. The coalescence is delayed when the underlying bath of liquid is vertically oscillated at a high acceleration [15]. In this case, the lubrication effect by the interstitial air between two free surfaces produces a lift force that would postpone or even prevent the coalescence.

When the droplet impacts the surface of solid, we also observe splashing. If the solid surface is smooth, a similar corona structure is observed. The dynamics of corona formation is related to the ambient air. A study shows that the corona structure is strongly suppressed under low air pressure [97]. If the surface is rough, the splashing occurs at the contact line rather than forming a corona [96]. If the surface is hydrophobic, the bouncing of the droplet is also observed [60].

When the droplet impacts a thin layer of liquid on a solid substrate, the macroscopic corona structure disappears altogether and instead a thin ejecta sheet is created [84]. The existence of such ejecta sheets has only recently been discovered and has captured the attention of scientists [36]. Underlying this seemingly simple phenomenon is complex dynamics [36, 90], whose understanding is currently incomplete.

Studies of these phenomena were strongly motivated by their importance for a variety of industrial processes such as containment of hazardous liquids, uniform coating of surfaces, and efficient

Figure 5: Milk drop coronet, H. E. Edgerton, 1939

fuel injection. In this chapter, we report a related phenomenon, namely the impact of a water droplet against soap films. Specifically, we are interested in tunneling of a ballistic droplet through the film. A classical analysis of Taylor and Michael [83] based on an energy argument suggests that when a hole is created on a liquid film, it will shrink and heal if its diameter is smaller than the film thickness. On the other hand, if the diameter is larger than the thickness, an instability that leads to the rupture of the film will occur. Analyses were also carried out by Zheng and Witten [99] in a proposal to create a giant liquid film in space that is free of gravitational forces and surrounding air; both are significant factors complicating the study of two-dimensional fluid flows and turbulence using these films in ground-based experiments [13, 46, 89]. Their calculation shows that a meteor of a few nanometer in size can be hazardous to a space-based film. While the energetic argument is compelling and has found some experimental confirmations [42], the calculation cannot account for certain observations made in these films. For instance, common experiences show that when a soap film is perturbed by a foreign object, the film often breaks. However, if the object is wetted by water, the film is much more resistant to the perturbation. A recent experiment demonstrated that a

macroscopic object as large as a tennis ball can pass through a micron-thick film without breaking it [16]. It is evident that the passage dynamics in this latter case cannot be understood unless film deformation into the third dimension, perpendicular to the film, is taken into account.

To investigate the tunneling process quantitatively we implemented an inkjet technique to generate uniform sized ($R_0 = 26\,\mu$m) water droplets at a controllable rate. The trajectories of the droplets before and after impacts were digitized using a high-speed video camera, allowing quantitative measurements of momentum and energy transfers between the droplets and the film. It was observed that droplets can tunnel through the soap film if its impact velocity is higher than a certain threshold value $v_C$, and in no case rupture occurs as a result of the impact. Using films of different thicknesses ($0 < h \lesssim 10\,\mu$m), we found that the energy barrier $E_C = \frac{1}{2}mv_C^2$ for tunneling is a linear function of $h$ and can be expressed as $E_C = E_{min}(1 + \alpha h/R_0)$, where $E_{min} \simeq 0.01$ erg and $\alpha \simeq 3.9$ are constants. Kinematically, we found that the tunneling process can be modeled as an inelastic collision between the droplet and the film. It only requires two parameters, $M_1$ and $M_2$, which specify respectively the effective mass of the film involved in the collision and the mass that is transferred to the droplet after the collision.

## 2.2 EXPERIMENTS

### 2.2.1 Soap films

Experiments were carried out using vertically flowing and static soap films, which were discussed in previous publications [70, 69] and in the Appendix. Briefly, a vertically flowing soap film channel is constructed using two parallel nylon wires, whose two ends are tied together (see Fig. 6). Wires are connected to two soap solution reservoirs, one at the top (R1) and the other at the bottom (R2) of the channel. The top reservoir feeds the channel with soap solution, whose composition will be discussed later. The solution flux, $F_S$ is regulated by a valve (V) at the top of the channel. The soap solution is recollected at the bottom reservoir, and then pumped back to the top reservoir at the pumping flux $F_P$. To maintain the depth of the solution at the top and the bottom reservoir to be constant, any excess amount of solution at the top reservoir is returned to

the bottom one through an independent tubing. Since this returning flux $F_R = F_P - F_S$, the net flux toward/outward either reservoir is zero, resulting in a long-lasting film once initiated.

To create a soap film, we first let the soap solution flow along the two vertical wires by squeezing them together, and then we separate the wires from each other to form a film. The channel width $W$ can be varies by adjusting the tension applied to four auxiliary nylon wires which are connected to the main wires. We set $W$ to be constant at 5 cm. By regulating the solution flux $F_S$, the film flowing speed $V_F = F_S/(Wh)$, where $h$ is the thickness of the film, can be varied. For the vertical film, there is a strong correlation between the flowing speed $V_F$ and the film thickness $h$, i.e., both $V_F$ and $h$ increase with $F_S$, but we measured $V_F$ and $h$ independently, using a fast video camera and a laser transmission interferometer[1], which will be described below. With the current setup, $2.5 < h < 10\,\mu$m can be achieved corresponding to $1.5 < V_F < 2.5$ m/s. Note that in our current setup, $h$ and $V_F$ are related.

In the vertical soap film, the velocity of the film is uniform across the spanwise direction, with the exception near the nylon wires, where shear layers exist. For this reason, the thickness of the film is not uniform near the nylon wires, i.e., the film is thicker near the wire. A previous study [95] shows that such non-uniformity is strongly localized near the wires. All of our measurement were made in the middle of the soap film channel where $h$ is uniform (see Ref. [95]) on scales much greater than the droplet radius $R_0$.

A large flowing soap film was not stable for $V_F < 1.5$ m/s (or $h < 2.5\,\mu$m). Thus, for measurements with thin $h$, we generated smaller static films by immersing a thin rectangular metal frame $(3 \times 3\,\text{cm}^2 \times 50\,\mu\text{m})$ into the soap solution and then pulling it out slowly. The soap films formed in this manner were initially thick, but they were subject to thinning due to gravity. For $h < 2.5\,\mu$m, the film was quasi static ($V_F \lesssim 0.02$ m/s) with $h$ varying slowly with time, and we monitored $h$ by a laser transmission interferometer[2]. Compared to flowing soap films, static soap films can be made much smaller and thinner. With the metal frame we described above, we could easily generate soap films with $h < 1\,\mu$m.

To determine the film thickness $h$, we measured the optical transmittance of the $p$-polarized light $T_\perp$ at $\lambda = 685$ nm as a function of incident angle $\theta$ of a semiconductor laser. A rotation

---

[1]A laser transmission interferometer is suggested and tested by Mr. Roushan who worked with the Wu research group in 2005. The instrument is constructed in a help of his documentation.

[2]Color of the film is also indicative of $h$.

14
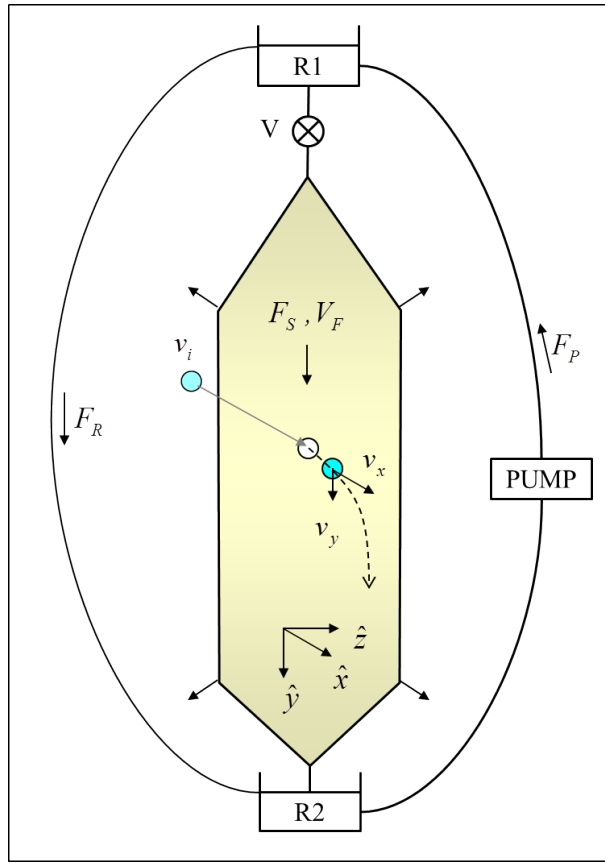
Figure 6: The experimental setup. The soap-film channel is formed by two nylon wires, and the width of the channel is maintained by four side wires (four thin arrow attached to the film) as depicted in the figure. The soap solution is injected into the film through a valve (V) from the top reservoir (R1), and recollected at the bottom reservoir (R2) and pumped back to the top. The net flux is zero at any arbitrary point of the channel, thus a long-lasting film was implemented. A vertical soap film flows in the $\hat{y}$ direction with a uniform velocity $V_F$. A water droplet is ejected horizontally, in the $\hat{x}$ direction, toward the soap film with an impact velocity $v_i$. The final velocity of the droplet after impact ($v_x$, $v_y$) is also indicated. To visualize the water droplet and the film, a high-intensity halogen lamp and a low-pressure sodium lamp were used. The droplet's trajectories and their corresponding velocities were recorded by a high-speed video camera. Similar measurements were also performed in static vertical films created in a rigid metal frame with a surface area $3 \times 3 \, \text{cm}^2$.

stage was built to allow the laser and a photo-diode to be rotated synchronously on two separate arms. A computer controlled stepping motor drives the rotation stage, allowing a wide range of incident angle to be scanned rapidly, i.e., $-70° \leq \theta \leq +70°$ in $\sim 5\,\text{s}$. We modeled the soap film as a dielectric slab of thickness $h$ with a refractive index $n = 1.33$. A calculation shows that $T_\perp$ is given by [29]

$$T_\perp = \left[1 + \left(\frac{2r_\perp}{1-r_\perp^2}\right)^2 \sin^2\left(\delta/2\right)\right]^{-1}, \tag{2.1}$$

where $r_\perp = \frac{\cos\theta - \sqrt{n^2 - \sin^2\theta}}{\cos\theta + \sqrt{n^2 - \sin^2\theta}}$ and $\delta = \frac{4\pi h}{\lambda}\sqrt{n^2 - \sin^2\theta}$. As shown in Fig. 7, this slab model works quite well for our soap films, and $h$ can be accurately determined.

The soap solution used consists of 2% (in volume) liquid detergent (Dawn) and 98% distilled water. The kinematic viscosity of the soap solution, measured by a glass capillary viscometer (Cannon Instrument Co.), is $\nu \simeq 0.012\,\text{cm}^2/\text{s}$, close to water. The surface tension of the liquid/air interface of the bulk solution was determined by a Du Noüy tensiometer (CSC Scientific) as $\sigma = 32 \pm 1\,\text{erg/cm}^2$.

Measurements of $\sigma$ as a function of the concentration of the liquid detergent $C_S$ (in volume) is shown in Fig. 8. The figure shows that as $C_S$ increases (as we add more soap), $\sigma$ rapidly decreases from $72\,\text{erg/cm}^2$ of pure water to $32\,\text{erg/cm}^2$ at 0.03%. Further addition of soap does not lower $\sigma$, indicating that the critical micellar concentration of our soap solution is well below 0.1%. As will be discussed below, a wave speed measurement in the soap film indicates that the surface tension of the film is about the same as measured on the free surface of the bulk soap solution, indicating that at 2% concentration, the surfaces of the film are fully covered by the surfactant.

### 2.2.2 Making small droplets

Micron-sized water droplets are created by using an inkjet printer cartridge (NEC model #30-060). This cartridge works by electrically heating water near a nozzle (Diam.=$40\,\mu$m), which consists of a small heater with a $30\,\Omega$ internal resistance. Using a custom-made computer program, we generated a train of Transistor-Transistor Logic (TTL) pulses, which is 5 V for $10\,\mu$s and repeated periodically with a frequency 10 Hz. TTL pulses are amplified by a custom-made current driving circuit (see Fig. 9), so rectangular electric pulses of 7.5 V were applied to the heater for $10\,\mu$s. Each electric pulse delivers $\left(V^2/R\right)\delta t \simeq 190\,\text{erg}$ to the heater.
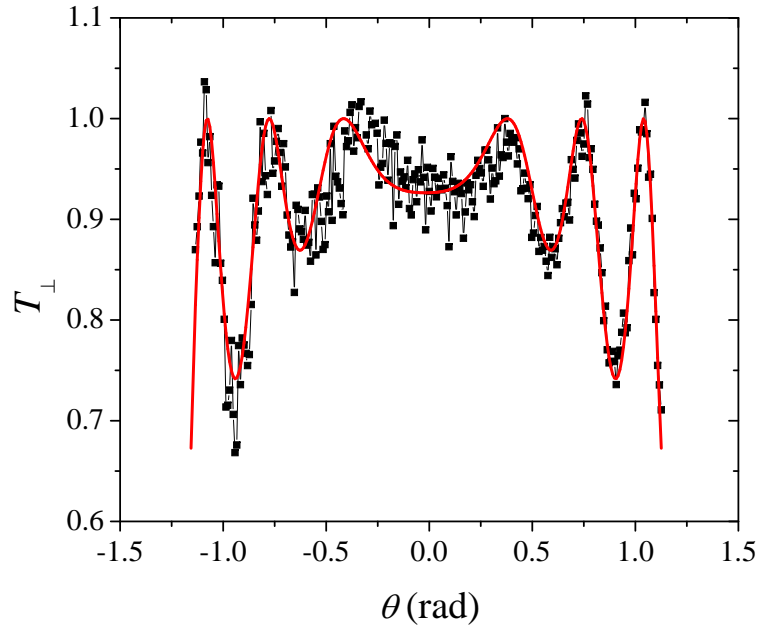
Figure 7: A typical optical transmittance measurement in a flowing film. The data (squares) show transmittance $T_\perp$ as a function of the incident angle $\theta$. We found that a soap film can be well approximated by a dielectric slab with a constant thickness $h$ and a refractive index $n = 1.33$. This allows $T_\perp$ to be calculated rigorously. The solid line is a fit to the slab model of Eq. (2.1), resulting in $h \simeq 2.56\,\mu$m in this case.
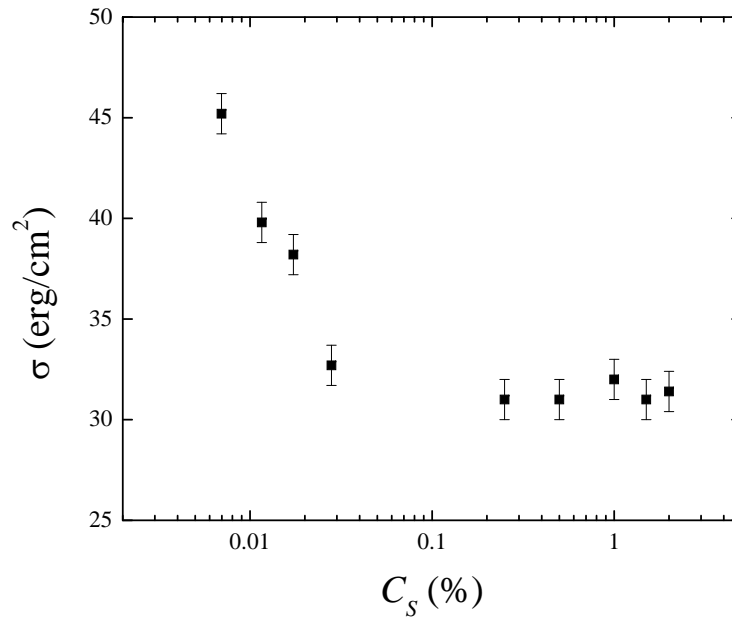
Figure 8: The surface tension of soap solution $\sigma$ vs. the soap concentration $C_S$. Here $C_S$ is the volume fraction. Without surfactant, $\sigma \sim 72\,\text{erg/cm}^2$ is measured by Du Noüy tensionmeter. As soap is added to water, $\sigma$ drops drastically. Already at 0.03 %, the surface tension of soap solution and air interface reaches to its asymptote value $\sim 32\,\text{erg/cm}^2$.
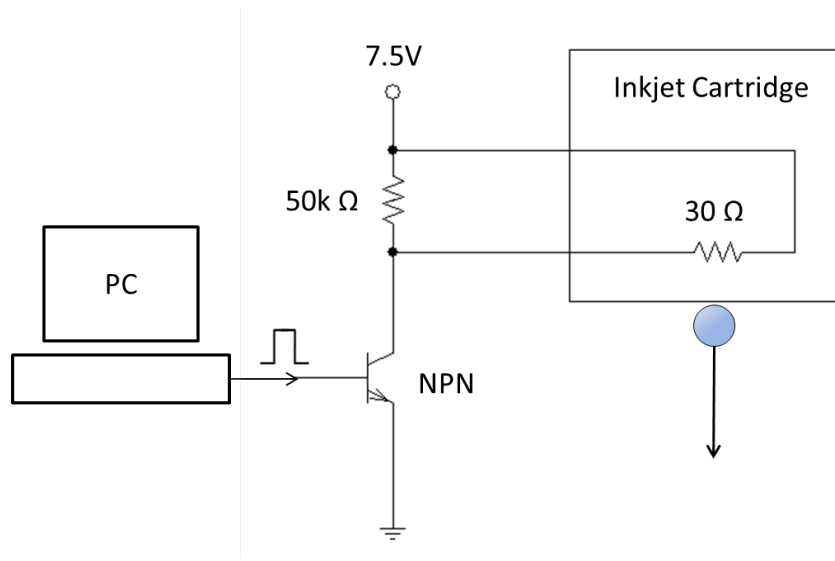
Figure 9: A circuit diagram to generate a droplet using an inkjet cartridge. A TTL pulse from a PC is amplified by an NPN transistor. As a result, a rectangular electric pulse of $7.5\,\mathrm{V}$ is applied to the heater for $10\,\mu\mathrm{s}$. The pulse is repeated periodically with a frequency $10\,\mathrm{Hz}$.

To characterize the system, droplets were injected horizontally inside a chamber which shields the droplets from the air flow. As air friction rapidly damps their motion, the droplets reached a terminal velocity $v_t = 7.6 \pm 1.1\,\mathrm{cm/s}$ within $20\,\mathrm{ms}$. For a small Reynolds number in air, $\mathrm{Re}_a(\equiv 2v_tR/v_a) < 1$, $v_t$ of a sphere is given by $v_t \simeq \frac{mg}{6\pi\eta_a R}$, where $\eta_a$ and $v_a$ are respectively the shear and the kinematic viscosity of air. This yields a droplet radius of $25.4 \pm 1.7\,\mu\mathrm{m}$. Independently we measured the droplet radius by weighing the cartridge before and after ejecting $9 \times 10^4$ droplets. The decrease in the cartridge mass, averaged over several trials, was $6.5 \pm 1$ mg. This gives the average mass per droplet $72 \pm 11$ ng or a radius $R = 26 \pm 1$ $\mu$m, which is in good agreement with the $v_t$ measurement. The difference of 2.5% between the two methods may be due to evaporation during the $20\,\mathrm{ms}$ flight time in air, but this difference is barely discernible. In what follows, we will use $R_0 = 26\,\mu\mathrm{m}$ as the radius of our droplets.
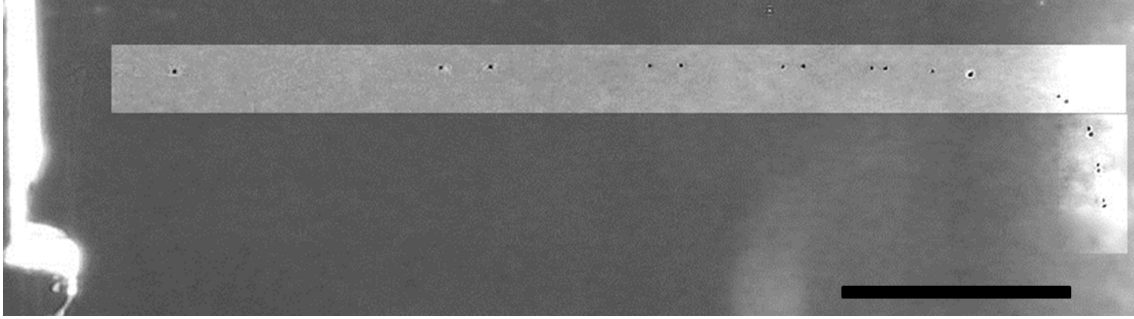
Figure 10: Trajectory of a droplet injected horizontally from the cartridge. The image's contrast is adjusted for better presentation. Trajectory of a droplet has been digitized using two strobe light sources. Here 19 strobes were applied at time $t =$0.3, 2.2, 2.5, 4.4, 4.7, 6.6, 6.9, 8.8, 9.1, 10.9, 12.7, 21.8, 23.6, 32.7, 34.5, 43.6, 45.4, 54.5, 56.3 ms. Initially it travels horizontally, however it is subjected to a strong damping and quickly ($t < 20$ ms) loses the horizontal momentum. In the vertical direction, due to gravity, it is accelerated and reaches the terminal velocity $v_t = 7.6$ cm/s. The scale bar is 1 cm.

### 2.2.3 Setup

To study the interactions with a soap film, a stream of droplets generated by the inkjet nozzle was aimed normal to the film. For convenience of a latter discussion, a coordinate system is set up such that the initial velocity is along the $x$-axis and the film flows in $\hat{y}$ direction as depicted in Fig. 6. To visualize the droplet's trajectory, a high-intensity (300 W) halogen lamp and a high-speed video camera (Phantom V5, Vision Research) were mounted perpendicular to $xy$-plane facing each other, so we can capture forward scattering from the droplet and follow their motions. In typical measurements, the camera operates at 5000 fps with a resolution $256 \times 512$, allowing droplet velocity to be determined reliably.

In the experiment, the impact velocity $v_i$ was varied by adjusting the distance $\ell_x$ between the nozzle and the film. The particle trajectory remained horizontal for a distance of $\sim 5$ cm before noticeable bending took place. Therefore all of our measurements were restricted to $\ell_x < 5$ cm. For instance, at the critical velocity $v_C \simeq 520$ cm/s, $\ell_x$ was approximately 2.5 cm, and the vertical

20

velocity component was only 1 % of $V_F$ and thus negligible. After the collision, the droplet either tunnels through with a non-zero $v_x$ or is absorbed by the film with $v_x = 0$. We measured the velocity components $(v_x, v_y)$ after tunneling as a function of $v_i$ and the film thickness $h$.

## 2.3 RESULTS AND DISCUSSIONS

### 2.3.1 The existence of the critical velocity $v_C$ and the momentum transfer in $\hat{x}$ direction

Figure 11(a) displays the horizontal velocity component $v_x$ of the droplets after the impact on a soap film as a function of $v_i$. The measurements were repeated for films of different thicknesses $h$. We showed that there exists a critical velocity $v_C$; for $v_i < v_C$, the droplet loses its horizontal momentum ($v_x = 0$) and it flows with the soap film after impact. On the other hand, for $v_i > v_C$, the droplet is able to tunnel through the film with $v_x > 0$. Although the data near the threshold is somewhat noisy, the critical velocity $v_C$ can be determined without much ambiguity by extrapolating the data below and above the threshold. As delineated in Fig. 12(a), our measurements indicate that $v_C$ increases with $h$, suggesting that the energy barrier for tunneling becomes greater for a larger $h$. We also found that $v_C$ does not vanish when $h \to 0$ but approaches a finite value $v_{C0} \sim 520\,\text{cm/s}$, which translates to a minimum energy $E_{min} (\equiv \frac{1}{2}mv_{C0}^2) \simeq 0.01\,\text{erg}$. This suggests that a considerable fraction of the tunneling energy $E_C$ is in the deformation of the soap film. Another conspicuous feature seen in Fig. 11(a) is that after tunneling, $v_x$ is proportional to the impact velocity $v_i$, and the proportionality constant is, to a good approximation, unity for all different $h$.

### 2.3.2 Momentum transfer in $\hat{y}$ direction

The momentum exchange in the vertical direction is also significant. Figure 11(b) displays normalized $y$-component velocity $v_y/V_F$ as a function of the impact velocity $v_i$. It is shown that if $v_i < v_C$, $v_y/V_F = 1$, i.e., the droplet moves with the film. However, for $v_i > v_C$, the tunneling causes the droplet to gain a momentum in the $\hat{y}$ direction, but in general $v_y < V_F$. We give the $y$-component of velocity in terms of $\varepsilon = v_y/V_F$. Figure 11(b) demonstrates that $\varepsilon$ is nearly constant in each regime (merging and tunneling) but changes abruptly at $v_c$. In addition, $\varepsilon$ depends on the film thickness

21
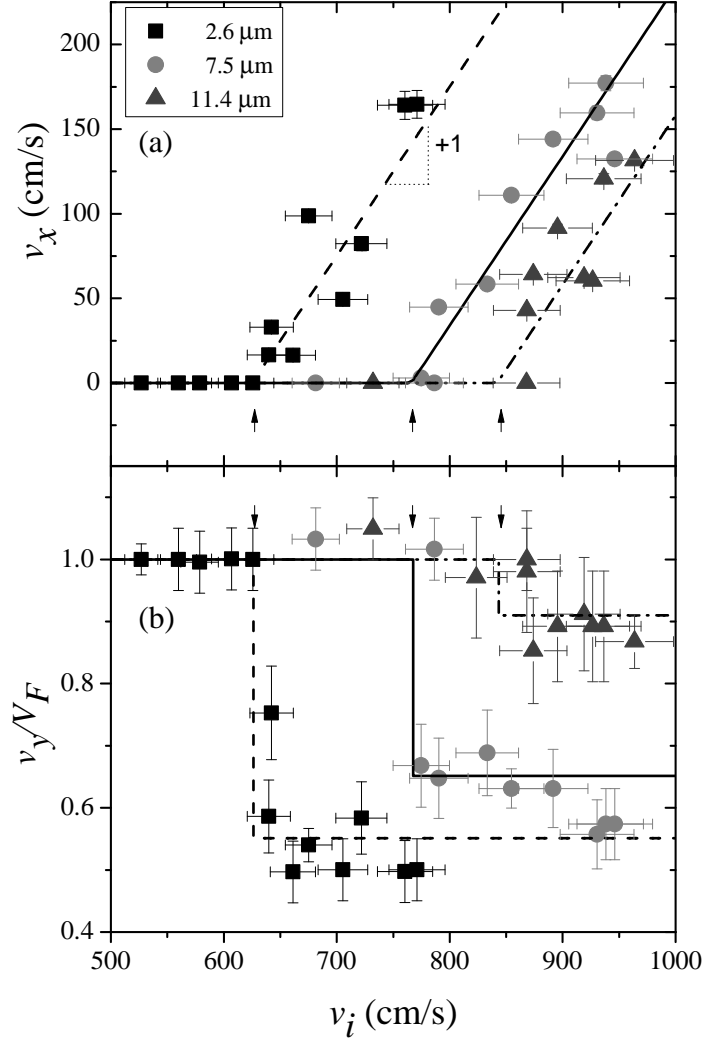
Figure 11: The droplet velocity $(v_x, v_y)$ after impact as a function of the impact velocity $v_i$. The measurements were carried out for different film thicknesses: $h = 2.6$ $\mu$m (squares), 7.5 $\mu$m (circles), and 11.4 $\mu$m (triangles). The error bars represent the measurement uncertainties, mostly due to the finite pixel size. In (a), the x-component of the velocity $v_x$ is plotted against $v_i$. It is shown that there exists a critical velocity $v_C$ for each film thickness as indicated by the vertical arrows. In (b), the normalized y-component of the velocity $v_y/V_F$ is plotted against $v_i$. Here we found that $v_y/V_F$ has two discrete values for a given $h$. It is either +1 when the droplet merges with the film, or $\varepsilon \leq 1$ when the droplet tunnels through the film.

22
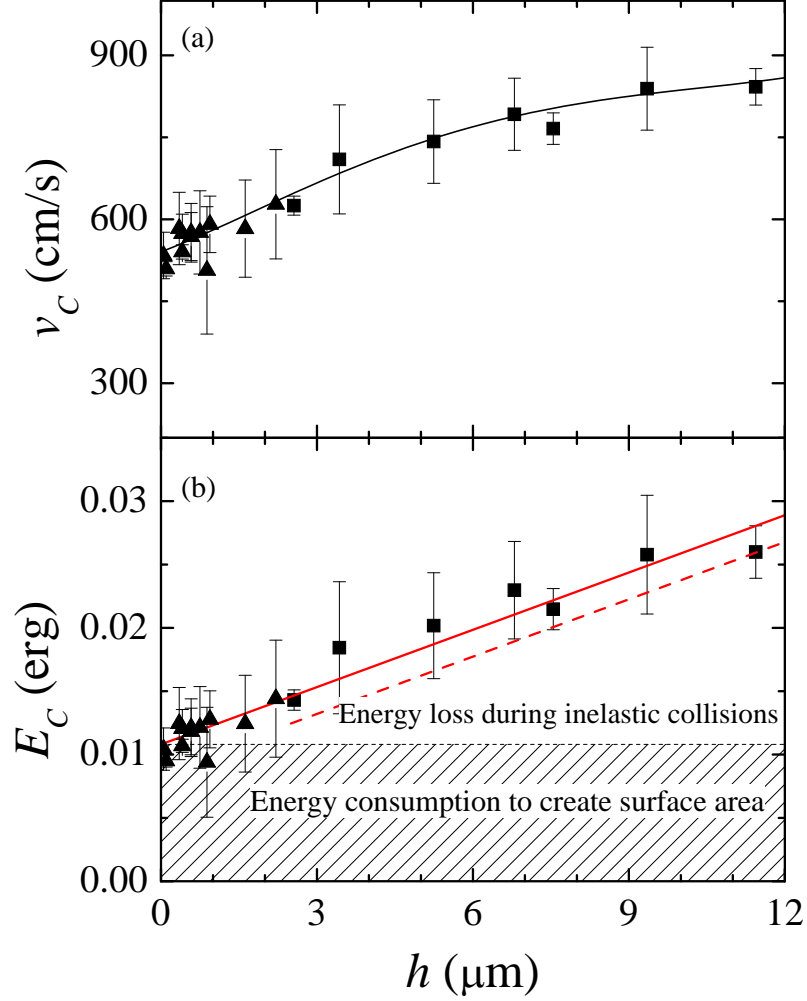
Figure 12: (a) The critical velocity $v_C$ and (b) the energy barrier $E_C \equiv \frac{1}{2}mv_C^2$ vs. the film thickness $h$. In both plots, the triangles and squares are for static and flowing soap films, respectively. It is shown that $E_C(h)$ is approximately linear in $h$, but it does not vanish as $h \to 0$, indicating that a finite film deformation energy is required for tunneling. The solid and the dotted lines are calculations based on Eq. (2.10) and Eq. (2.9) (with $V_F = 2.5\,\text{m/s}$), respectively. See text for more details.

$h$ as delineated in Fig. 13. When the droplet passes through a thicker film, it gains more momentum in the $\hat{y}$ direction than passing through a thin one. Asymptotically, one expects that $\varepsilon \rightarrow 1$ as $h \rightarrow \infty$, which is consistent with our observation. We found that a tunneling droplet readily picks up the $y$-momentum from the film. For instance, at the current experimental condition, $v_y$ is $\sim 60\%$ of $V_F$ for a film as thin as a few microns and is $\sim 90\%$ for $h \simeq 10\,\mu$m.

### 2.3.3  Deformation and wave propagation

To understand the physical origin of the energy barrier in the tunneling process, we examined the impact dynamics using fast video imaging with the film illuminated by a monochromatic sodium lamp. Figures 14(a)-(d) display four consecutive images of a droplet shortly after it had impacted on a soap film of $h = 4\,\mu$m. The time interval between the images was fixed at 0.26 ms. Here, the droplet as well as its mirror image on the soap film are clearly visible. Also visible in (b) is a scar created by the droplet, but the scar disappeared in (c), indicating that its lifetime is less than 0.26 ms. Because of the short length and time scales involved, we believe that the scar region is associated with strong vorticity, which dissipates energy. The use of the monochromatic light also allowed us to observe waves created by the impact. Here, the wavefront appears as a dark band in (b) that propagates radially outward. In Figs. 15(a)-(d), another sequence of images is captured at intervals of 0.2 ms with the camera normal to the surface of the soap film. Here the droplet is merged with the film because it impacts the film at the velocity lower than $v_C$. The merging droplet is visible as a dark spot at the center of the circular wavefront and is carried downstream by the film. As it moves downstream, the wavefront propagates radially outward at a constant velocity $v_w$. By investigating images such as ones in Fig. 15, the wave speed $v_w$ on the soap film can be determined as a function of $h$, which is displayed as solid squares in Fig. 15(e). The figure shows that $v_w$ increases rapidly as $h$ decreases; for a small thickness, $h < 1\,\mu$m, $v_w$ can be as large as 10 m/s. A liquid film in general can support two different types of waves, known as the symmetric and the anti-symmetric waves [82]. For the symmetric wave, the two surfaces of the film move out of phase with respect to each other, and is also called peristaltic mode of oscillations [see Fig. 16(b)]. For the anti-symmetric wave, both surfaces undulate in phase [see Fig. 16(c)]. In the absence of surfactants (like soap molecules), the restoring force of both waves are due to the
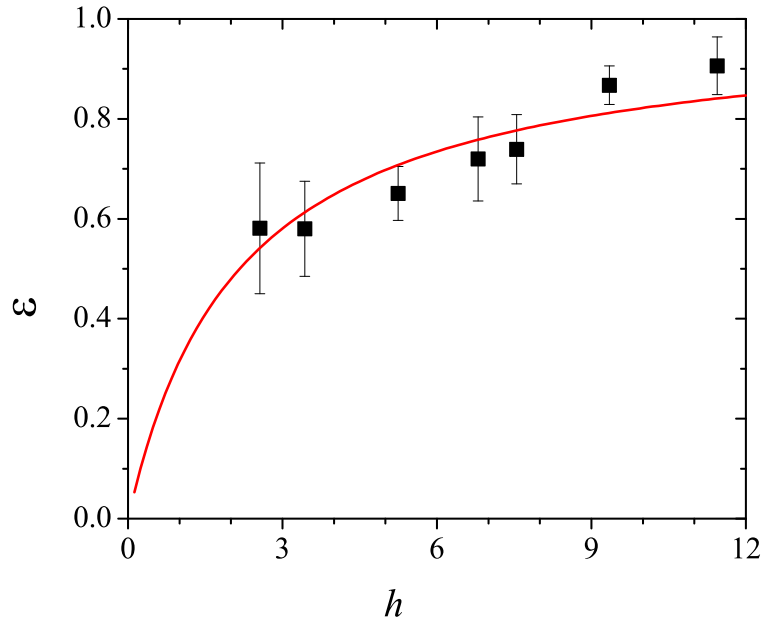
Figure 13: The normalized vertical velocity after tunneling $\varepsilon = v_y/V_F$ vs. the film thickness $h$. It is observed that as $h$ increases, $\varepsilon$ becomes larger, indicating that the droplet gains a linear momentum in the $\hat{y}$ direction. Asymptotically, $v_y \to V_F$ (or $\varepsilon \to 1$) as $h \to \infty$ as expected. The solid line is a calculation based on Eq. (2.11) derived from an inelastic collision model.

surface tension $\sigma$ but the dispersion relations are different for the two cases because of different mass distributions in the film. The anti-symmetric wave is non-dispersive with a constant velocity given by $v_a = \sqrt{\frac{2\sigma}{\rho_w h}}$, and the symmetric wave, on the other hand, is dispersive with a velocity $v_s = k\sqrt{\frac{\sigma h}{2\rho_w}}$ that depends on a wave number $k$. Since $v_s/v_a = kh/2$, it is expected that $v_a \gg v_s$ in the long-wavelength limit. In the presence of surfactants, the restoring force for the symmetric mode is dominated by the surface (or Marangoni) elasticity $E \equiv A\frac{d\sigma}{dA}$, where $A$ is a surface area, instead of $\sigma$. It is shown by Lucassen [44] that in the long-wavelength limit, the elastic wave is also non-dispersive with a propagation speed $v_e = \sqrt{\frac{2E}{\rho_w h}}$. In our soap film therefore there is a degeneracy in that both the anti-symmetric capillary wave and the symmetric elastic wave are possible, and both scale with the film thickness as $h^{-1/2}$. We found that our experimental data in Fig. 15 can be well described by the mathematical form $v_w = \sqrt{\frac{2c}{\rho_w h}}$ (see the inset), where $c$ is an adjustable parameter. Using $\rho_w = 1\,\text{g/cm}^3$, a fitting procedure yields $c \simeq 32.7 \pm 2.6\,\text{erg/cm}^2$, which matches very well with the surface tension measurement ($\sigma = 32\,\text{erg/cm}^2$) using the Du Noüy ring method. Thus, unless it is an amazing coincidence, where Marangoni elasticity $E$ is nearly identical to $\sigma$ for our soap film, we believe that the dominant wave mode in the film created by the droplet impact is the anti-symmetric wave.

### 2.3.4 Film structure near the impact point

At the impact point [see Fig. 14(a)], it is observed that the droplet deforms the soap film locally, forming a cylindrical pouch a few droplet diameters long. Because of smallness of the droplet and fast dynamics, it was not feasible to follow the spatiotemporal evolution of the cylindrical pouch. However, inspections of a large number of video images reveal that the longest pouch is $\sim 4R_0$, indicating that in order to tunnel through, the soap film must be stretched into a long cylinder with an excess surface area of $\sim 14\pi R_0^2$, where $R_0$ is the radius of the water droplets. A naive calculation using $\sigma = 32\,\text{erg/cm}^2$ indicates that this corresponds to a surface energy of $9.5 \times 10^{-3}\,\text{erg}$. Considering the Marangoni effect, we expect that the energy requirement may be greater.

A question that arises naturally is what determines the maximum length of the cylinder. A related phenomenon is the Plateau-Rayleigh instability where a uniform circular jet of fluid breaks
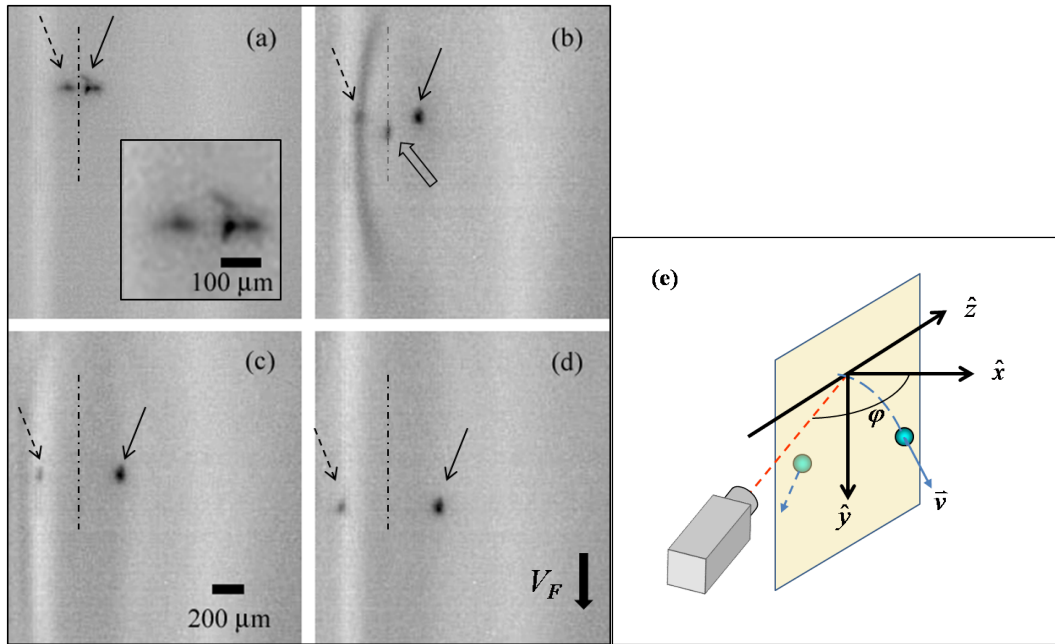
Figure 14: The tunneling dynamics of a water droplet. The sequence of video images (a)-(d) were taken at times $t = 0$, 0.26, 0.52, and 0.78 ms with the resolution of $256 \times 256$ pixels. The coordinates in (e) are the same as in Fig. 6, and the droplet and its mirror image on the film are depicted by two droplets. The camera was set at an angle $\varphi \simeq 75°$. The penetrating droplet and its mirror image are clearly visible in (a)-(d) and are indicated by the pair of arrows. The dash-dotted lines in (a)-(d) depict the plane of reflection. As a function of time, the droplet-image pair moves together in the vertical direction but apart from each other in the horizontal direction. This allows an alternative means to precisely determine $v_x$ and $v_y$. Shortly after the impact, an elongated dark region can be identified in (a), showing that the film is stretched by the droplet. A moment later in (b), a scar, which is indicated by a large arrow, is left behind in the film. The scar moves with $V_F$, which is faster than the droplet velocity $v_y$. Interestingly, the scar in (b) disappears rapidly and is no longer observable in (c). Also seen in (b) is the surface wave (the dark band) that propagates radially outwards from the impact point. This wave (or the band) is barely seen in (c), but disappears from the view in (d).

27
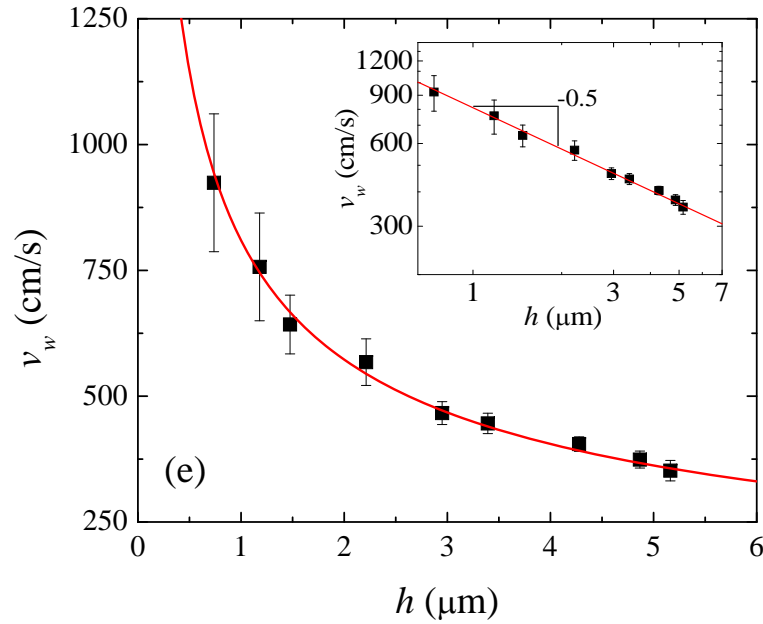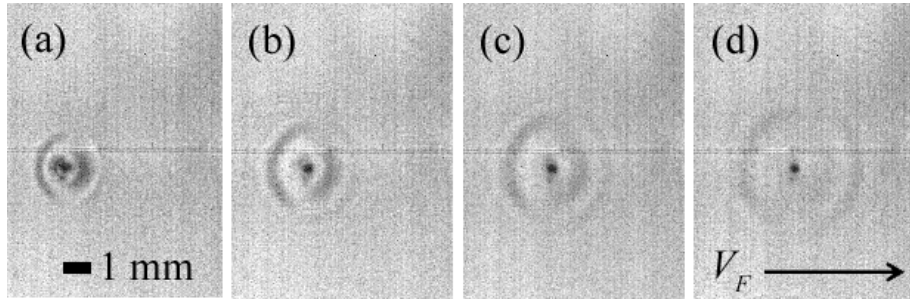
Figure 15: A wave generated by an impacting droplet. Images (a)-(d) were taken sequentially at an equal interval, corresponding to $t = 0$, 0.2, 0.4, and 0.6 ms, respectively. The camera angle is described in Fig. 14(e) with $\varphi \simeq 0°$. The impact velocity of the droplet is less than $v_C$ so that it merges with the soap film. The droplet appears as a dark spot at the center of the expanding circular wavefront. In (e), the wave speed $v_w$ in the soap films is measured as a function of $h$. The scaling relation $v_w \propto h^{-1/2}$ is delineated in the inset, where the solid line is a fit to $v_w = \sqrt{\frac{2\sigma}{\rho_w h}}$.

up into a stream of droplets [10]. For the anti-symmetric undulation to be the dominant mode of oscillations in our soap film, the instability of a cylindrical soap film is similar to the Plateau-Rayleigh problem with the simple modification of replacing the surface tension $\sigma$ by $2\sigma$, due to the presence of two liquid-air interfaces of the film. It follows that the fastest growing wave number $k_{max}$ of the axial undulation is given by $k_{max} \simeq 0.7/R_0$, corresponding to $\lambda_{max}(\equiv 2\pi/k_{max}) \simeq 9R_0$ [10]. We note that our experimentally observed pouch length $4R_0$ is about a half of $\lambda_{max}$, which makes physical sense since the front of the pouch, where the water droplet locates, must be the anti-node and the location of the pinch-off must be the node given by $(n+\frac{1}{2})\lambda_{max}$ where $n = 0, 1, 2, \ldots$. Our observation corresponds to $n = 0$ [see Fig. 16(a)]. This is possible if the pinch-off time $\tau$ is shorter than the stretching time $(\sim \lambda_{max}/2U)$, because otherwise a longer pouch will be produced and it will break in multiple locations, which was not observed. Quantitatively, this scenario also makes sense since according to our measurement the stretching time is $\lambda_{max}/2U \simeq 12\,\mu\text{s}$ and the pinch-off time $\tau$ can be estimated by the growth rate of the Plateau-Rayleigh instability $\tau \equiv \sqrt{\rho_a R_0^3/2\sigma} \simeq 0.52\,\mu\text{s}$. Thus the condition $\tau \ll \lambda_{max}/2U$ is satisfied. The emerging physical picture is that during transmission, a piece of soap film is extruded by the fast moving droplet. At the same time an axial undulation grows rapidly on the stretched cylindrical film, and the cylinder closes off at its base once $\lambda_{max}/2$ is reached. As we will show below, in order to explain the kinematics of the tunneling droplet, a small mass must be transferred from the film to the droplet and the size of such a mass can be determined from our measurements.

### 2.3.5  Calculations

It would be desirable to compare our experimental observations with theoretical predictions. Unfortunately such theory is not currently available. A back-of-the-envelope calculation shows that our measurements were carried out in a hydrodynamic regime where Reynolds number Re $= \frac{2\rho_w R_0 v_i}{\eta_w} \gtrsim 260$ and the Weber number We $= \frac{2\rho_w R_0 v_i^2}{\sigma} \gtrsim 44$ are both large. Thus the kinetic energy or the inertia effect overwhelms energy dissipation and the capillary effect. In the following we propose a heuristic model that can account for some key features of our observations.

It is apparent that when a collision takes place, only a fraction of film mass in the neighborhood of the impact is involved in the interaction. Thus an effective mass $M_1$ and its corresponding size

(a)

$M_1$-$M_2$

$M_2$

$v_y$

$v_x$

$m$

$\sim 4R_0$

(b) symmetric wave

(c) anti-symmetric wave
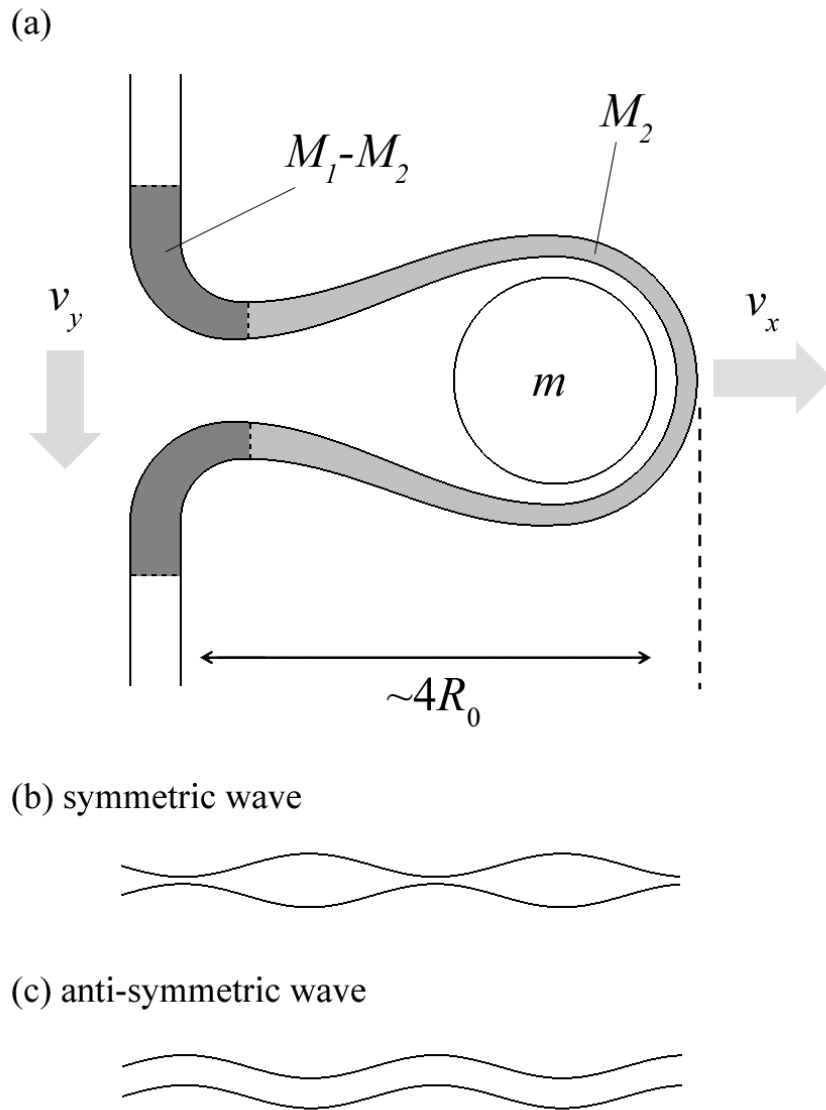
Figure 16: The schematics depicting different conformations of a soap film. In (a), the film is stretched by a ballistic droplet, where $M_2$ will eventually engulf droplet $m$, and $M_1$ provides a $y-$momentum to the droplet. (b) and (c) are two possible wave modes in a soap film.

$R_1 = \sqrt{M_1/\pi\rho_w h}$ may be specified. After the collision, a part of $M_1$, called $M_2$, is transferred to the water droplet, increasing its mass from $m$ to $m + M_2$. The emerging droplet travels with velocity $(v_x, v_y)$ and the remaining mass $M_1 - M_2$ travels along the film with velocity $(v'_x, v'_y)$ [see Fig. 16(a)]. The presence of $M_2$ allows a second length scale $R_2 = \sqrt{M_2/\pi\rho_w h}$ to be specified. We treat our problem as an inelastic collision in which linear momentum is conserved but not energy.

The linear momentum conservation demands

$$mv_i = (m + M_2)v_x + (M_1 - M_2)v'_x, \tag{2.2}$$

$$M_1 V_F = (m + M_2)v_y + (M_1 - M_2)v'_y. \tag{2.3}$$

At the moment of separation, when the dressed droplet $(m + M_2)$ becomes detached from the rest of the film, we expect that $v_x > 0$ but $v'_x \simeq 0$. For the inelastic collision, one also expects $v_y = v'_y$ at the separation point. Solving the above equations, we find

$$v_x = \frac{m}{m + M_2} v_i, \tag{2.4}$$

$$v_y = v'_y = \frac{M_1}{m + M_1} V_F. \tag{2.5}$$

The total kinetic energy $KE_f$ of the droplet and the film after collision is given by

$$
\begin{aligned}
KE_f &= \frac{1}{2}(m + M_2)(v_x^2 + v_y^2) + \frac{1}{2}(M_1 - M_2)(v'^2_y), \\
&= \frac{1}{2}\frac{m}{m + M_2}mv_i^2 + \frac{1}{2}\frac{M_1}{m + M_1}M_1 V_F^2. \tag{2.6}
\end{aligned}
$$

Neglecting the deformation of the film, this is all the mechanical energy of the system (droplet plus the soap film) that remains after the collision. It is clear that the collision is inelastic since

$$
\begin{aligned}
\Delta KE( &\equiv KE_i - KE_f) \\
&= \frac{1}{2}m\left(\frac{M_2}{m + M_2}v_i^2 + \frac{M_1}{m + M_1}V_F^2\right) \geq 0, \tag{2.7}
\end{aligned}
$$

where $KE_i = \frac{1}{2}mv_i^2 + \frac{1}{2}M_1 V_F^2$ is the total kinetic energy of the system before the collision. Physically, $\Delta KE$ is the amount of energy ultimately dissipated by the creation of vorticity in the fluid. Since both $M_1$ and $M_2$ are proportional to $h$, we find that energy dissipation vanish when $h \to 0$. In other words, no vorticity can be created in a very thin film so the physics of tunneling becomes

a purely potential flow problem. For a successful transmission, the energy consideration therefore requires that the initial energy of the droplet should be greater than the sum of the energy dissipation $\Delta KE$ and the film deformation $E_{min}$ with the result: $KE_i \geq \Delta KE + E_{min}$ (or $KE_f \geq E_{min}$). This yields

$$\frac{1}{2}mv_i^2 \geq E_{min}\left(1 + \frac{M_2}{m}\right) - \frac{1}{2}mV_F^2\left(\frac{m+M_2}{m+M_1}\right), \tag{2.8}$$

or the critical energy of the droplet $E_C = \frac{1}{2}mv_C^2$ as:

$$E_C = E_{min}\left(1 + \frac{M_2}{m}\right) - \frac{1}{2}mV_F^2\left(\frac{m+M_2}{m+M_1}\right). \tag{2.9}$$

This equation predicts that the motion of the film ($V_F \neq 0$) lowers the energy barrier of tunneling. For a small $V_F$, e.g., in our experiment $(V_F/v_C)^2 < 0.15$, one may neglect the last term to obtain,

$$E_C \simeq E_{min}\left(1 + \frac{M_2}{m}\right) = E_{min}\left(1 + \frac{3}{4}\alpha_2^2\frac{h}{R_0}\right), \tag{2.10}$$

where $\alpha_2 = R_2/R_0$ is a constant. Equation (2.10) is consistent with our observation in that $E_C$ is linear in $h$ with a finite intercept. Using the known parameters of our soap film ($E_{min} \simeq 0.01\,\text{erg}$ and $R_0 = 26\,\mu\text{m}$), we found $\alpha_2 \simeq 2.2 \pm 0.1$. Interestingly, this value of $\alpha_2$ implies a rather uniform coating of the penetrating droplet by the film of thickness $h$, i.e., $\Delta V \simeq 4\pi R_0^2 h$. In Fig. 12(b) we plot Eq. (2.9) using a dotted line and Eq. (2.10) using a solid line with $V_F = 2.5\,\text{m/s}$. It is seen that the reduction in $E_C$ due to the film motion is rather small and is hardly distinguishable in the measurements using static (triangles) and flowing (squares) soap films.

According to Eq. (2.5), the emerging droplet will have a velocity in vertical direction

$$v_y = \frac{M_1}{m+M_1}V_F = \frac{V_F}{1 + \frac{4}{3}\left(\frac{R_0}{\alpha_1^2 h}\right)}, \tag{2.11}$$

where $\alpha_1 = R_1/R_0$. This equation yields the correct asymptotic behavior, $\varepsilon(h)(\equiv v_y/V_F) \to 1$ as $h \to \infty$, as seen in Fig. 13. Using $\alpha_1$ as an adjustable parameter, a fitting procedure gives $\alpha_1 \simeq 4.0 \pm 0.4$, which is delineated by the solid line in Fig. 13.

## 2.4 CONCLUSION

Using well-controlled micron-sized ballistic droplets generated by an inkjet cartridge, we have characterized the energy requirement for tunneling of these droplets through soap films. The energy barrier $E_C(h)$ is found to be linearly proportional to the film thickness $h$ with the result: $E_C = E_{min}(1 + \alpha h/R_0)$. Here the minimal barrier height $E_{min}(\equiv \frac{1}{2}mv_{C0}^2) \simeq 0.01\,\text{erg}$ and the slope $\alpha \simeq 3.9$ are determined. The measured $E_{min}$ corresponds to the creation of an excess surface area of $\sim 14\pi R_0^2$, which turns out to be consistent with the Rayleigh instability condition of pinching off at $\lambda_{max}/2$. The observed $E_{min}$ also implies the existence of a critical Weber number $\text{We}_C(\equiv 2\rho_w R_0 v_{C0}^2/\sigma) \simeq 44$, when the film inertia is unimportant, $h \to 0$.

A self consistent theory is not currently available, and we wish that our observations will provide a useful foundation for such theory. The dynamics is clearly complex in that it involves multiple length and time scales. We have identified two such scales, $R_1$ and $R_2$, that are needed to account for the energy and momentum exchanges between the droplet and the film. A self consistent theory must deal with additional length scales, corresponding to early-time or short-length-scale events, where Re is small, and vorticity production, hence energy dissipation, is prominent. The physics in this regime may explain the intriguing observation that the energy dissipation becomes negligible for some macroscopically thin but microscopically thick films; i.e., the limit $h \to 0$ must correspond to a film that is still thick enough so that it can be stretched to the Rayleigh instability limit. Another issue of interest is the separation dynamics of a tunneling droplet from the rest of the film. This is a singular event that produces discontinuities, such as $v_x \neq v_x'$ at the moment of separation.

This investigation was initially motivated by our desire to print ink patterns in a turbulent flowing soap film and to study how different spatial modes of the pattern are dispersed by turbulent eddies. This would allow passive-scalar turbulence to be studied in a controllable fashion with a defined initial condition. Our measurements presented above give a parameter range for ink droplets to remain on the surface of a moving film, which is a prerequisite for a successful conduct of such measurement. We also found that a ballistic water droplet is an effective wave generator; we had no difficulty of observing the anti-symmetric waves in the film and were able to precisely determine their speeds for different film thicknesses. Curiously, however, the symmetric waves

33

remain elusive. Unlike anti-symmetric waves, the symmetric wave is an important attribute of a soap film and would allow experimenters to obtain useful information about Marangoni elasticity, which is not readily measured in a film. The failure to observe such a wave suggests that the peristaltic oscillations may decay too fast to be seen in our current experimental setting or a different means of perturbation may be needed. We wish to examine this issue more carefully in future experiments.

Aside from its academic interest, the ability of small particles to penetrate a fluid film without damaging it can have important technological applications such as encapsulation of solid particles and transmission of genetic materials through biological cells. The latter is a fascinating application of ballistic transmission in biological systems where gold particles coated with DNA molecules of interest can be be delivered into plant or animal cells [43]. A better understanding of transmission kinematics, such as the one studied here, may shed new light on its working principle and can ultimately improve the quality of this important technology.

# 3.0 STROUHAL-REYNOLDS NUMBER RELATIONS OF VON KÁRMÁN VORTEX STREET

## 3.1 INTRODUCTION

When a uniform stream of fluid encounters an obstacle, a pattern of repeating pairs of vortices is formed. This staggered rows of vortices is observed over a broad range of Re, approximately $50 < \text{Re} < 10^7$. In this range, the flow behind is not steady, causing a periodic vortex shedding from each side of the body. Vortices from each side are rotating in opposite directions, and their interaction produces two rows of counter-rotating vortices.

This so-called von Kármán vortex street has been studied by scientists for many years [79, 58, 7, 63, 92]. Theodore von Kärmän performed the first stability analysis based on a point vortex model [87]. In this model, a complete separation of the irrotational and rotational part of the fluid is assumed, i.e., the vorticity is supposed to occupy infinitesimal amount of area in a 2D inviscid fluid. Subsequent studies include Hooker's correction by including non-zero viscosity [31] to the point vortex model and Saffman's correction by including the finite size of the vortex [74]. However, our fundamental understanding of vortex wake formation, its stability, and evolution still remain largely incomplete and highly phenomenological. At the heart of the problem is why and how vorticity created in the boundary layer of an obstacle and discharged into the bulk of fluid self-organizes into spatiotemporally periodic patterns.

In this work, we wish to address this issue by studying vortex shedding and street formation using rods of different geometric cross-sectional areas in a freely flowing soap film. The use of the film strongly suppresses instabilities and turbulence commonly encountered in three dimensional (3D) fluids, allowing the *laminar vortex streets* to be studied for Reynolds numbers (Re) much higher than achievable in bulk fluids. Here we only present measurements with shapes of aspect

ratios close to unity. Other shapes will be discussed in chapter 4.

We will focus on a Strouhal-Reynolds number relation [58, 93, 28, 54], which connects the dimensionless frequency $\text{St} = fD/U$ to $\text{Re} = DU/\nu$, where $f$ is the vortex shedding frequency, $D$ is a linear dimension of the rod, which will be specified later, $U$ is the mean flow speed, and $\nu$ is the kinematic viscosity. The St-Re relation was proposed by Lord Rayleigh almost a century ago. Based on a hydrodynamic self-similarity hypothesis, he proposed an empirical relation,

$$\text{St} = a\left(1 - \frac{b}{\text{Re}}\right), \tag{3.1}$$

where $a \simeq 0.2$ and $b \simeq 20$ [58] for a circular cylinder [63]. Discrepancies between Eq. (3.1) and measurements exist near the onset of the vortex shedding ($\text{Re} < 100$) and has been recognized by earlier workers. Despite this, Eq. (3.1) has been used for a long time, until Fey *et al.* [28] and Williamson and Brown [93] suggested an alternative equation. Motivated by a boundary layer theory, they individually proposed,

$$\text{St} = a' - \frac{b'}{\text{Re}^{1/2}}, \tag{3.2}$$

where $a'$ and $b'$ are also constants. Even though Eq. (3.2) provides a much better description of data near the onset than Eq. (3.1), the relation has not found a wide use because the two parameters $a'$ and $b'$ are piecewisely determined over different regimes in Re.

Here, our focus will be on a quantitative comparison between measurements and a different St-Re relation:

$$\text{St} = \frac{1}{A + B/\text{Re}}, \tag{3.3}$$

that was recently proposed [67]. This relation can be derived based on general physical considerations with inputs from direct observations of vortex shedding from a *circular* cylinder [67]. The following experimental observations suffice to obtain Eq. (3.3):

1. $f = v_{st}/\lambda$: The spatiotemporal periodicity of the wake implies that the motion of a vortex street behaves as a wave so that the linear dispersion relation $v_{st} = \lambda f$ must hold, where $v_{st}$ is the speed of the vortex street in the lab frame and $\lambda$ is the wavelength, or the longitudinal spacing between two adjacent same-sign vortices [see Fig. 20(a)].

36
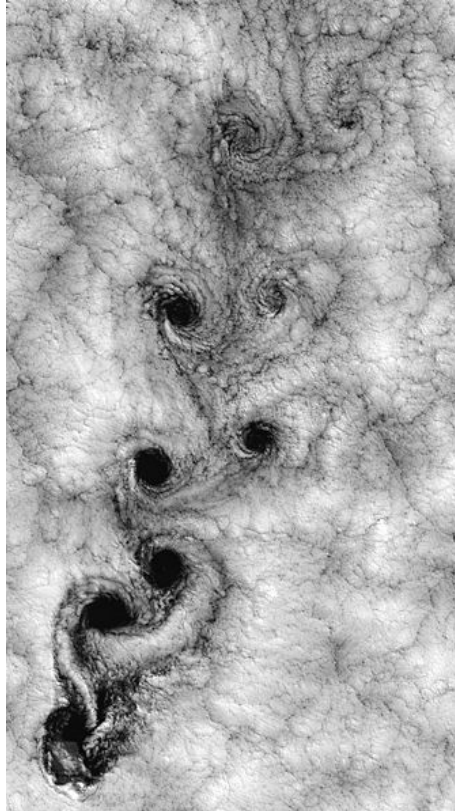
Figure 17: A vortex street produced by Juan Fernández island, Chile.[1]

2. $\lambda/D = \lambda_0/D + \alpha$: Over a broad range of $D$, $\lambda$ is a linear function of $D$, $\lambda = \lambda_0 + \alpha D$, with $\lambda_0$ and $\alpha$ being constant. This is an observational result [67].

3. $v_{st}/U \sim$ const: $v_{st}$ is a fixed fraction of $U$ and depends on $D$ only weakly, e.g. $c(\equiv v_{st}/U) \simeq 0.8$ for the circular cylinder. This is again an observational result [67].

Using the above three ingredients, one can construct $\mathrm{St} = fD/U = \frac{v_{st}/U}{\lambda/D}$, and it follows that $A$ and $B$ in Eq. (3.3) are given by $A = \alpha/c$ and $B = \lambda_0 U/(c\nu)$. Thus, the coefficients $A$ and $B$ are closely related to the physical processes of boundary layer instability, which gives rise to the wavy behavior characterized by the parameters $\alpha$ and $\lambda_0$, and to properties of vortices, whose strength determines $c$ [7]. Roushan and Wu [67] showed Eq. (3.3) is better than either Eq. (3.1) or (3.2) for describing vortex shedding for rods of circular shape. The current work is motivated by the expectation that Eq. (3.3) may be also applicable to slender bodies of non-circular shapes because Eq. (3.3) is derived using a rather general physical argument.

In this work, we generated vortex streets using rods of both circular and non-circular cross-sectional shapes. We present the first experimental evidence that Eq. (3.3) is adequate for describing vortex shedding for rods other than the circular shape. This finding implies that the underlying physics for different shapes perhaps is simple and can be explained by the same mechanisms discussed above. Another simplifying feature found in our measurement is that $A \simeq 4.7$ turns out to be nearly identical for all rods, indicating that the asymptotic Strouhal number $\mathrm{St}_\infty(\equiv 1/A) \simeq 0.21$ may be universal for $\mathrm{Re} \to \infty$. Thus, most of the shape-dependence is in $B$, which is related to $\lambda_0$ and $c$.

## 3.2  EXPERIMENTS

### 3.2.1  Inclined soap film

Our measurements were carried out in an inclined soap-film channel (see Fig. 18) previously described in Refs. [70, 69] and in the previous chapter. An inclined soap film was developed by Mr. Roushan to reduce the effect of the gravity on the vertical soap film channel [68]. As a result, the flowing speed $V_F$ is greatly reduced in the inclined soap film than in the vertical soap film. The

construction of the inclined soap film is very similar to the construction of a vertical soap film. For the inclined channel to work properly, it requires that all components of the channel should be able to rotate together about a pivoting axis. Specifically, the film used was inclined by 78°, and the gravity was reduced by a factor of $\cos 78° = 0.21$. The $200 \times 5 \, \text{cm}^2$ soap film flows continuously with a speed $U$, which can be varied from 50 to 130 cm/s by changing the injection flux of the soap solution. In most runs, the flowing speed was fixed as $U \sim 60 \, \text{cm/s}$. At such settings, the film is weakly compressible with a Mach number $M = U/v_w \sim 0.1$, where $v_w$ is the propagating speed of an antisymmetric wave on the film. Sagged by the gravity, the film is thicker in the middle than near the wires. However the width of the channel is much larger than the width of the vortex streets, therefore the thickness variation is negligible and the film thickness $h \sim 3 \, \mu\text{m}$ can be considered uniform. The rms fluctuations of $U$ was a few percent and was the main source of uncertainties in the measurement.

The soap solution consisted of a mixture of 2% Dawn liquid detergent, 5% glycerol, and water. The viscosity of the soap solution, determined by a Cannon viscometer, was $v \simeq 0.013 \pm 0.001 \, \text{cm}^2/\text{s}$.

### 3.2.2 Tapered rods and definition of the linear dimension $D$

To create vortex streets, we used tapered rods of different geometrical cross sections, such as circles, squares, diamonds, and equilateral triangles as delineated in Fig. 19. These tapered rods were carefully made of titanium or glass, depending on their sizes. Titanium rods were machined to have tips of size $\lesssim 10 \, \mu\text{m}$ and glass rods were thermally tapered to have tips of size $\sim 1 \, \mu\text{m}$.

By using a motorized translation stage, which is mounted perpendicular to the soap film channel, a rod can be moved perpendicular to the film plane. By adjusting the depth of insertion of the rod into the film, its width $W$ facing the flow (see Fig. 19) was varied. Here, $W$ was precisely measured by a CMOS camera (DCM130, OPLENIC) mounted on a long-working-distance microscope. For each shape, we defined an outer length $D$, which is the diameter of the smallest circle enclosing the particular shape. For example, for a circle, $D = W$, however for a square, $D = \sqrt{2}W$, and for for a triangle, $D = \frac{2}{\sqrt{3}}W$. In this experiment, $\text{Re} = UD/v$ was solely determined by $D$, as $U$ and $v$ were fixed. It will be shown that our way of defining $D$ will lead to the observation of a

39
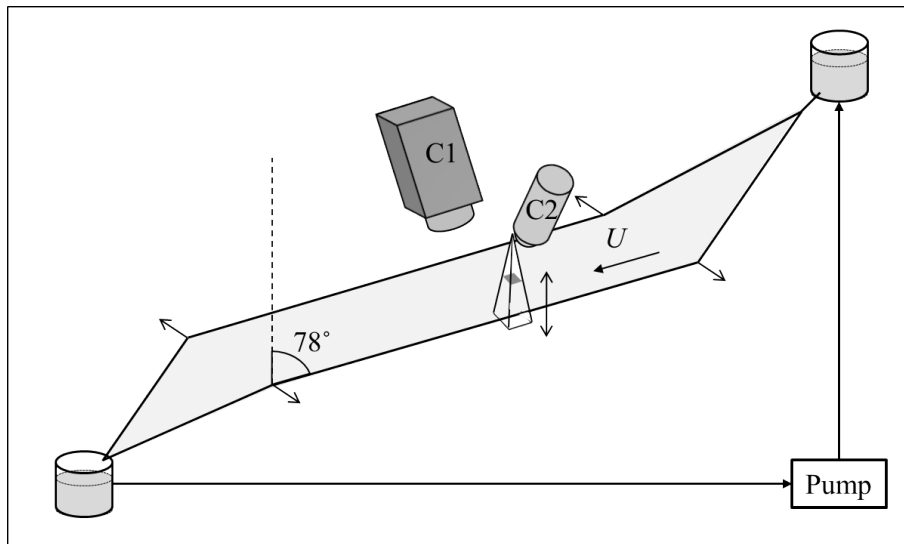
Figure 18: Experimental setup. The soap film channel is inclined at $78°$ from vertical. Soap solution is injected from the top reservoir and collected at the bottom reservoir. The flow speed $U$ is varied by controlling the injection flux. In the experiment, $U$ is fixed at $\sim 60$ cm/s. A fast video camera (C1) and a microscope (C2) are mounted directly above the film.
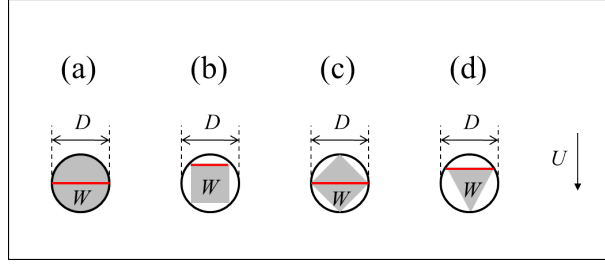
Figure 19: Cross sections of tapered rods. (a) A circular, (b) a square, (c) a diamond and (d) a triangular rod are delineated. When the flow is from the top to the bottom of the page, $W$ denotes the width of rods facing the flow. The linear dimension of the rod $D$ is defined as a diameter of the smallest circle enclosing a particular shape.

constant St at large Re.

When a rod is inserted into the film, depending on Re, a vortex street is formed behind the rod. The wake structure was captured [see Figs. 20(a) and (b)] by a high-speed CCD camera (Phantom V, Vision Research), while the film was illuminated by a sodium lamp (wavelength 590 nm). By performing image analyses, $U$, $\lambda$, $f$, and $v_{st}$ were precisely measured.

## 3.3   RESULTS AND DISCUSSIONS

In Figs. 20(a) and (b), we present snapshots of typical vortex streets generated using a circular and a square rods, respectively. Two vortex streets were generated at the same Re, or the same $D$. These two vortex streets are very similar in appearance. However, even though they are produced using rods of the same $D$, the wavelength $\lambda$ of the respective vortex streets are different. Inspired by these observations, we postulate:

1. The underlying physical mechanism for generating vortex streets may not be changed regardless the shape used.

2. Different shaped rods may contribute to different boundary layer structures and hence different wavelengths.

41

3. The amount of vorticity injected into fluid may be altered by changing the rod shape.

In the following sections, we will first focus on the structure of the vortex street. We characterize the wavelength $\lambda$ and $v_{st}$ using four structure parameters $\lambda_0$, $\alpha$, $c$, and the size of the rod $D$. Then we will turn our attention to the measurement of vortex shedding frequency $f$, or the St-Re relation.

### 3.3.1 The wavelength

As mentioned in the introduction, the wavelength of the vortex street is defined as the distance between two adjacent vortices of the same handedness, as delineated in Fig. 20(a). Qualitatively, the distance between two neighboring vortices increases as the pair moves downstream, and eventually reaches an asymptotic value. For simplicity of discussion, we define $\lambda'(y)$ as the longitudinal spacing between vortices in a row, which is a function of both $D$ and $y$, the downstream distance. At $y \to \infty$, $\lambda'$ approaches a certain value $\lambda(D)$.

Figures 21(a)-(d) show the asymptotic wavelength $\lambda$ as a function of $D$ for circular, square, diamond, and triangular rods, respectively. A common feature of these measurements is that $\lambda$ is linear in $D$,

$$\lambda = \lambda_0 + \alpha D, \tag{3.4}$$

where the intercept $\lambda_0$ and the slope $\alpha$ varies depending on rod shapes. Values of $\lambda_0$ and $\alpha$ for different shaped rods are given in Table 1.

In an effort to understand the physical origin of $\alpha$, we made a quantitative investigation of the evolution of vortex streets as a function of $y$. Using circular rods, the transient wavelengths $\lambda'(y)$ were measured for different $D$, and the result is displayed in Fig. 22(a). We found that all the measurements obey the simple mathematical form,

$$\lambda'(y) = \lambda(1 - e^{-y/y_0}), \tag{3.5}$$

with $y_0$ being a characteristic decay length and $\lambda$ the wavelength at a large distance. By using Eq. (3.5), $y_0$ and $\lambda$ are determined for each $D$. In Fig. 22(b), $\ln(1 - \lambda'/\lambda) \equiv \ln(1 - \Lambda)$ is plotted against $y/y_0 \equiv Y$. The linearity with zero intercept and the slope -1 observed in (b) provides a
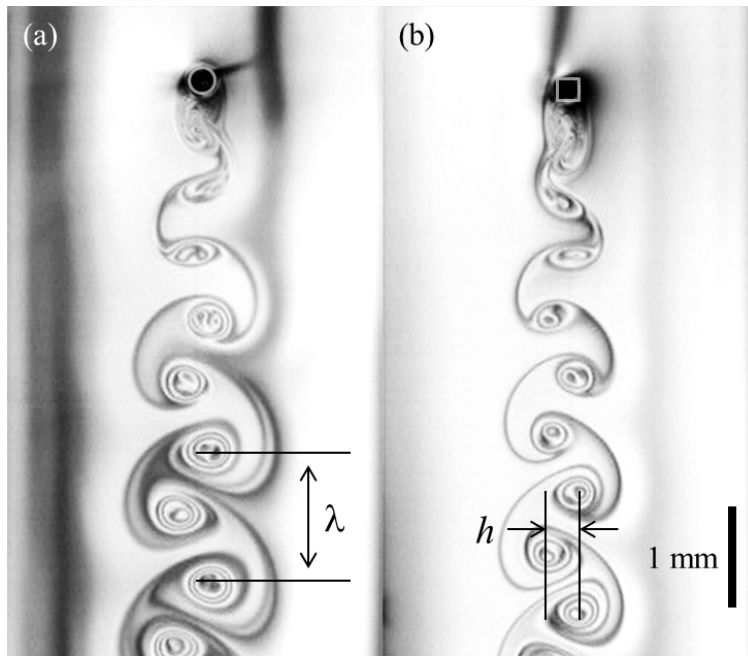
Figure 20: Vortex streets created by (a) a circular and (b) a square rod of the same $D = 0.035\,\text{cm}$ (Re $= 170$). The structures of the vortex streets appear similar, suggesting their underlying generating mechanism might be also the same.
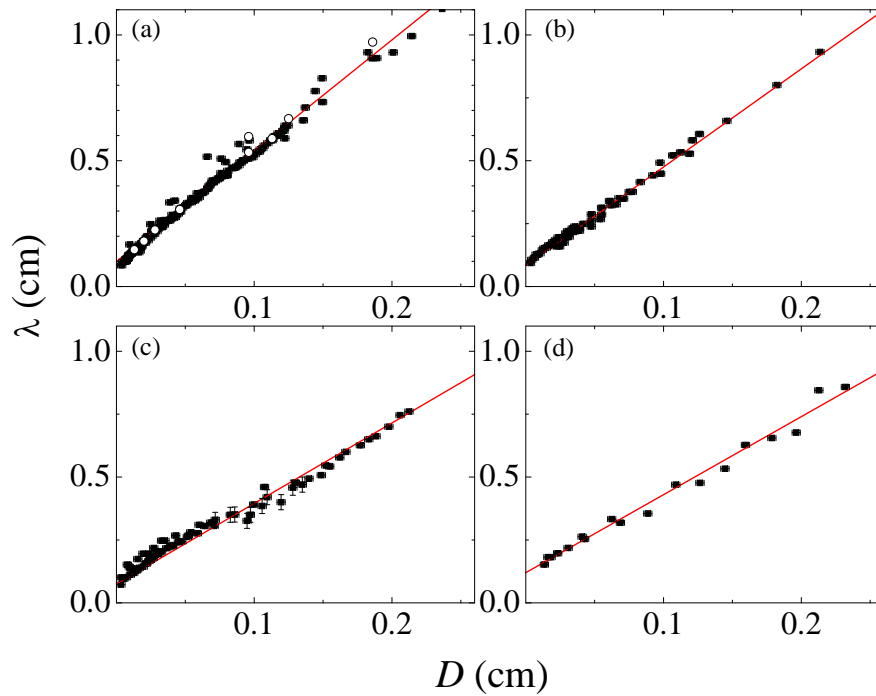
Figure 21: Wavelength $\lambda$ vs. $D$ for (a) circular, (b) square, (c) diamond, and (d) triangular rods. Here, $\lambda$ is defined far from the rods, $\lambda \equiv \lambda'(y \to \infty)$. In all cases, $\lambda$ is linear in $D$ with a non-zero positive intercept. Both the slope ($\equiv \alpha$) and the intercept ($\equiv \lambda_0$) varies with shapes.

|       | C | S | D | T |
|-------|---|---|---|---|
| $A$ | $4.8 \pm 0.1$ | $4.4 \pm 0.1$ | $5.0 \pm 0.1$ | $4.6 \pm 0.2$ |
| $B$ | $648 \pm 46$ | $505 \pm 45$ | $410 \pm 24$ | $533 \pm 41$ |
| $c$ | 0.8 | 0.86 | 0.63 | 0.7 |
| $\alpha$ | $4.5 \pm 0.1$ | $3.9 \pm 0.2$ | $3.2 \pm 0.2$ | $3.1 \pm 0.4$ |
| $\lambda_0$ (mm) | $1.00 \pm 0.05$ | $0.85 \pm 0.05$ | $0.75 \pm 0.20$ | $1.2 \pm 0.2$ |
| $A = \alpha/c$ | $5.6 \pm 0.1$ | $4.5 \pm 0.2$ | $5.1 \pm 0.2$ | $4.4 \pm 0.6$ |
| $B = \lambda_0 U/c\nu$ | $577 \pm 29$ | $456 \pm 27$ | $549 \pm 147$ | $791 \pm 132$ |

Table 1: *A* and *B* from direct measurements [see the insets of Figs. 25(a)-(d)] and from calculations (bottom two rows). These are supposed to be identical, however there exist discrepancies, mainly due to setting *c* constant. Using the standard regression analysis method, the limits of significance (at 95% confidence level) were determined, and the true value of *A* for a circular rod may exist between 4.7 and 4.9 at 95% chance [17, 41].

strong verification of Eq. (3.5). As shown by the open circles in Fig. 21(a), $\lambda$ acquired here is entirely consistent with the previous measurements

We also found that $y_0$ is proportional to $\lambda$, and intriguingly the proportionality constant is very close to $1/\alpha = 0.22$ as depicted in Fig. 22(c). Equation (3.5) suggests that $\lambda'$ associated with the fundamental shedding frequency $f$ is continuously stretched by the flow and can be reasonably described by,

$$\lambda'(y) = \lambda \left( 1 - e^{-y/\alpha^{-1}\lambda} \right). \tag{3.6}$$

Using Eq. (3.4), Eq. (3.6) can be written as

$$\lambda'(y) = \alpha \left( D + \frac{\lambda_0}{\alpha} \right) \left[ 1 - e^{-\left( D + \frac{\lambda_0}{\alpha} \right)^{-1} y} \right]. \tag{3.7}$$

In this expression, one can observe that a new length scale $\frac{\lambda_0}{\alpha}$ emerges, and such a length scale is stretched by a factor $\alpha$ to give rise the wavelength $\lambda_0$ that we observe. Note, typically $\lambda_0/\alpha \sim$

$200\,\mu$m, and when $D = 200\,\mu$m, the boundary layer thickness $\delta_b = 5\sqrt{\nu D/U} \sim 100\,\mu$m. Therefore, $\lambda_0/\alpha$ represents a characteristic length that separates two regimes where $\delta_b \ll D$ and where $\delta_b \gg D$.

In an effort to understand physical meaning of $\alpha$, we seek to explain our observation using the simple picture of stretching of a passive scalar by potential flow near a circular cylinder. Without a rigorous mathematical description for near-wake dynamics, this is the best we could do, and we believe that the calculation should be reasonably accurate very close to the onset of the vortex shedding [35].

Specifically we would like to know how a small fluid element of size $l_0$ near the rod would be stretched downstream due to the velocity gradient induced by the potential flow. In the laminar flow regime[1], the potential flow in a polar coordinate system (See Fig. 23) is given by

$$\phi(\vec{r}) = U\left(r + \frac{D^2}{4r}\right)\sin\theta. \tag{3.8}$$

This velocity potential satisfies the boundary conditions:

1. at $r \to \infty$, $v_x = \partial_x\phi = 0$ and $v_y = \partial_y\phi = U$,

2. at $r = D/2$, $v_r = \partial_r\phi = 0$ (slip boundary condition).

The rate of stretching in the radial direction is

$$\partial_r v_r(\equiv \frac{\partial^2\phi}{\partial r^2}) = \frac{U\sin\theta}{2D}\cdot\left(\frac{D}{r}\right)^3. \tag{3.9}$$

At the stagnation point downstream, $r = D/2$ and $\theta = \pi/2$, the stretching rate is maximum with $\partial_r v_r = 4U/D$. The small fluid element will be stretched when $\partial_r v_r \neq 0$. The stretching rate decays as $y^{-3}$ in the laminar flow regime. However vortex shedding may alter this $y$ dependence. According to our observation it is appropriate to assume that the stretching rate decays as $\sim \exp\left(-\frac{y}{D}\right)$. Using this simple ansatz, the small fluid element of size $l_0$ at $y = 0$ will be stretched downstream to the size of $l$ according to

$$\begin{aligned} dl &= l_0\,(\partial_r v_r)\,|_{\theta=\pi/2}dt \\ &\simeq 4l_0\exp\left(-\frac{y}{D}\right)d\left(\frac{y}{D}\right), \end{aligned} \tag{3.10}$$

---

[1]When Re is slightly above the onset, the vorticity near the rod will be discharged into the flow and will be stretched by neighboring potential flow.
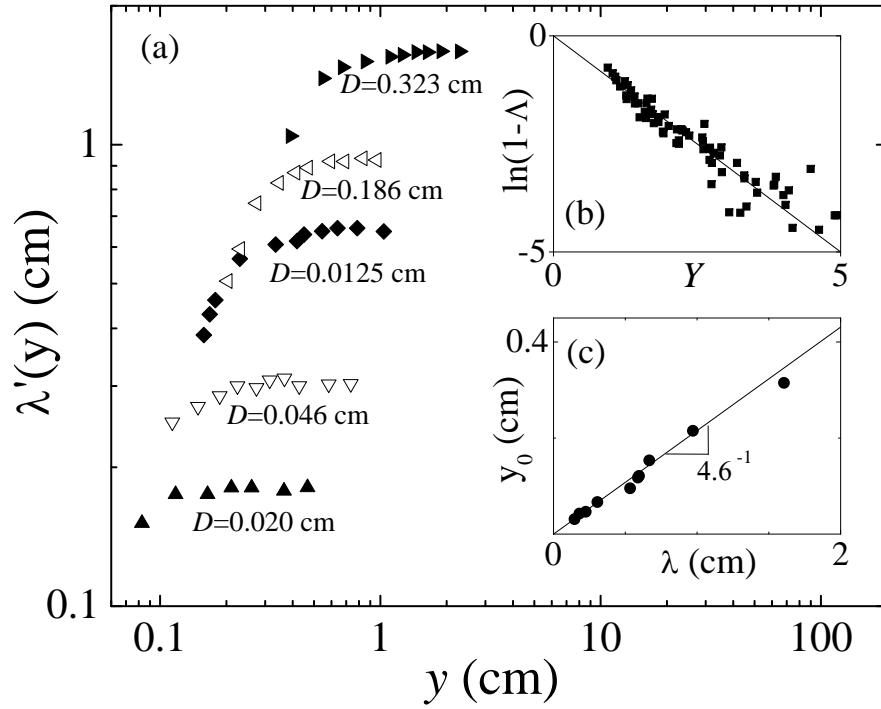
Figure 22: The wavelength $\lambda'$ vs. $y$. In (a), it is depicted that for each $D$, $\lambda'$ initially increases with $y$, but it reaches an asymptotic value $\lambda$, implying $\lambda' = \lambda(1 - e^{-y/y_0})$, where $\lambda$ and $y_0$ are parameters depends on $D$. In (b), $\ln(1 - \Lambda)$, where $\Lambda \equiv \lambda'/\lambda$, is plotted against $Y \equiv y/y_0$. The observed linearity verifies Eq. (3.5). In (c), $y_0$ is proportional to $\lambda$ with the proportionality constant close to $\alpha^{-1} = 0.22$ for the circular rods.
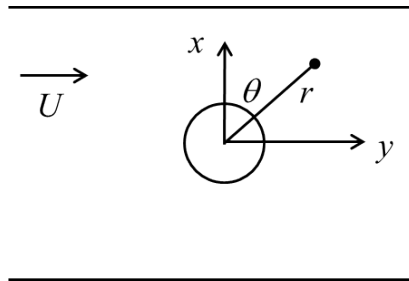


Figure 23: A polar coordinate system in the uniform fluid flow.

where $dy = U\,dt$ and is used. Upon integration, we have

$$l(y) = l_\infty - 4l_0 \exp\left(-\frac{y}{D}\right), \tag{3.11}$$

where $l_\infty$ is the fully stretched length. We determine $l_0$ self consistently with $l(0) \equiv l_0 = l_\infty - 4l_0$. This yields $l_\infty = 5l_0$, implying that the small fluid element near the rod is eventually amplified by 5 times. This amplification factor is consistent to $\alpha$ in Eq. (3.7),

$$\alpha = l_\infty/l_0 = 5. \tag{3.12}$$

Replacing $l$ by $\lambda'$ and $l_\infty$ by $\lambda$ leads to

$$\lambda'(y) = \lambda \left[1 - \frac{4}{5} \exp\left(-\frac{y}{D}\right)\right]. \tag{3.13}$$

Both Eqs. (3.12) and (3.13) are qualitatively consistent with our observations, if one assumes that vorticity behaves like a passive scalar.

### 3.3.2   The vortex street velocity

In Figs. 24(a)-(d), we plotted $c \equiv v_{st}/U$ vs. Re for different rods. Like $\lambda'$, $v_{st}/U$ is also a function of the downstream distance and approaches an asymptotic value at $y \to \infty$. As can be seen, $c$ is not a monotonic function of $D$ in general. It is found that $c$ initially decreases with Re (starting from $\sim 0.9$), reaches a minimum value $c_{min}$ at a certain Re, and $c$ may increase again for even larger Re. In particular, for circular and square rods, $c$ reaches $c_{min} \simeq 0.8$ near Re $\sim 400$ and increase when Re $> 1000$. For diamond and triangular rods, $c$ reaches $c_{min} \simeq 0.7$ and no further increase in $c$ was observed for the given range of Re. Physically, $c$ is a measure of vortex strength $\kappa$ (or the circulation); the more powerful the vortices are the smaller the value of $c$. Using a point-vortex model, von Kármán showed that a vortex street travels against a *static* background fluid with a velocity [7]:

$$v'_{st} = \frac{\kappa}{2\lambda} \tanh\left(\frac{h\pi}{\lambda}\right), \tag{3.14}$$

where $h$ is transverse spacing between the vortices, and $v_{st} = U - v'_{st}$ is the velocity of the vortex street in the laboratory frame. It is clear that for diamond and triangular rods, the trailing edge reduces the base suction pressure, resulting in a wider wake and a somewhat larger Kármán ratio
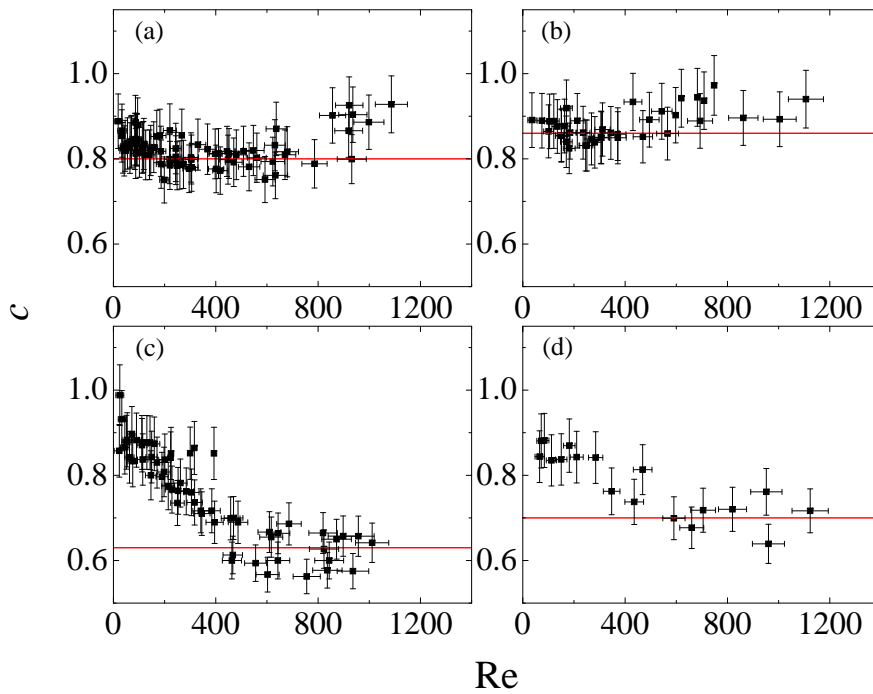
Figure 24: $c$ vs. Re for (a) circular, (b) square, (c) diamond, and (d) triangular rods. The horizontal lines denote $c_{min}$. When Re is small, $c$ decreases as Re increases. For circular and square rods, $c$ appears to increase again after reaching $c_{min}$ as Re increases.

$h/\lambda$. The trailing edge also physically separates two sides of the boundary layers, preventing annihilation of vorticity of opposite handiness. These two effects conspire to give diamond and triangular rods a lower $c_{min}$ than that of circular and square rods. It is noteworthy that if we used the Kármán's stability condition $\tanh(\frac{h\pi}{\lambda}) = 1/\sqrt{2}$ and assume that vorticity created in the boundary layer are 100% encapsulated into the eyes[2] of vortices, $\kappa \simeq \lambda U$ [80], it follows $c \equiv (1 - v'_{st}/U) = 1 - \frac{1}{2\sqrt{2}}$ or 0.65. This result is remarkably close to our measured $c_{min}$ for diamonds and triangles, suggesting that these geometries permit the maximum preservation of vorticity. On the other hand, when Re is not so large or when circular and square rods are used, a noticeable amount of vorticity must have been annihilated before a stable vortex street is formed.

### 3.3.3 St-Re relation

We next turn our attention to the experimental determination of the St-Re relation. Here, the shedding frequency $f$ was measured by directly counting the number of vortices peeling off from a rod in a given time interval. We verified that this counting method is identical to the power-spectrum measurement downstream using a laser Doppler velocimeter (LDV), showing that vortex streets are laminar and $f$ represents the global mode of oscillations [56]. Also, in all measurements, $f$ was equal to $v_{st}/\lambda$ within the limit of experimental uncertainties, providing a solid support for the validity of the linear dispersion relation.

Figures 25(a)-(d) display runs with circular, square, diamond, and triangular rods, respectively. We noted that for all geometries, the *laminar* vortex shedding persists over a broad range of Re up to Re $\sim 1200$. This is about an order of magnitude (or 6 times) greater than in similar measurements carried out in 3D [91, 48, 98]. All the data exhibit a similar trend, i.e., St increases rapidly with Re near an onset Re$_C$, and it levels off for large Re. Because of uncertainties in the measurement, we were unable to determine how Re$_C$ varies with the rod geometry. However, all of our data are consistent with the onsets occurring within $10 < \text{Re}_C < 30$, which are lower than Re$_C \sim 47$ typically reported for circular rods in 3D [56, 92, 48]. We found that all of our measurements can be adequately described by Eq. (3.3), which are displayed by solid lines in Figs. 25(a)-(d). The quality of the fits using Eq. (3.3) can be compared to that using Eq. (3.1) [dotted lines in Figs.

---

[2]The eye of a vortex is a circular swirl that is observable in Fig. 20.

25(a)-(d)] and are quantified by the $\chi^2$ values tabulated in Table 2. The appropriateness of the equation can also be demonstrated by the linear behavior of $St^{-1}$ vs. $Re^{-1}$ plots presented in the insets.

The *A* and *B* coefficients determined by fitting the data of Fig. 25 are in reasonable agreement with those calculated from wake structure measurements ($\alpha/c$ and $\lambda_0 U/cv$), indicating consistency between different types of measurements (see Table 1). Given that the linear dispersion relation was confirmed experimentally, the discrepancies, sometimes as large as $\sim 30\%$ between the measured and the calculated *B*, are mainly due to the approximation of setting $c_{min}$ to a constant.

A conspicuous feature of the measured St-Re relationships depicted in Figs. 25(a)-(d) is that as $Re \to \infty$, St appears to approach a universal asymptotic value $St_\infty$, regardless of the shape. We would like to point out that while $\alpha$ and $c$ (as well as $\lambda_0$) are shape dependent, the ratio $\alpha/c$ is only weakly so, indicating that there is a correlation between $\alpha$ and $c$. It is found that $St_\infty \simeq 0.21$ and its variation due to the rod shape is less than 5%. This constant value is obtained only when we used *D* instead of *W* to characterize vortex shedding. If *W* were used, the asymptotic $St_\infty$ differs significantly from rod to rod. This indicates that *D* is more relevant than *W* in the interpretation of physical process of vortex shedding when $Re \to \infty$. This asymptotic behavior may be understood as the instability being associated with the irrotational part of the fluid flow, which becomes more prominent as Re increases. We posit that for large Re, the shedding frequency *f* only depends on the largest dimension of the disturbance, whose relevance to *D* may be explained by multipolar expansions of the potential flow. At high Re, as the flow is only slightly compressible (Mach number $M \sim 0.1$) and most vorticity is concentrated inside the vortex eye [68, 8, 2], a flow can be considered approximately potential in most region of the fluid (see Appendix C.1). Then the far field of the potential flow for different shapes can be represented as a linear superposition of singularities of different orders via a multipole expansion.

For a circular cylinder, the potential function is described by

$$\phi_{circle} = U \left( r + \frac{D^2}{4r} \right) \cos \theta. \tag{3.15}$$

Without losing generality, we can set $U = 1$ and $D = 1$ for simplicity

$$\phi_{circle} = r \cos \theta + 0.25 \frac{\cos \theta}{r}. \tag{3.16}$$

51
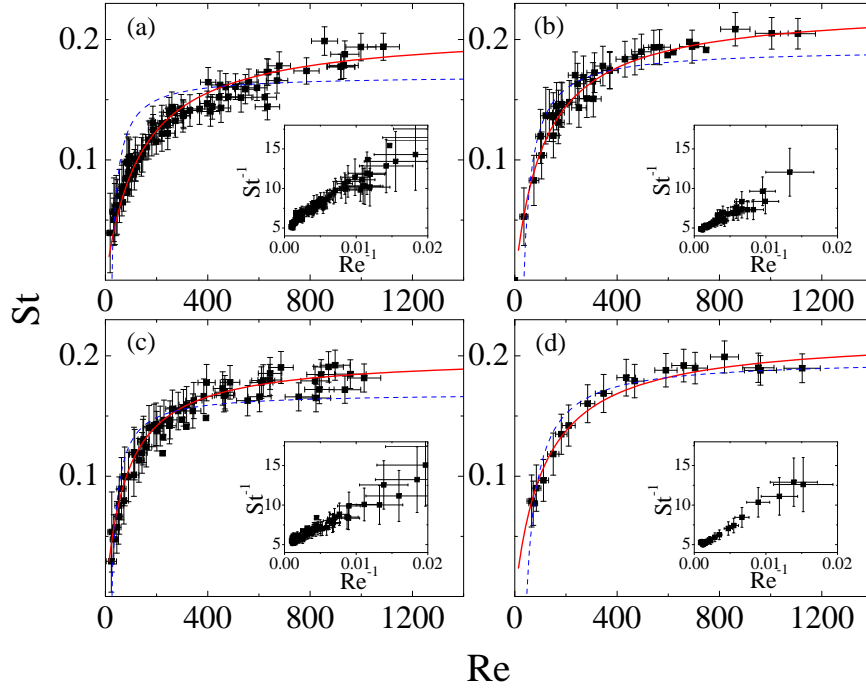
Figure 25: St vs. Re for (a) circular, (b) square, (c) diamond, and (d) triangular rods. Solid and dotted lines in (a)-(d) are theoretical predictions according to Eq. (3.3) and Rayleigh's relation Eq. (3.1), respectively. The insets are $St^{-1}$ vs. $Re^{-1}$ plots.

| $\chi^2$ ($\times 10^{-4}$) | Circle | Square | Diamond | Triangle |
|---|---|---|---|---|
| Eq. (3.3) | 0.7 | 0.3 | 0.7 | 0.4 |
| Eq. (3.1) | 5.0 | 1.1 | 3.1 | 1.2 |

Table 2: Unnormalized $\chi^2$-square values from fits to two different equations. Equation (3.3) yields much lower $\chi^2$-square values than Eq. (3.1) for all shapes. This means that Eq. (3.3) describes data better than Eq. (3.1).

Here the first term represents the mean flow, and the second term represents the dipolar field which is required to match the boundary condition at the surface of the circular rod. For a square rod, Eq. (3.15) must be modified to match with the boundary condition for the square. This modification can be made numerically[3],

$$\phi_{squre} = \phi_{circle} + 0.052 \times \frac{\cos 3\theta}{r^3} - 0.023 \times \frac{\cos 5\theta}{r^5} + \cdots . \tag{3.17}$$

Similar calculation can be done for a diamond rod with the result,

$$\phi_{diamond} = \phi_{circle} - 0.0019 \times \frac{\cos 3\theta}{r^3} + 5.5 \times 10^{-4} \times \frac{\cos 5\theta}{r^5} + \cdots . \tag{3.18}$$

As can be seen, in addition to the dipolar term, Eqs. (3.17) and (3.18) contain additional multipolar terms, each of which is associated with a corresponding mode of oscillation. However the strength of higher order poles are much weaker than that of the dipole, and the potential flow past a non-circular rod is essentially dominated by the dipolar field with $D$ the same as its equivalent. It remains an intriguing possibility that the observed oscillation may be due to the instability of this dipolar field. The universal shedding frequency is thus related to the angular mode of the dipolar expansion which yield a constant frequency $f \propto \frac{U}{D}$ when Re $\to \infty$.

While our parametrization scheme makes $A$ independent of geometry, $B$, which determines the crossover from low to high Re regimes, remains strongly dependent on the rod shape. It is found that rods with sharp corners (square, diamond, and triangular rods) reaches $St_\infty$ faster than the circular rods. Since when Re $= B/A$, St $= \frac{1}{2}St_\infty$, the value $B/A$ is a measure of how rapidly St approaches to $St_\infty$. The square, diamond, and triangular rods yield, respectively, 1.18, 1.65, 1.17 times greater $B/A$ value compared to the circular rod. Using $A = \alpha/c$ and $B = \lambda_0 U/cv$, it is easy to see that

$$St = \frac{1}{(A + B/\text{Re})} = \frac{1}{A} \cdot \frac{D}{\left( D + \frac{\lambda_0}{\alpha} \right)}. \tag{3.19}$$

A simple physical picture that emerges from this study is that the two parameters $A$ and $B$ are essentially determined by two relevant scales in the problem, $D$ and $\lambda_0/\alpha$. When Re is large, the oscillation is governed by the outer scale of the problem $D$, and the approximation $\lambda \sim \alpha D$ is reasonable or equivalently $D \gg \lambda_0/\alpha$. For small and intermediate Re $\lesssim B/A = \frac{(\lambda_0/\alpha)U}{v}$, on the

---

[3]Details of the calculation can be found in the Appendix C.

other hand, the influence of the boundary layer thickness, whose significance is characterized by the scale $\lambda_0/\alpha$, scales with $\sqrt{D}$ and is not negligible compared to $D$. Our measurements show that all the shape-dependence is buried in $B$ and is related to the inner scale $\lambda_0$.

## 3.4  CONCLUSION

In summary, we demonstrated that the new St-Re relation, Eq. (3.3), is applicable to vortex shedding behind non-circular rods. It is shown that the $A$ and $B$ coefficients in the equation are determined respectively by two characteristic length scales $D$ and $\lambda_0$ in the flow. In the high Re regime, the potential flow dominates and the oscillation frequency appears to be uniquely determined by the largest length scale $D$ in the problem. On the other hand, in the low and intermediate Re regimes, where fluid viscosity cannot be neglected, $\lambda_0$ also contributes to the oscillation, and it is shape dependent. The work reported herein demonstrates that in a soap film, mixing between the rotation part and the potential part of fluid flows is weak, giving rise to important features of fluid dynamics. These include:

1. The vorticity created in the boundary layer is efficiently encapsulated into the eyes of vortices, particularly for diamond and triangular rods that contains a sharp trailing edge.
2. The laminar wake persists over a broad range in Re, which results from an absence of vortex stretching in a 2D fluid.
3. Asymptotically, the oscillation is determined by a single scale $D$.

This last property is remarkable considering that in 3D fluids, the potential part of fluid flow is rapidly spoiled by small-scale velocity fluctuations as Re increases, which lead to chaotic or turbulent behaviors. In our case, however, since small-scale velocity fluctuations (or strong vorticity) are well isolated in small regimes, potential flow becomes more prominent as Re increases. The separation of potential and viscous regions is a hallmark of 2D fluid flow and can be readily seen in a 2D soap film. This important property may be exploited further to address fundamental issues in fluid dynamics.

## 4.0  ONSET OF TYPE 2 VORTEX STREETS

### 4.1  INTRODUCTION

Von Kármán vortex streets discussed in the previous chapter are robust over a broad range of Reynolds number ($30 < \text{Re} < 10^7$) and stable over a long distance. Using a point vortex model, Theodore von Kármán performed a stability analysis and suggested two conditions for such a vortex street to be stable [87]:

1. Two rows of vortices must be out of phase with respect to each other; namely, a vortex must be located at the same distance from two neighboring vortices of the opposite handedness.

2. The so-called Kármán ratio $K_r$, the transverse distance $h$ between two staggered rows to the wavelength $\lambda$ (see Fig. 20 for definitions), must be 0.28.

Experiments, including those reported in the previous chapter, show that the first condition is satisfied most of times. However, the second condition is often violated. Measurements by Rosenhead and Schwabe showed $K_r \simeq 0.3$ [62] whereas Fage and Johansen found $K_r = 0.25$, 0.38 and 0.52 [26]. Our own data in chapter 3 also indicate that $K_r$ is between 0.3 and 0.5 (see Fig. 27), which are larger than the proposed value 0.28. However, to our knowledge $K_r$ significantly greater than 0.28, say by a factor of two, or significantly less than 0.28 is rarely observed.

In this chapter, we will discuss the existence of a quasi-steady-state vortex street in which the second stability condition is significantly violated. We shall call these vortex streets "type II" as opposed to the normal "type I" streets, which are presented in chapter 3. One such type II vortex streets is shown in Fig. 26. This vortex street differs from the type I in the following ways:

1. The Kármán ratio $K_r$ is much greater than those of type I (see Fig. 27).
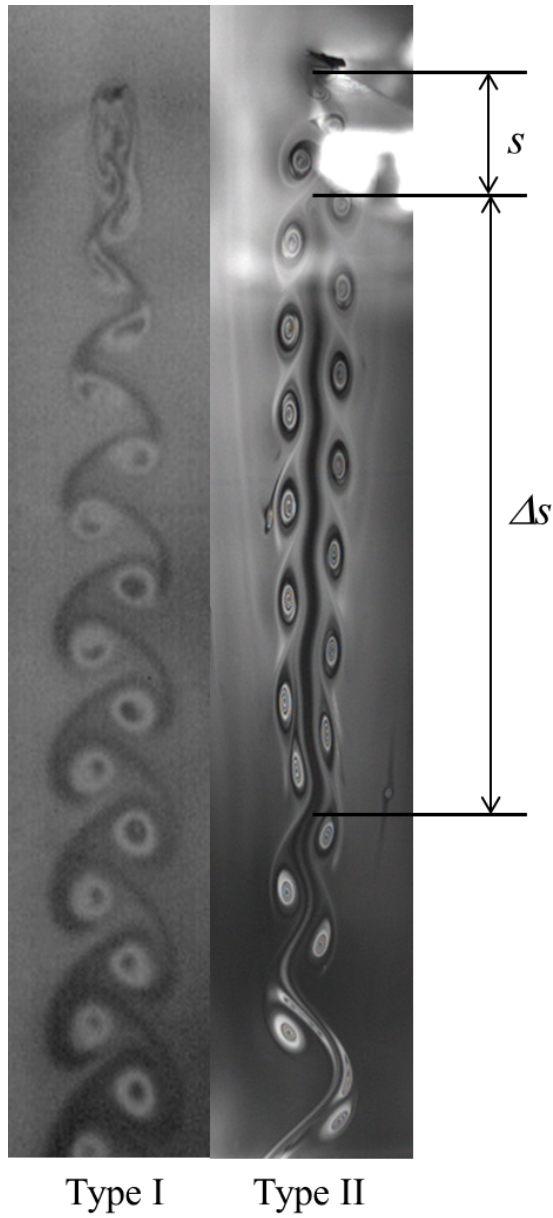
Figure 26: A snapshot of a typical type I and II vortex street. The type II vortex street is created by a triangular rod with $W = 0.13\,\text{cm}$, corresponding to $\text{Re} = 660$. It is evident that the type II differs from type I in that there exists an irrotational flow region that separates the two staggered rows of vortices. This zigzag region resembles a snake swimming up stream in our video clips and hence earns the name "snake region" used in the main text. The type II street is metastable, and it disintegrates down street and ultimately form the type I street.

2. There exists a potential flow region between the two rows of the vortices, providing a barrier between the two signed vortices.

3. They are metastable. After persisting for a certain distance downstream, which depends on Re, two neighboring vortices of the same handiness merge, forming a bigger vortex.

In our work, we found that type II vortex streets can be readily and reliably created using an equilateral triangular rod with one of its sharp corners facing the upstream flow. Motivated by this observation, we manufactured triangular rods with different aspect ratios or acuteness $r_a = H/W$, where $H$ is the height and $W$ is the base of the triangle. Measurements showed that type II vortex streets originates from type I street because the wake structure immediately adjacent to the rod is always the first type. For the type II vortex street to emerge, the Reynolds number Re must exceed some critical value $\text{Re}_{C2}$, which depends on $r_a$. When $\text{Re}_C < \text{Re} < \text{Re}_{C2}$, only the normal type I vortex streets are observed, and when $\text{Re} > \text{Re}_{C2}$, both type I and II are observed.

## 4.2  EXPERIMENTS

Aside from the different shaped rods used, the experimental methods are identical to those discussed in the previous chapter. Specifically, we used five tapered triangular rods with different aspect ratios $r_a =$0.3, 0.5, 0.87 (equilateral), 1.5, and 2.5 as depicted in Fig. 28. Similar to the previous chapter, these rods were made of titanium and precisely machined to a tip size $\sim 50\,\mu$m. Using a translational stage, a rod was mounted and moved through the inclined soap film while its insertion depth was monitored by the CMOS camera mounted on the long-range microscope. The downstream wake structures were monitored by the fast video camera.

In this study, the linear dimensions relevant to the flow structures are $W$ and $H$, and we will use dimensionless number $\text{Re} \equiv WU/\nu$ and $r_a$ to characterize the flow. By this definition, triangles with the same base $W$ but with different heights $H$, will have the same Reynolds number Re but different $r_a$. The net effect is that the triangle with a large $H$ will have a thicker boundary layer since its thickness scales as $\delta \propto \sqrt{\nu H/U}$.[1]

---

[1]The boundary layer is proportional to $\sqrt{\nu t}$,where $t$ is the time for transverse momentum diffusion. When a constant flow speed is assumed, $t$ is proportional to the length to travel, in this case $\sim H$.
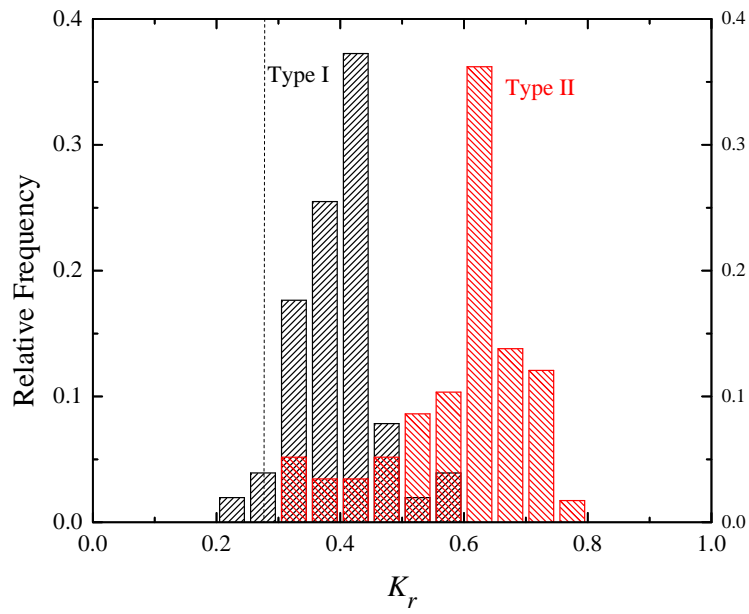
Figure 27: Kármán ratio $K_r$ of type I (black) and type II (red) vortex streets. The vertical dotted line is the classical prediction by von Kármán. Although statistical variations exist, $K_r$ of the type II is significantly higher than those of type I.
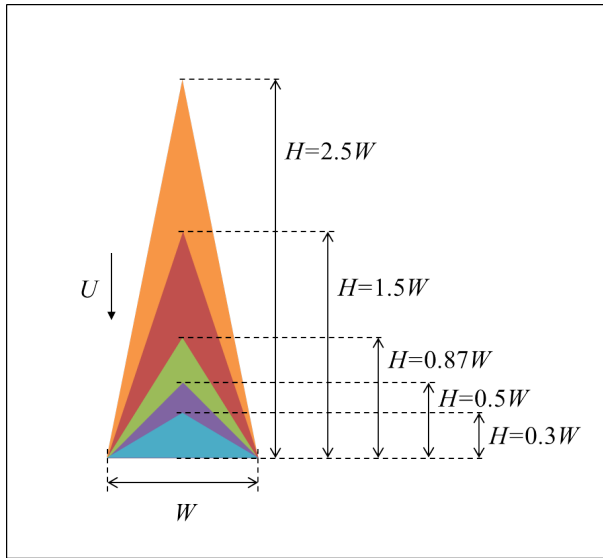
Figure 28: The cross-sectional areas of five tapered rods used in this experiment. The rods are made of titanium with a tip size $\sim 50\,\mu$m. For the same $W$, each rod has different streamwise dimension $H$, giving rise to a different boundary layer thickness $\delta$. The aspect ratio of the rods are defined as $r_a \equiv H/W$.

## 4.3 RESULTS AND DISCUSSIONS

Figure 29 shows the threshold values $Re_{C2}$ vs. the aspect ratio $r_a$. It is found that a triangle of smaller $r_a$ will shed the type II vortex street at a lower Re. For instance a rod of $r_a = 0.3$ has a threshold of $Re_{C2} \sim 150$ but a taller triangle with $r_a = 1.5$ requires $Re_{C2} \sim 350$. For triangles with $r_a > 2.5$, only type I vortex streets were observed, perhaps due to a unattainably large $Re_{C2}$. Since for the same base length $W$ or Re, an acute triangle occupies a larger area in the soap film, the above observation is somewhat peculiar because it shows that the smaller body is more readily producing rows of vortices that are more separated in space. For this reason, we postulate that the creation of type II vortex street may be dependent on the boundary layer thickness $\delta$ relative to $D$.

According to Prandtl's boundary-layer theory [55, 49], $\delta$ near a thin plate is given by

$$\delta = \alpha \sqrt{\frac{\nu y_1}{U}}, \tag{4.1}$$

where $y_1$ is the distance from the leading edge of the plate, and the $\alpha$ value varies depending on the definition of the boundary layer. For instance, if one defines the boundary layer thickness to be at a velocity 99% of $U$, then $\alpha \approx 5$ [75]. There is an issue about whether the Prandtl's boundary-layer theory is applicable to a soap film, where fluid flows in the film is coupled to the surrounding air [70]. Using a laser Doppler velocimeter, Rutgers *et al.* [70] measured the velocity profile near a thin plate in a soap film and showed that it could be best described by an exponential function $v(x) = U - v_1 e^{-x/l}$, which yields a linear velocity profile for $x \ll l$ and is consistent with Prandtl's prediction. A conspicuous feature of this measurement however is that the nonslip boundary condition appears to be violated since $v(0) = U - v_1 \neq 0$. The explanation in Ref. [70] is that for $x$ very close to the boundary, the laser Doppler velocimetry measurement became unreliable due to strong scattering of light. This peculiar feature aside, the boundary layer thickness can be predicted with the result $\delta = l \ln(100 v_1 / U)$. Measurements of $\delta$ as a function of $y_1$ by Rutgers *et al.* resulted in $\delta \sim y_1^{1/3}$ instead of $y_1^{1/2}$ as predicted by Eq. (4.1). In our measurement, however, we found that the boundary layer discharged from the rear end of a thin plate appears to be black, indicating that its optical property is quite different from the rest of the film. The darkness of the region may be due to surface roughness resulting from high vorticity in the boundary layer, which causes a dramatic decrease in the surface reflectivity as depicted in
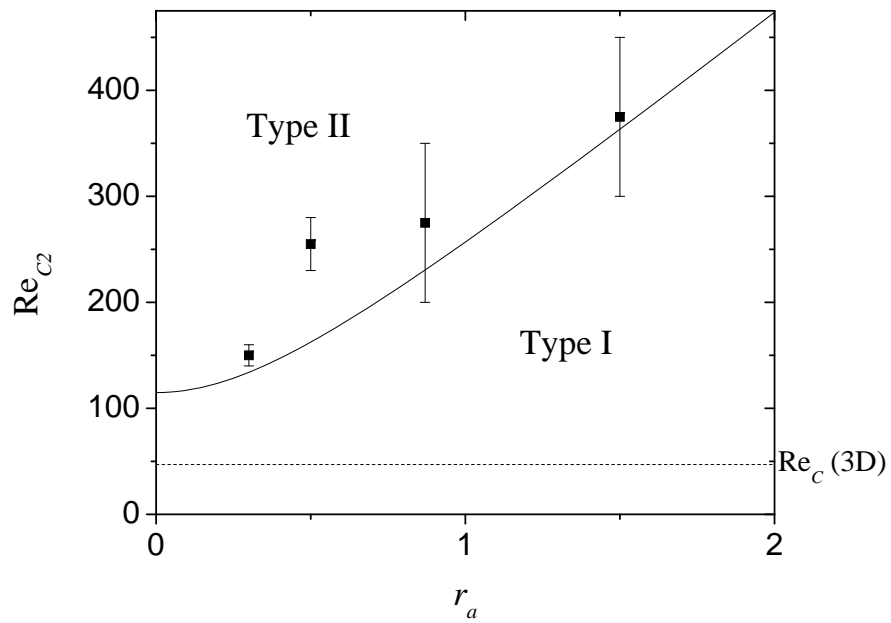
Figure 29: Onset of the type II vortex streets $Re_{C2}$ vs. the aspect ratio $r_a = H/W$. It is shown that the type II vortex streets can be generated by an obtuse triangle at a lower Reynolds number than an acute triangle. The solid line is calculated based on Eq. (4.3).

the inset of Fig. 29. We used thin plates of different $y_1$ and measured the width $2\delta_d$ of the dark region directly below the trailing edge of the plate. The data displayed in Fig. 30 show that $\delta_d$ is consistent with Eq. (4.1) and $\alpha \simeq 6$ is slightly higher than those determined in 3D fluids. In what follows we assume that Prandtl's equation [Eq. (4.1)] is valid in the soap film, and estimate the boundary layer thickness $\delta_e$ of a triangle according to

$$\delta_e = 6\sqrt{\frac{\nu L}{U}}, \tag{4.2}$$

where $L = \left[ \left( \frac{1}{2} \right)^2 + r_a^2 \right]^{\frac{1}{2}} W$ is the length of the hypotenuse of the triangle. We believe that this is an overestimate because $U$ would be greater near sharp edges of a triangle than near a flat plate.

For each triangle, the type of vortex street is plotted vs. $\delta_e/W$ in Fig. 31. As can be seen, for a triangle of $r_a = 0.3$ (black), if $\delta_e/W > 0.4$, the vortex shedding is type I (closed symbols). On the other hand, if $\delta_e/W < 0.4$, the vortex shedding is type II (open symbols). The same trend appears to be followed by other aspect ratios $r_a$ as depicted by different colored symbols. The solid line is placed at $\delta_e = 0.4W$, and it reasonably represents the boundary between the two types of vortex shedding. This suggests that the criterion for type II shedding is given by $2.5\delta_e < W$, which yields

$$\mathrm{Re}_{C2} \gtrsim 113\sqrt{1 + 4r_a^2}. \tag{4.3}$$

This equation is plotted as a solid line in Fig. 29, which shows a reasonable agreement with the experimental data.

When the type II vortex street is observed, a potential flow region that separates two rows of vortices is present. We posit that this potential flow region provides a physical barrier preventing mixing of vorticity of opposite signs. This effectively prolongs the metastability of the vortex street and allows the type II street to persist. As delineated in Fig. 26, the potential flow region appears at a certain downstream distance $s$ from the rod and persists over a distance $\Delta s$. Outside this region, the vortex street is of the first type. In particular, immediately below the potential flow region, neighboring vortices of the same sign coalesce, which significantly increases the spatial periodicity of the wake. By the vortices merging process, the vortex street transforms back to type I downstream. Figure 32 displays $s/W$ vs. $\mathrm{Re}/\mathrm{Re}_{C2}$ for rods of different $r_a$. The larger the $s/W$ value, the greater the stability of the initial type I vortex street. The graph shows that
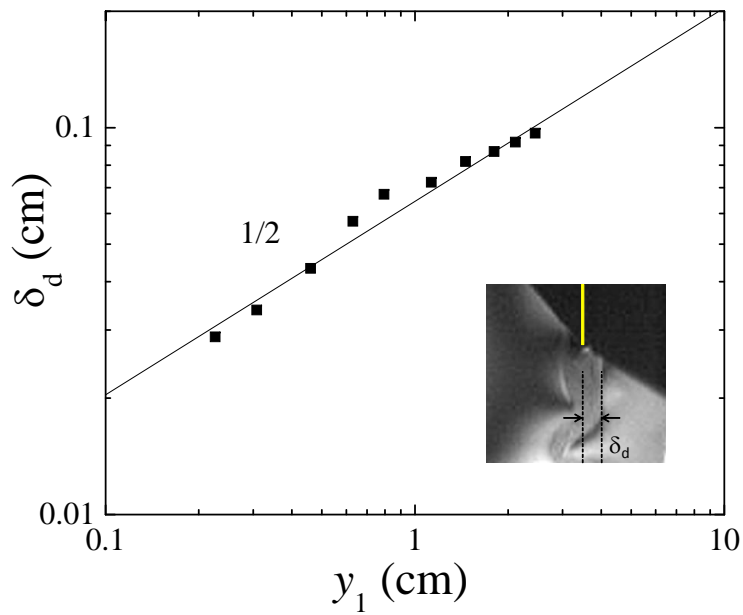
Figure 30: The thickness $\delta_d$ of the dark region observed at the trailing edge of a thin plate immersed into a soap film vs. the streamwise length $y_1$ of the plate. The Prandtl's scaling relation $\delta \sim y_1^{1/2}$ is reasonably valid over a decade. The inset is a video image showing the dark region shedding from the plate (yellow line), corresponding to $y_1 = 1.8\,\text{cm}$ and $\delta_d = 0.09\,\text{cm}$. This dark region oscillates downstream and eventually forms a vortex street.
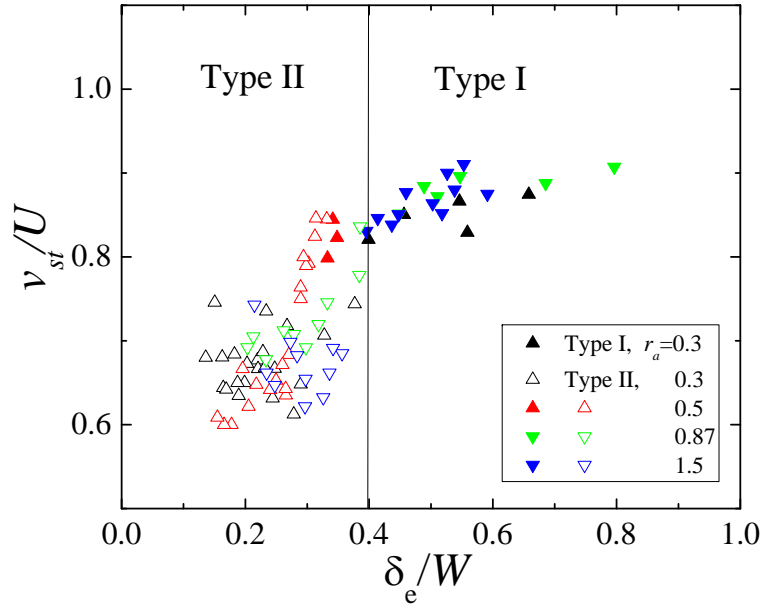
Figure 31: For triangles of different aspect ratios $r_a$, the velocity of vortex streets $v_{st}/U$ is plotted against $\delta_e/W$. Open and closed symbols represents type II and type I vortex streets, respectively. As shown by the vertical line, $\delta_e/W = 0.4$ is approximately the boundary separating the two regimes of vortex shedding. The type II vortex streets are moving much slower than type I vortex streets. This indicates that the vortices are much stronger in type II than in type I.

when $\mathrm{Re} \gg \mathrm{Re}_{C2}$, $s_{\infty}/W \simeq 4$ is approximate constant, which corresponds about one wavelength $\lambda$; namely only a pair of vortices next to the rod is present [see Fig. 26(a)]. When $\mathrm{Re} \rightarrow \mathrm{Re}_{C2}$, $s/W$ increases rapidly, and experimentally this value can be as large as 50. This suggests that type I vortex street may be stable when $\mathrm{Re} \leq \mathrm{Re}_{C2}$. In the inset, we plot $\Delta s/W$ vs. $\delta_e$, which is a measure of the stability of the type II vortex street. The figure shows that the transition to type I shedding can be significantly delayed when the boundary layer becomes thinner. Interestingly, the size $\Delta s$ seems to be mostly determined by $\delta_e$, as experimentally no strong trend is observed when $\Delta s$ is plotted against other quantities such as $\delta_e/D$ or $\mathrm{Re}/\mathrm{Re}_{C2}$, which is displayed in the inset. This indicates that the transition from type II to type I vortex street is strongly affected by the boundary layer instability. As shown in Fig. 31, $v_{st}/U$ is significantly lower for type II than for type I, and smaller $\delta_e$ yields smaller $v_{st}/U$ values, implying stronger vortices according to Eq. (3.14). It may be that when $\delta_e$ is small, the vorticity injected into the fluid never gets a chance to annihilate each other. This gives rise to more powerful vortices and consequently more persistence to the type II street. We observed that when $\delta_e$ is large, the transition to type I street occurs at $\Delta s \sim 20W$, which appears to represent the shortest potential region when the type II occurs.

An interesting feature of the type II vortex streets is that despite the two sides of the vortices are physically isolated by the irrotational region, the shedding of the clockwise and the counter-clockwise vortices is still synchronized similar to the type I street. We found that the type II vortex street emerges when the thickness of the boundary layer is thin compared to the separation distance $W$ between the two boundary layers. When this condition is not satisfied, the boundary layers from two sides of the body can mix, and a significant amount of vorticity is dissipated. Even if the criterion Eq. (4.3) is met, the phenomenon may not be possible unless the opposite signed vortices in the fluid are well isolated from each other. To a large extent, this is made possible due to the two-dimensional nature of fluid flow for which vortex stretching is not present.

## 4.4 SUMMARY

Flows behind a bluff body often result in vortex streets consisting of two rows of staggered positive and negative vortices as discussed in chapter 3 and depicted in Fig. 26(b). Here in this chapter
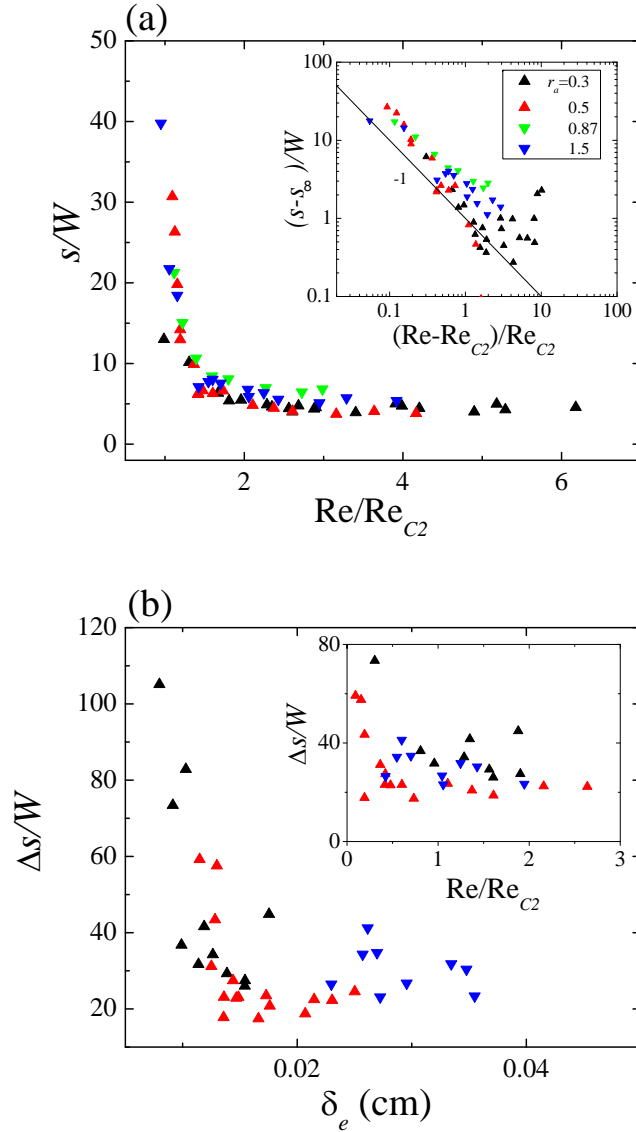
Figure 32: (a) The distance *s* from the rod to the starting point of the potential region vs. Re normalized by $Re_{C2}$. As Re increases, *s* rapidly reaches a constant value $s_\infty \sim 4W$, which is about one wavelength. It is seen that *s* becomes longer as Re is closer to the onset $Re_{C2}$, obeying a power law $(s - s_\infty)/W \propto [(Re - Re_{C2})/Re_{C2}]^{-1}$ (see the inset). In (b), the length the potential flow region $\Delta s$ is plotted against $\delta_e$. It shows that the transition to type I shedding can be delayed when the boundary layer is thinner. However, when the same quantity is plotted against Re (in the inset), no strong trend is observed.

we report that such a normal, or what we called type I, vortex street is not unique. Under certain conditions, particularly the use of inverted triangular rods, type II vortex streets can be reliably created in the flow. The type II vortex streets are characterized by their relatively large Kármán ratios $K_r$ and the metastability, which eventually leads to the more stable type I vortex streets in a far field.

Using triangular rods of different aspect ratios, we investigate this novel vortex street. Based on our observations, we postulated that the type II vortex streets are produced when (i) the boundary layer is much thinner than the width of the triangle $W$, and (ii) the two rows of counter rotating vortices are well isolated from each other due the presence of the irrotational flow region, which has the shape of a wiggling snake.

# 5.0 PRELIMINARY RESULTS ON PREDICTABILITY OF A TURBULENT FLOW IN A 2D SOAP FILM

## 5.1 INTRODUCTION

The stochastic time series is easily found in our daily life, e.g., in weather and in stock markets. Because it is important to understand such time series, there have been great interests of quantifying the chaotic behavior of these systems. There have been several proposed measures of the chaotic behavior of the system, including a Kolmogorov-Sinai entropy and a Lyapunov analysis, which are widely used.

A sample entropy (SampEn) is one of such concepts to quantify the complexity of a stochastic time series, suggested by S. Pincus [52, 53] and modified by Richman and Moorman [61]. Sample entropy is not the normal statistical entropy which is given by $-\sum p \ln p$, but rather the *information contents* of the system defined as $-\ln p$. For instance, if $p = 1$, SampEn $= 0$, meaning that there is not more information can be extracted from the system. But for $p = 0$, SampEn $= \infty$, meaning that we know nothing about the system, and there are infinite amount of information can be extracted. Specifically SampEn is defined as a negative logarithm of the conditional probability of finding a pair of identical values sharing an identical history of a certain length in a time series. As a negative logarithm of a probability, it has a positive value from 0 to infinity. When the conditional probability is 1, i.e., all subsets in a time series are identical and followed by the same value, SampEn will be 0. In the other extreme, if the conditional probability is 0, i.e., each subsets in a time series are the same but followed by different values, SampEn will be infinity. Therefore, SampEn can be thought as a measure of the (un)predictability. In the multiscale sample entropy (MSE) analysis, one calculate SampEn of a coarse-grained time series through a local averaging. Since it is introduced, the MSE analysis has been utilized in physiology such as heart beat [11, 12],

68

postural sway [57], weather forecasting [78], and stock markets prediction [45].

In this work, we present application of MSE analyses to a turbulent flow in 2D soap films, which was initiated by Dr. Matthew Shtrahman[1]. Turbulence is characterized by the emergence of many scales through bifurcation processes, and a comparison of complexities at different time scales is particularly interesting. While the full physical understanding is yet to be achieved, the calculation of the sample entropy has never been attempted in analyzing a turbulent time series.

## 5.2   EXPERIMENTAL AND COMPUTATIONAL METHODS

Our experiments were carried out in a vertically flowing soap film channel, which is identical to the one used for experiments in chapter 2. The only difference is the channel width $W$. In this experiment, two soap films, one with $W = 2\,\mathrm{cm}$ and the other with $W = 8\,\mathrm{cm}$, have been used. The flow speed $V_F$ was set to $\sim 1.5\,\mathrm{cm/s}$ for both films. The soap solution consisted of 2% of liquid detergent (Dawn, P&G) and rest of water. The viscosity of the solution was $0.012\,\mathrm{cm^2/s}$. For convenience of discussions below, a coordinate system was set such that $\hat{x}$ is transverse to the flow (spanwise direction), and $\hat{y}$ is longitudinal to the flow, which is the direction of the gravity (streamwise direction). In the soap film, turbulence was generated using a 2D grid (a comb) which was placed at $\sim 50\,\mathrm{cm}$ away from the top of the channel. The size of each tooth of the comb was $\sim 1\,\mathrm{mm}$. At a $y$ distance downstream of the comb, the velocity components $v_x$ and $v_y$ were measured as a function of time $t$ using a laser Doppler velocimeter (LDV) (TSI Scientific). The data acquisition rate was $\sim 10,000\,\mathrm{Hz}$. In what follows, we denotes velocity components as $v_{y,i}^{(W)}(t)$, where $W$ denotes the width of the soap film used, $i$ stands for either $x$ or $y$ velocity component, and $y$ is the downstream distance from the grid. The indices might be omitted when there is no possibility of confusion.

For such measured time series, we calculated the sample entropy using the measured velocity time series. The calculation has been made using a custom-made software package that is written in C. Here we will briefly discuss how calculations were carried out.

First, because LDV does not measure the velocity at an equal time interval, the measured time

---

[1]Private communication.

| Soap Film | $V_F$ | $W$ |
|:---:|:---:|:---:|
| 1 | 1.4 m/s | 2 cm |
| 2 | 1.5 m/s | 8 cm |

Table 3: Soap films used in the experiments

series first have to undergo a sampling process. Figure 33 shows an example of raw measured data as red circles. At $t \sim 0.752$ s, data points are densely populated. In contrast, at $t \sim 0.0753$ s, they are sparsely populated. To avoid statistics bias, such irregularities need be eliminated before any calculation is made. To achieve this, we used the linear interpolation scheme. We first define $t_n = n\tau_0$, where $n$ is an integer from 0 to $N$, and $\tau_0 = 0.1$ ms is the sampling time interval. We then interpolated the velocity value $v_{y,i}^{(W)}(t_n)$ using two adjacent measured data points $v_{y,i}^{(W)}(t_a)$ and $v_{y,i}^{(W)}(t_b)$, where $t_a < t_b$. Formally, this is given by

$$v(t_n) = v(t_a) + \frac{v(t_b) - v(t_a)}{t_b - t_a}(t_n - t_a), \tag{5.1}$$

where the indices are omitted. In all analysis, $N$ was set to $2^{20}$ ($\simeq 10^6$). As a result, an array of a million of entries $\{v_0, v_1, \ldots, v_{(N-1)}\}$ was constructed, where $v_n = v_{y,i}^{(W)}(n\tau_0)$.

Next, the interpolated time series are subject to a normalization process. We define the mean and the standard deviation of a time series as

$$\langle v \rangle = \frac{1}{N}\sum_{n=0}^{N-1} v_n, \tag{5.2}$$

$$\sigma[v] = \sqrt{\frac{1}{N}\sum_{n=0}^{N-1}(v_n - \langle v \rangle)^2}. \tag{5.3}$$

For each entry in a time series $v_n$, the normalization process replace $v_n$ by $(v_n - \langle v \rangle)/\sigma[v]$, and the resultant time series has $\langle v \rangle = 0$ and $\sigma[v] = 1$.
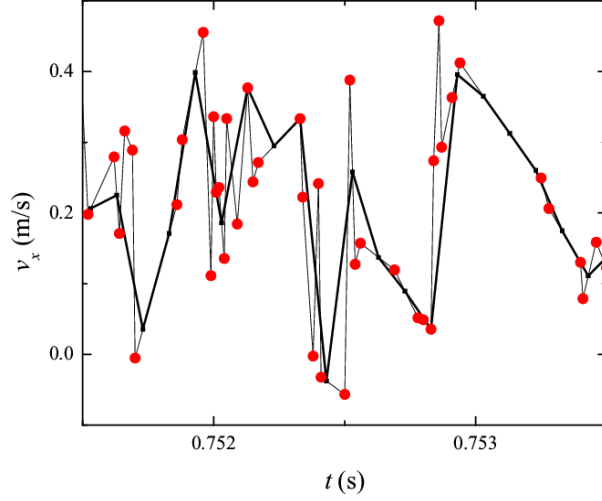
Figure 33: Raw data (red) and interpolated data (black).

Once the measured time series were interpolated and normalized, the auto-correlation function and the sample entropy were calculated. The auto-correlation function of a normalized time series is calculated in the following way,

$$\text{AutoCR}(s) = \frac{1}{N-s} \sum_{n=0}^{N-s-1} v_n v_{n+s},$$ (5.4)

where $s$ in an integer.

Next, we introduce the coarse graining time scale $\tau$. It is a dimensionless integer specifying the number of entries to be averaged over to construct a new time series. Formally, the coarse-grained time series $\left\{ v_0^{(\tau)}, v_1^{(\tau)}, \ldots, v_{N/\tau-1}^{(\tau)} \right\}$ can be constructed by local non-overlapping averaging of the original time series $\{v_0, v_1, \ldots, v_{N-1}\}$,

$$v_i^{(\tau)} = \frac{1}{\tau} \sum_{j=0}^{\tau-1} v_{i\tau+j}.$$ (5.5)

This coarse-grained time series is the one we want to use for calculating the sample entropy. The concept and detailed methods to calculate the sample entropy can be found in Ref. [52, 61]. Briefly, the sample entropy is designed to quantify the predictability of the time series. In this

71

calculation, one counts how many posteriors were repeated at a certain given prior. In a time series $\{v_0, \ldots, v_{N-1}\}$, one can find a certain subset of length $m$, $\{v_n, \ldots, v_{n+m-1}\}$, is the same to the another subset of the same length $\{v_{n+l}, \ldots, v_{n+l+m-1}\}$, i.e., $|v_{n+k} - v_{n+l+k}| < r$ for $k = 0, \ldots, m-1$, where $r$ is the tolerance. Then we define a conditional probability $p(\tau, m, r)$ that given the identical sub-strings, the immediate value that follows is also the same, i.e. $|v_{n+m} - v_{n+m+l}| < r$. The sample entropy is defined as

$$\text{SampEn}(\tau, m, r) = -\ln\left[p(\tau, m, r)\right], \tag{5.6}$$

The sample entropy can be calculated and plotted as a function of the coarse-grained time scale $\tau$, the string length $m$ or the tolerance $r$. This procedure is called a multiscale sample entropy (MSE) analysis [11, 12]. Throughout the calculations, we fix the tolerance range $r$ to be 15% of $\sigma[v]$ determined from a given time series. In practice, the selection of $r$ is limited in two ways. If $r$ is too large, there is an increasing chance of artifacts due to trivial matchings. Conversely, if $r$ is too small, there will not be enough counts for meaningful statistics. At $r = 0.15\sigma$, the variance of our sample entropy [39] becomes less than 1 % over a broad range of $\tau$, which we vary from 1 to 500 corresponding to time scales ranging from 0.1 to 50 ms. We also performed the MSE analysis by varying $m$ from 1 to 8. Unlike the coarse graining process, which acts as a low-pass filter, increasing $m$ enables us to calculate the probability of occurrence of a long sequence of events with the elementary time scales set by $\tau$.

## 5.3 RESULTS AND DISCUSSIONS

### 5.3.1 Auto-correlation functions

Figure 34 shows the velocity-velocity auto-correlation function for the 2 cm wide soap film. The auto-correlation functions for the 8 cm wide soap film are similar. We found that the auto-correlation functions of the longitudinal fluctuations decay monotonically, and those of transverse fluctuations oscillate once or twice before they fully decay. In all cases, the correlation is almost zero after $\sim 20\,\mu\text{s}$. The correlation time is longer for the time series measured at a larger $y$, with the exception of $y = 0.8\,\text{cm}$ where the turbulence is not fully developed.

72
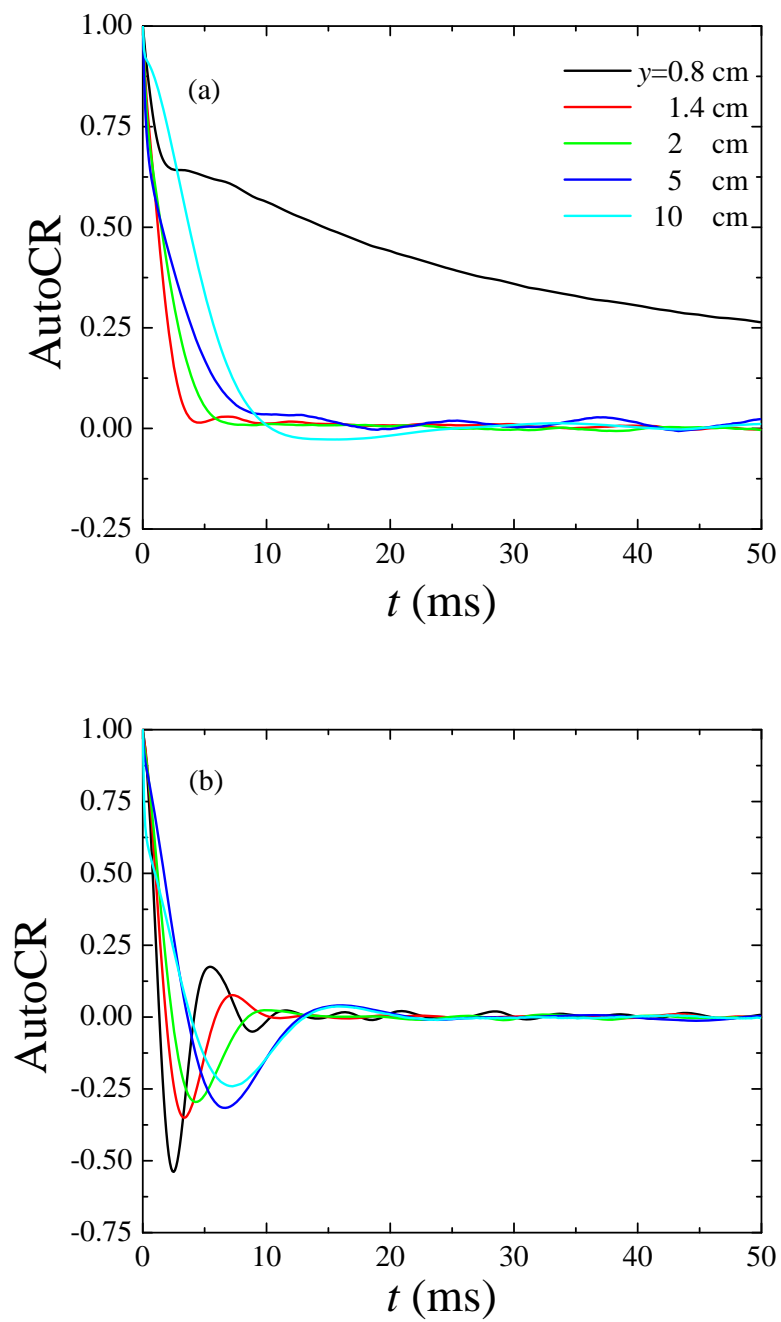
Figure 34: Auto-correlation functions of (a) the longitudinal and (b) the transverse velocity components of the 2 cm wide soap film.

### 5.3.2 Sample entropy calculation

Sample entropies of the longitudinal and transverse components of two soap films ($W = 2, 8$ cm) are displayed in Figs. 35-38. Each individual plots shows a map of the sample entropy, which depends on two parameters $\tau$ (horizontal axis) and $m$ (vertical axis). For all measurements, $N = 2^{20} = 1,048,576$ when $\tau = 1$. At $\tau = 500$, $N$ is reduced to $\sim 2000$. In the figures, a color scale was applied such that the red indicates that the time series is highly unpredictable (SampEn $\simeq 2.5$) while the blue indicates that it is more predictable (SampEn $\simeq 0.2$). It is noteworthy that the increase of $m$ reduces the number of the matching subsets, increasing the noise in the sample entropy. For example, in Fig. 35, abrupt change of colors at $m = 8$ is an artifact due to the decrease of the number of matching subsets.

Several features are interesting. First, for both films, the sample entropy for both longitudinal and transverse components increases, reaches a maximum value, and then decreases as $\tau$ increases. In case of a white noise, the sample entropy monotonically decreases as $\tau$ increase [12] due to the averaging effect in the coarse graining process. This can be understood because the time series of the velocity fluctuation in a turbulent flow is not Markovian. The flow is predictable at small time scales because at these scales the auto-correlation function is not zero. As the auto-correlation diminishes, the sample entropy increases first and then decreases due to the coarse graining averaging effect.

The second interesting feature is that the longitudinal and transverse fluctuations are clearly different. While the sample entropy of the longitudinal fluctuation changes gradually with $\tau$, the transverse one changes more abruptly. Also the transverse fluctuations have a lower value of SampEn with a broader range than the longitudinal ones. This is shown by the more extended blue colors in the plots. The observation indicates that grid turbulence in soap films is not isotropic. Such anisotropy originates from the fact that the soap film channel has a mean flow and vortices are injected in that particular direction. Therefore, the transverse time series contain complexities highly concentrated in a narrow band of $\tau$, and the band of complexity spreads to longer time scales as the downstream distance $y$ increases. This may be a reflection of an inverse energy cascade process, which is a characteristic of 2D turbulence. The location of such bands are about several milliseconds in our measurements. Reciprocally, these are several hundreds of Hertz, roughly

consistent with the frequency of the vortex shedding from the comb.

Lastly, the notion of a coherent structure must be mentioned. The transverse fluctuation of the 8 cm wide soap film (see Fig. 38) has a smaller sample entropy values at $y = 10, 13$ cm for $m > 5$ than for $m \leq 4$. This suggests that the time series may be predicted in a long term but a short term prediction may not be as accurate. Similarly, SampEn of the longitudinal fluctuation of the 2 cm wide soap film has a particularly smaller value at $y = 3, 4$ cm. These may suggest the existence of a large coherent structure in soap film turbulence.

## 5.4  SUMMARY

The multiscale sample entropy (MSE) analysis is recently used to characterize the complexity of a time series in weather forecast or physiology. We applied the MSE to our time series of velocity fluctuations in 2D turbulence in soap films. The analysis indicates that the turbulence in a soap film is two-dimensional but not isotropic. Some signs of coherent structures are observed, but its full understanding is yet to be made.

Figure 35: Sample entropies of the longitudinal velocity fluctuation of the soap film 1 ($W = 2\,\mathrm{cm}$). From the left $y = 0.8, 1.4, 2, 3\,\mathrm{cm}$ (top), $y = 4, 5, 6, 8\,\mathrm{cm}$ (middle) and $y = 10, 12\,\mathrm{cm}$ (bottom row). The sample entropies are calculated for different $\tau$ (the horizontal axis) and $m$ (the vertical axis).
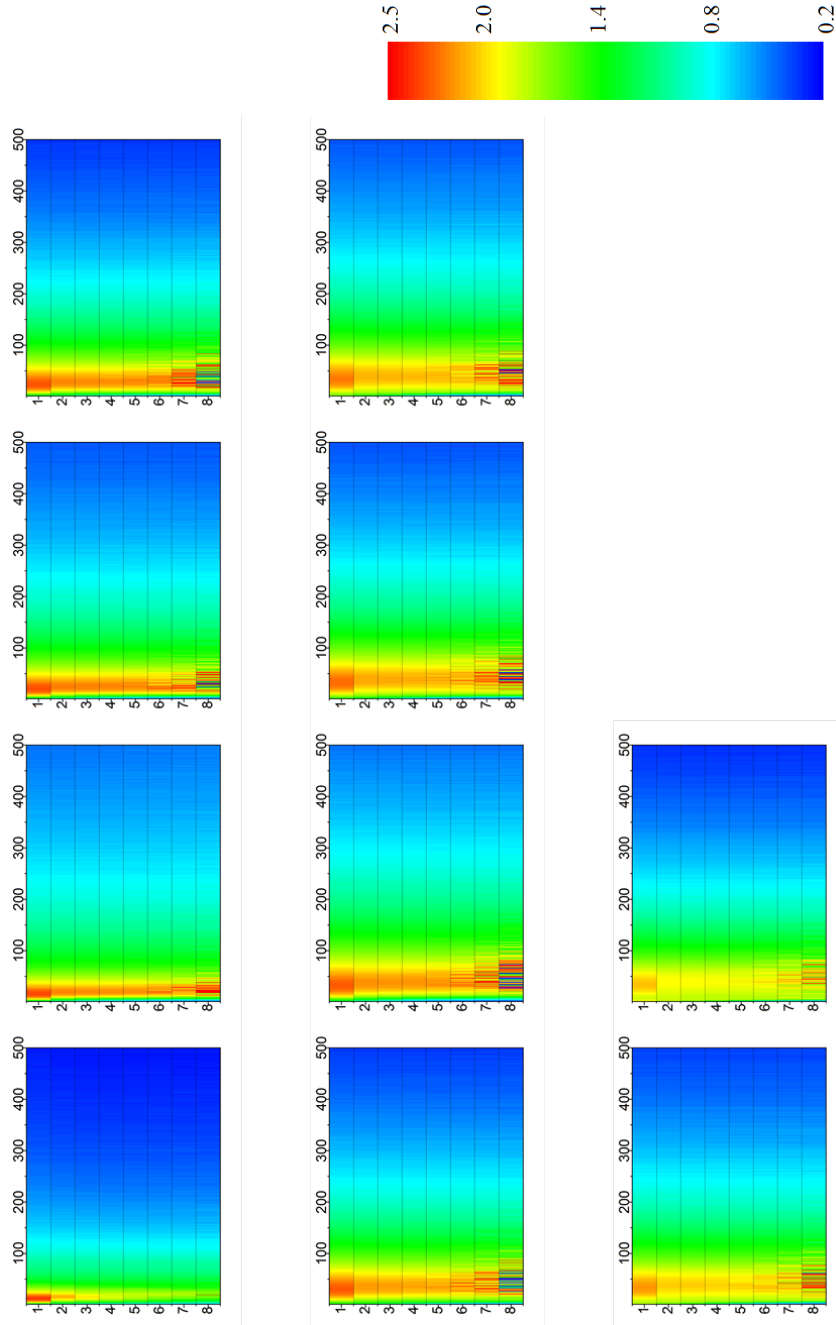
Figure 36: Sample entropies of the transverse velocity fluctuation of the soap film 1 ($W = 2$ cm). From the left $y = 0.8$, 1.4, 2, 3 cm (top), $y = 4$, 5, 6, 8 cm (middle) and $y = 10$, 12 cm (bottom row). The sample entropies are calculated for different $\tau$ (the horizontal axis) and $m$ (the vertical axis).
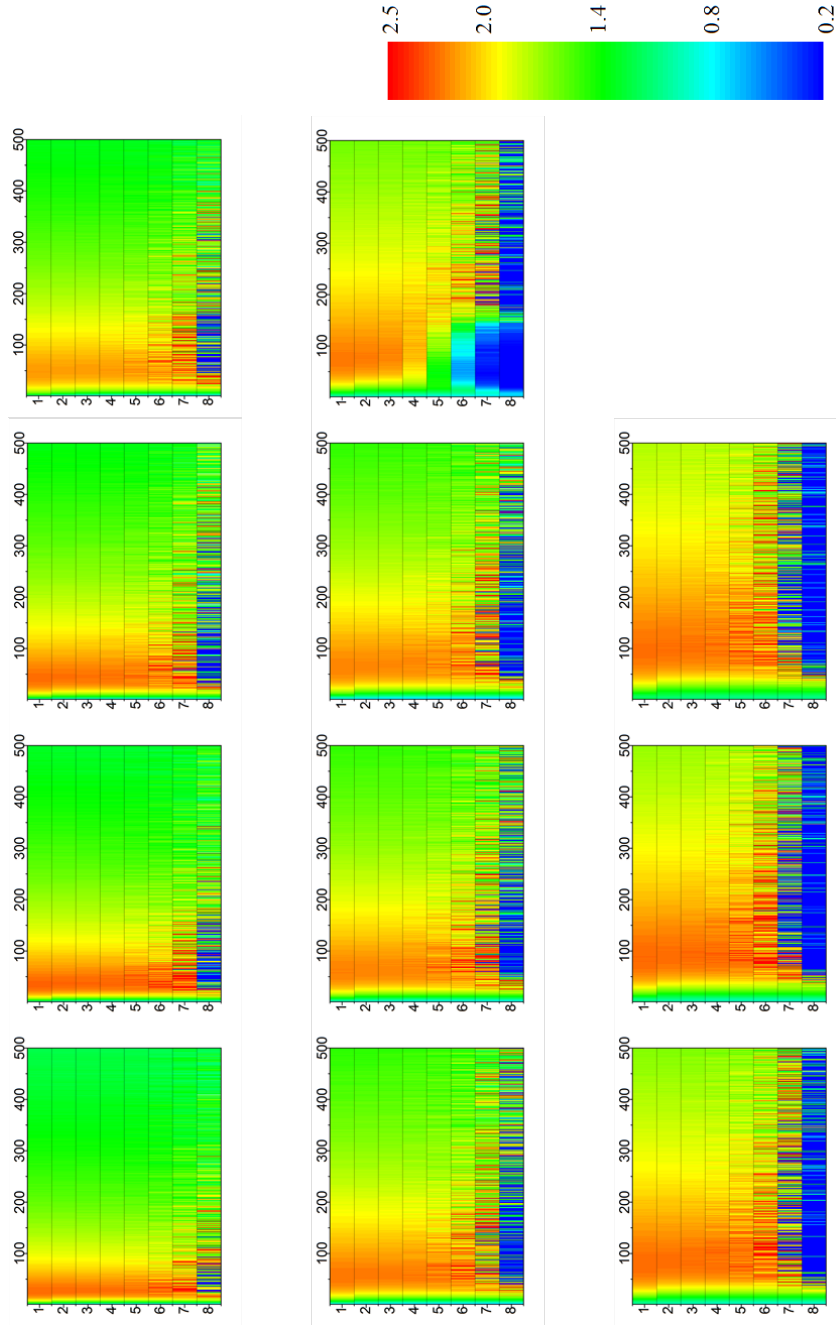
Figure 37: Sample entropies of the longitudinal velocity fluctuation of the soap film 2 ($W = 8\,\text{cm}$). From the left $y = 1, 2, 3, 4\,\text{cm}$ (top), $y = 5, 6, 7, 8\,\text{cm}$ (middle) and $y = 10, 13, 16\,\text{cm}$ (bottom row). The sample entropies are calculated for different $\tau$ (the horizontal axis) and $m$ (the vertical axis).
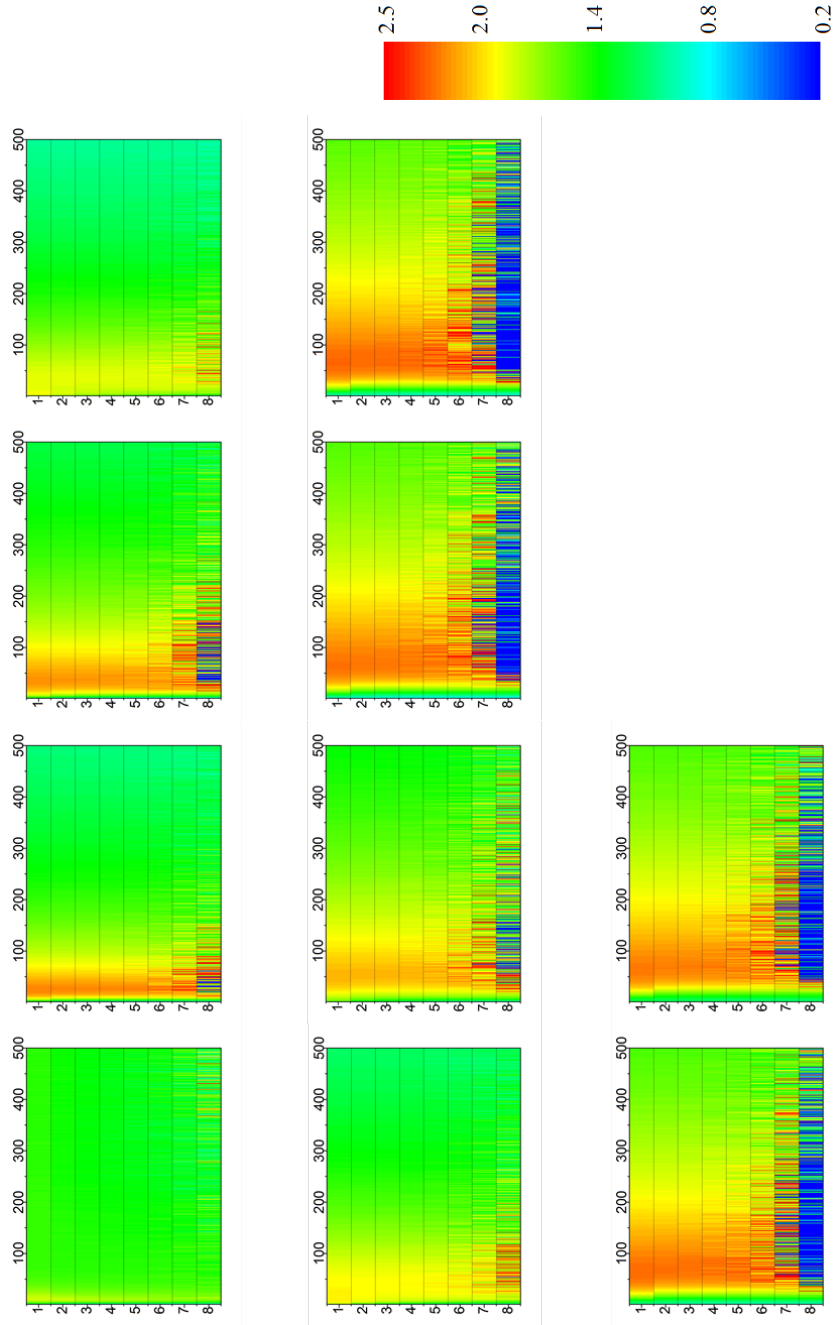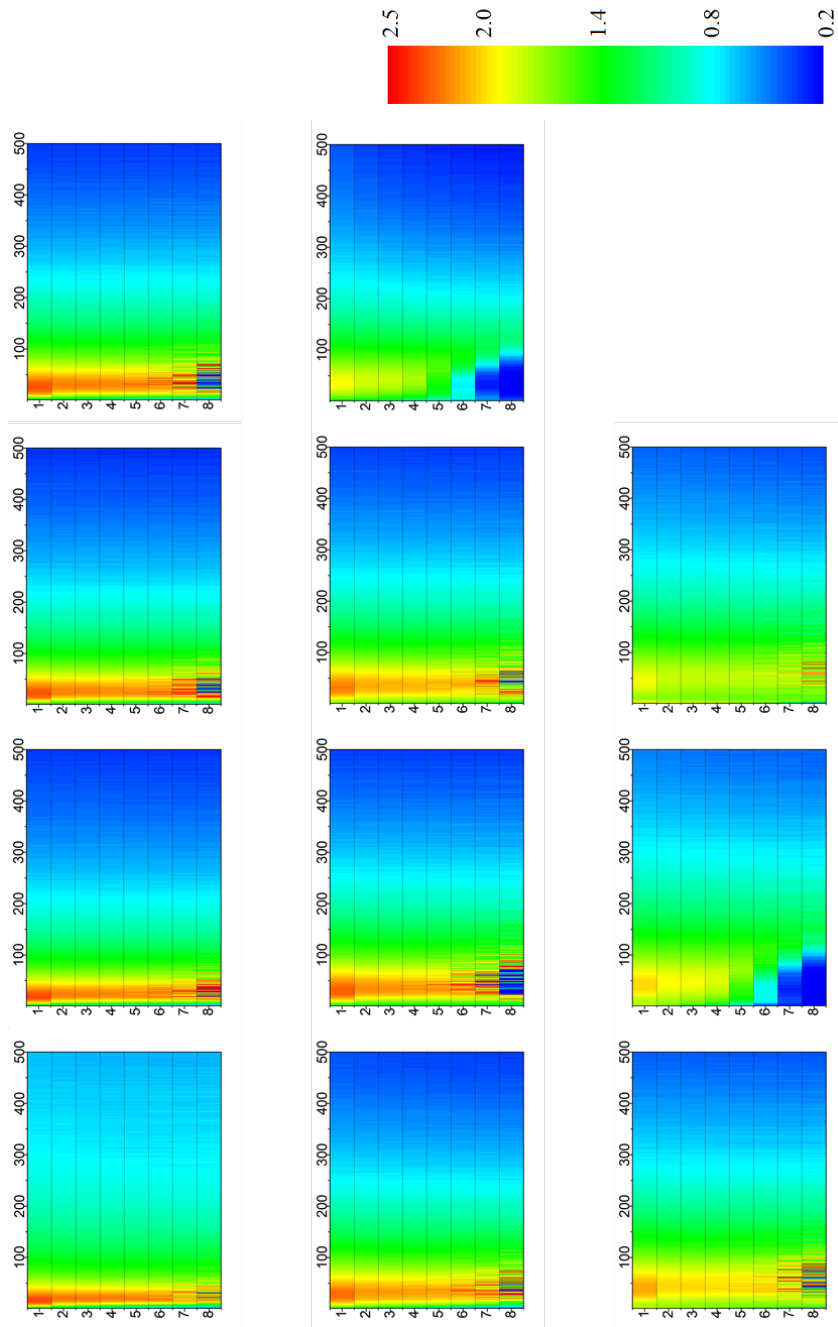
Figure 38: Sample entropies of the transverse velocity fluctuation of the soap film 2 ($W = 8$ cm). From the left $y = 1, 2, 3, 4$ cm (top), $y = 5, 6, 7, 8$ cm (middle) and $y = 10, 13, 16$ cm (bottom row). The sample entropies are calculated for different $\tau$ (the horizontal axis) and $m$ (the vertical axis).

# APPENDIX A

## PHYSICAL STRUCTURE OF A SOAP FILM

Soap molecules consist of a hydrophilic polar head and a hydrophobic hydrocarbon tail. When those molecules are resolved in water, hydrophobic tails of soap molecules tend to face air, while hydrophilic heads tend to face water [see Fig. 39(a)]. As a result, soap molecules tend to be placed at the air/water interface, and this give rise them a property of surfactants. In a soap film, surfactants exist both at the surfaces and in the interstitial fluid between two layers of surfactants [see Fig. 39(b)].

When soap molecules are formed the film structure, the surfactant concentration at the free surface $c_s$ and in the bulk liquid $c_b$ are balanced by the chemical potential of molecules. The typical relation between $c_s$ and $c_b$ is depicted in Fig. 40(a). There are two regimes of concentration in which the $c_s - c_b$ relation is differently described.

First, when the soap concentration $c_0 \equiv c_b + 2c_s/h$, where $h$ is the thickness of the film, is small, $c_s$ is linear in $c_b$ [see Fig. 40(a)]. At the same time, the surface tension $\sigma$ decreases linearly as $c_0$ increases [see Fig. 40(b)]. In this regime, the molecules are sparsely distributed on the surface, and the equation of state of molecules can be approximated as an ideal gas law.

Second, when $c_0$ is large, the linear relation no longer holds. In this regime, increasing $c_0$ increases only $c_b$ but $c_s$. In other words, $c_s$ saturates at a certain value of $c_0$, which is called the critical micelles concentration (CMC), and becomes independent of $c_b$. Above CMC, molecules start to form micelles, which is an aggregated structure with the hydrophilic heads in contact with water [see Fig. 39(c)]. In this regime, the surface tension $\sigma$ becomes constant on the change in $c_0$.

Because the surface tension of a soap film is a function of the *local* concentration of surfactant
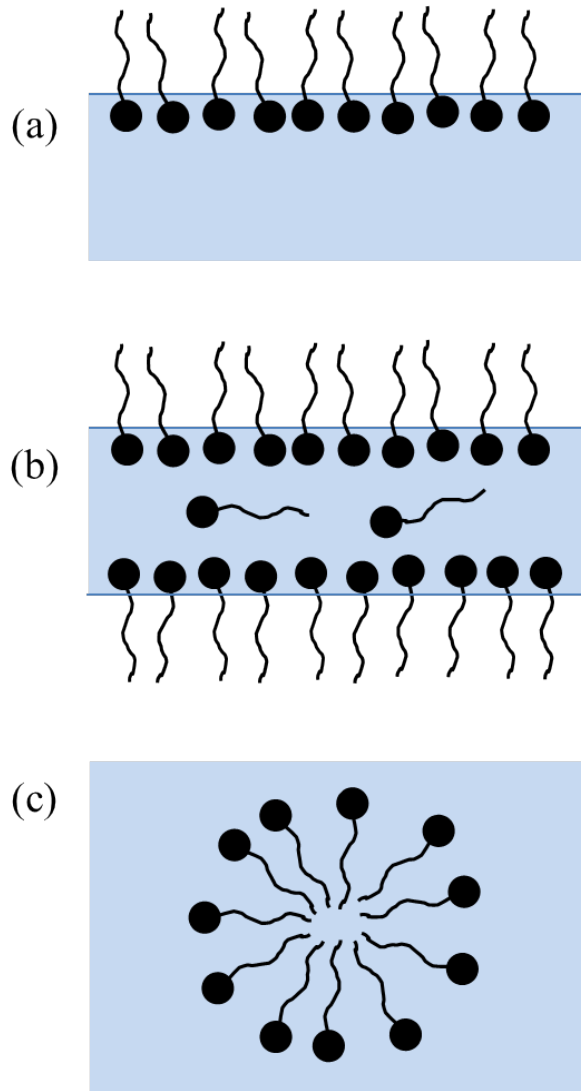
Figure 39: Possible configurations of soap molecules in water. (a) Soap molecules settle at the interface. They can form (b) the film structure and (c) micelles.
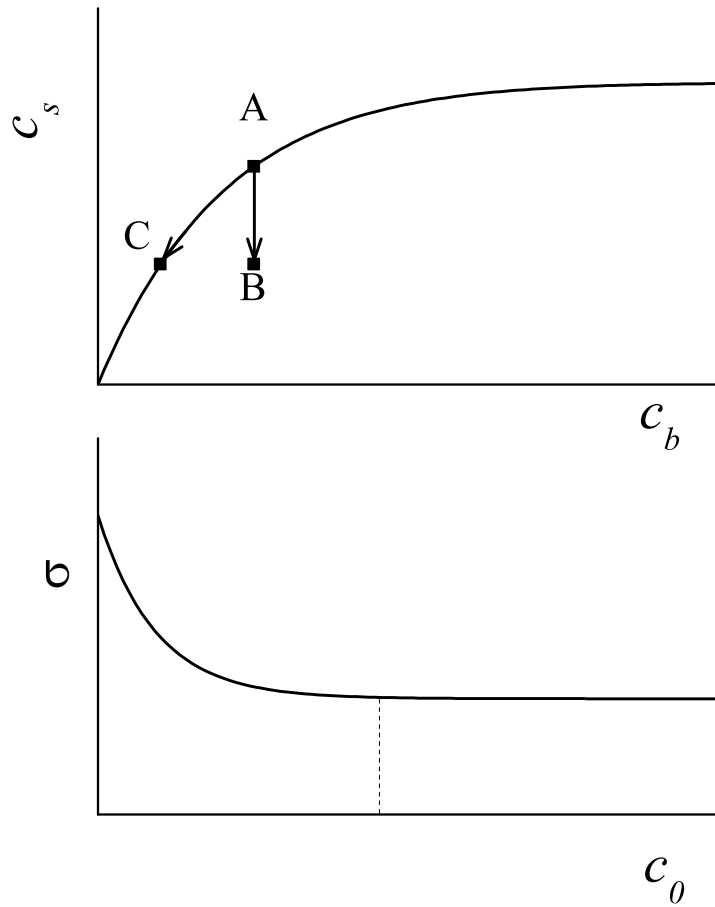
Figure 40: (a) Relation between the concentration of soap molecules at the surface $c_s$ vs. the concentration in the bulk liquid $c_b$. (b) The surface tension of the interface $\sigma$ vs. the concentration of soap $c_0$.

molecules, a soap film has elasticity and is sustainable under certain types of disturbance such as a local stretching. Depending on the time scale of the disturbance, there are two types of elasticity.

Suppose a film is in an equilibrium state, denote as a point A in Fig. 40(a). When the soap film is stretched in a time scale smaller than $\tau_D \equiv h^2/D$, where $h$ is the thickness of the film and $D$ is the diffusion coefficient, soap molecules in the bulk liquid do not have time to diffuse to the surface. Therefore, in this case, the molecules that covered a smaller area now cover a larger surface area, and $c_s$ decreases while $c_b$ is unchanged. This can be represented by the change of state from A to B in Fig. 40(a). The decrease of $c_s$ will increase the surface tension locally, providing a restoring force. This is called Marangoni elasticity and provides the stability of film under the fast disturbance. When the film is stretched slowly compared to $\tau_D$, soap molecules in the bulk liquid have enough time to diffuse to the surface. In this case $c_s$ decreases as a result of the stretching, and $c_b$ also decreases because a certain amount of molecules moved to the surface. This corresponds the change of state from A to C in the figure, and it is called Gibbs elasticity.

## BASIC EQUATIONS OF FLUID MOTION

### B.1 NAVIER-STOKES EQUATION AND THE CONSERVATION OF MASS

In a rigid body, the distance between any given two points of the body is unchanged when an external force is acting on it. As a result of it, one can consider the body as a point mass located at its center of mass [40]. The motion of any point in a rigid body is represented by that of the center of mass and the rotation about the center of mass. In a fluid[1], the situation is different. Fluid particles are moving in time, i.e., the position $\vec{x}$ of a particle in a fluid is an explicit function of time. By taking that account, the convective derivative[2] should be defined: using the chain rule of the differentiation,

$$\frac{d}{dt} = \frac{\partial}{\partial t} + \vec{v} \cdot \nabla, \tag{B.1}$$

where $\vec{v} = d\vec{x}/dt$ is the velocity of the fluid.

Using Eq. ( B.1) and the stress tensor [4], Navier-Stokes equation, the equation of a fluid motion, can be written:

$$\frac{\partial \vec{v}}{\partial t} + (\vec{v} \cdot \nabla)\vec{v} = -\frac{1}{\rho}\nabla p + \nu \nabla^2 \vec{v} + \frac{1}{\rho}\vec{f}_{ext} \tag{B.2}$$

where $\rho$, $p$ and $\nu$ are, respectively, the density, the pressure and the viscosity of the fluid, and $\vec{f}_{ext}$ is an external force acting on the fluid. The inertial term $(\vec{v} \cdot \nabla)\vec{v}$, originated from the momentum transport, is the only nonlinear term in the equation which makes the equation complex and math-

---

[1]A substance that is continually deformed under an applied stress, such as liquids, gases, plasmas, etc.

[2]There are many other names for this operator, including "material derivative", "substantial derivative", etc

ematically difficult to solve[3]. The viscous damping term on the right-hand side of the equation, $\nu\nabla^2\vec{v}$, is responsible for dissipation of energy at small scales. In general, the viscosity $\nu$ is a rank-2 tensor, however throughout this thesis, we assume it as a scalar quantity, i.e., the fluid is assumed *Newtonian*.

When the motion of fluid can be characterized by a certain length scale $D$ and velocity scale $U$, one can non-dimensionalize Eq. ( B.2) using the substitutions $\frac{\vec{v}}{U} \to \vec{v}'$, $L\nabla \to \nabla'$, $\frac{L}{U}\frac{\partial}{\partial t} \to \frac{\partial}{\partial t'}$ and $\frac{p}{\rho U^2} \to p'$, where the primed quantities are non-dimensional. Without a presence of an external force, the substitutions result in:

$$\frac{\partial \vec{v}'}{\partial t'} + \left(\vec{v}' \cdot \nabla'\right)\vec{v}' = -\nabla' p' + \frac{1}{\mathrm{Re}}\nabla'^2\vec{v}', \tag{B.3}$$

where

$$\mathrm{Re} = UD/\nu \tag{B.4}$$

is called Reynolds number[4], and it represents the relative importance of the inertial term $\left(\vec{v} \cdot \nabla\right)\vec{v}$ over the viscous damping term $\nu\nabla^2\vec{v}$, i.e., when $\mathrm{Re} \gg 1$, the inertial term is more significant than the viscous damping term, and $\mathrm{Re} \ll 1$, the viscous damping term is more significant than the inertial term.

After the non-dimensionalization process, the only remaining parameter in the Navier-Stokes equation is Re. Regardless of $U$, $D$ and $\nu$, Eq. ( B.3) remain unchanged if Re is same. This observation, by L. Rayleigh [59], was formulated as "the principle of similatude". This principle states that the non-dimensional velocity field of the fluid is expressed

$$v' = g(x', t'; \mathrm{Re}), \tag{B.5}$$

where $x' = x/D$ is the non-dimensional position vector and $g$ is a function that is determined only by Re.

Another important equation in fluid dynamics is the continuity equation, which is

$$\frac{\partial \rho}{\partial t} + \nabla \cdot (\rho\vec{v}) = 0, \tag{B.6}$$

---

[3]The existence and smoothness of its solution is unknown, and Clay Mathematics Institute has put a bounty of $1,000,000 for one to solve it.

[4]Although it was G. Stokes (1819-1903) who first introduced this concept, it is named after O. Reynolds (1842-1912) by A. Sommerfeld (1868-1951) [66].

where $\rho(\vec{x},t)$ is the density of the fluid. The continuity equation states the conservation of mass. When integrated over a volume element, the equation becomes

$$\frac{\partial}{\partial t} \int \rho \, dV = - \int (\rho \vec{v}) \cdot \hat{n} \, dA, \tag{B.7}$$

where $\hat{n}$ is an outward normal at the surface of the volume element. This states that the rate of change of mass in the volume element equals the inward flux of matter across the surface.

In general, $\rho$ is a function of $\vec{x}$ and $t$. However it is considered as a constant when the fluid is not compressible. In such a case, Eq. ( B.6) becomes

$$\nabla \cdot \vec{v} = 0, \tag{B.8}$$

which is usually called the incompressible condition.

## B.2   VORTICITY EQUATION

The vorticity of the fluid can be defined as a curl of the velocity,

$$\vec{\omega} = \nabla \times \vec{v}. \tag{B.9}$$

The vorticity equation is obtained by taking a curl on Navier-Stokes equation [Eq. ( B.2)]:

$$\frac{\partial \vec{\omega}}{\partial t} + (\vec{v} \cdot \nabla) \vec{\omega} = \nu \nabla^2 \vec{\omega} + (\vec{\omega} \cdot \nabla) \vec{v}. \tag{B.10}$$

When the external force $\vec{f}_{ext}$ in Eq. ( B.2) is conservative, its curl $\nabla \times \vec{f}_{ext}$ vanishes, and this term does not appear in the vorticity equation. Similar to Eq. ( B.2), the convective term $(\vec{v} \cdot \nabla) \vec{\omega}$ signifies the change of vorticity due to the convective transport, and $\nu \nabla^2 \vec{\omega}$ represents a dissipation. The last term of the equation, $(\vec{\omega} \cdot \nabla) \vec{v}$, is called vortex stretching and is only significant in 3D fluid. In 3D incompressible fluid, it results in the thinning of the fluid elements with vorticity due to the conservation of angular momentum, and the consequent decrease of radial length scale of the eddy, which eventually is attributed to the energy cascade in turbulence. In a 2D fluid, in contrast to a 3D

fluid, there is no vortex stretching. In that case, the motion of fluid is restricted in two-dimension, i.e., $v_z = 0$ and $\omega_x = \omega_y = 0$, the vortex stretching term vanishes:

$$(\vec{\omega} \cdot \nabla)\vec{v} = \omega_z \partial_z \vec{v} = 0. \tag{B.11}$$

The lacking of the vortex stretching in 2D makes a 2D fluid different from a 3D fluid substantially. Especially, the vortex is not weakened by stretching, a vortex persists more efficiently in 2D than in 3D.

## B.3   COMPLEX POTENTIAL OF A FLUID

In parts of a fluid where the local vorticity is zero, i.e., $\nabla \times \vec{v} = 0$, one can define a scalar function $\phi$ such that

$$\vec{v} = \nabla \phi \tag{B.12}$$

is satisfied. This scalar function $\phi$ is called a potential function. When the fluid is incompressible, i.e., the incompressible condition Eq. ( B.8) holds, one can see that $\phi$ is harmonic:

$$\nabla \cdot \nabla \phi = \nabla^2 \phi = 0. \tag{B.13}$$

Likewise, a stream function $\psi$ of a 2D fluid can be defined, in such a way that

$$\vec{v} = \nabla \times (\psi \hat{z}), \tag{B.14}$$

i.e., $v_x = \partial_y \psi$ and $v_y = -\partial_x \psi$. This definition of $\psi$ satisfies the incompressible condition of the fluid given that $\psi$ is an analytic function in 2D. Similar to $\phi$, $\psi$ is also harmonic when $\vec{v}$ is irrotational:

$$\omega_z = \partial_y v_x - \partial_x v_y = \nabla^2 \psi = 0. \tag{B.15}$$

Given that $\phi$ and $\psi$ satisfy Cauchy-Riemann condition

$$v_x = \frac{\partial \phi}{\partial x} = \frac{\partial \psi}{\partial y} \tag{B.16}$$

$$v_y = \frac{\partial \phi}{\partial y} = -\frac{\partial \psi}{\partial x}, \tag{B.17}$$

one can construct an *analytic* function

$$W(z) = \phi(z) + i\psi(z), \tag{B.18}$$

of $z = x + iy$ in a complex plane. The function $W(z)$ is called a complex potential function, and the above the Cauchy-Riemann condition assures that $\phi$ and $\psi$ are complementary. The velocity field $\vec{v} = (u, v)$ can be easily calculated using

$$u - iv = \frac{dW}{dz}. \tag{B.19}$$

The description of $W$ for several irrotational fluids is known. For example, a point vortex located at $z_0$ is described by

$$W(z) = -\frac{i\kappa}{2\pi} \log(z - z_0), \tag{B.20}$$

where $\kappa$ is the strength of the vortex. Another example is $W$ for von Kármán vortex streets. Using Eq. ( B.20), $W$ for two infinite array of vortices of strength $\kappa$ can be calculated:

$$W(z) = \frac{i\kappa}{2\pi} \log \frac{\sin \frac{\pi z}{\lambda}}{\sin \frac{\pi}{\lambda}(z - \frac{1}{2}\lambda - ih)}, \tag{B.21}$$

where $\lambda$ the longitudinal and $h$ the transverse spacing between vortices.

# APPENDIX C

# POTENTIAL FLOW

## C.1   VORTEX STREET FLOW AND POTENTIAL FLOW

This appendix is dedicated to present experimental evidences of that when Re is high (Re $\gtrsim$ 1000), the vortex street flow in a soap film channel can be treated as potential ($\vec{v} \simeq \nabla \phi$) outside small patches of vortex that occupies relatively smaller spatial regions. To show that, we observed a spinning of solid bodies in fluid. When a solid passive scalar is spinning in a fluid, the angular velocity $\Omega$ of the spinning motion is a half of the local vorticity of the fluid.

The circulation $\Gamma$ is defined as

$$\Gamma = \int \vec{\omega} \cdot d\vec{A}, \tag{C.1}$$

using $\vec{\omega} = \nabla \times \vec{v}$ and the Stokes' theorem,

$$\Gamma = \int \nabla \times \vec{v} \cdot d\vec{A} = \oint \vec{v} \cdot d\vec{l}. \tag{C.2}$$

Consider a close circular loop around a point vortex. Using $v = a\Omega$ for a solid spinner, it follows that

$$\Gamma = \omega \cdot \pi a^2 = 2\pi a v = 2\pi a \cdot a\Omega, \tag{C.3}$$

where $a$ is the radius of the loop. This yields that

$$\Omega = \frac{1}{2}\omega, \tag{C.4}$$

which relates the local vorticity of the fluid and the angular velocity of a spinning solid body.

89

Figure 41 shows the movement of two thin rectangular rotors in the fluid. The tracers, $1\text{mm} \times 1\text{mm}$ in size and $\sim 25\,\mu\text{m}$ thick, were deposited $\sim 75\,\text{cm}$ upstream of the vortex street generated by a circular rod. They reach $\gtrsim 95\%$ of the fluid velocity when they reach to the circular rod. In the figure, it is seen that the rotors does not rotate even though their trajectory is not straight. When they reach to the vicinity of a vortex patch, they start to rotate. This observation indicates that the vortex street flow is irrotational outside vortex patches of a finite size. Most of vorticity, which are originated from the boundary layer near the rods, are confined within such patches of vortex.

## C.2   POTENTIAL FLOW PAST A CIRCULAR CYLINDER

In a special circumstance in which the flow is irrotational and incompressible, a potential function of a fluid $\phi$ can be defined such as $\vec{v} = \nabla\phi$, and the potential function satisfies the Laplace equation

$$\nabla^2 \phi = 0. \tag{C.5}$$

General solution of the Eq. ( C.5) is obtained by using Green's function. Using a separation of variables, the general solution of the Laplace equation in 2-dimension is given by

$$\phi = \ln(r) + \left\{ \begin{array}{c} r^n \\ r^{-n} \end{array} \right\} \left\{ \begin{array}{c} \sin(n\theta) \\ \cos(n\theta) \end{array} \right\}, \tag{C.6}$$

where $n$ stands for a summation over integer numbers.

First let us consider a flow past a circular cylinder of radius $D$ with a flow $U_0$ at $r \to \infty$. In this example, following two boundary conditions must be satisfied by the solution:

1. $v_x = \frac{\partial \phi}{\partial x} = U_0$ at $r \to \infty$,
2. $v_r = \frac{\partial \phi}{\partial r} = 0$ at $r = D$ (slip boundary condition).

Since the flow has to have a finite velocity at infinity (the first boundary condition above), we can rule out all diverging solution except one that is proportional to $r\cos\theta$. So the solution of the problem will be reduced to

$$\phi = U_0 r \cos\theta + \sum_n A_n r^{-n} \cos(n\theta) + \sum_n B_n r^{-n} \sin(n\theta), \tag{C.7}$$
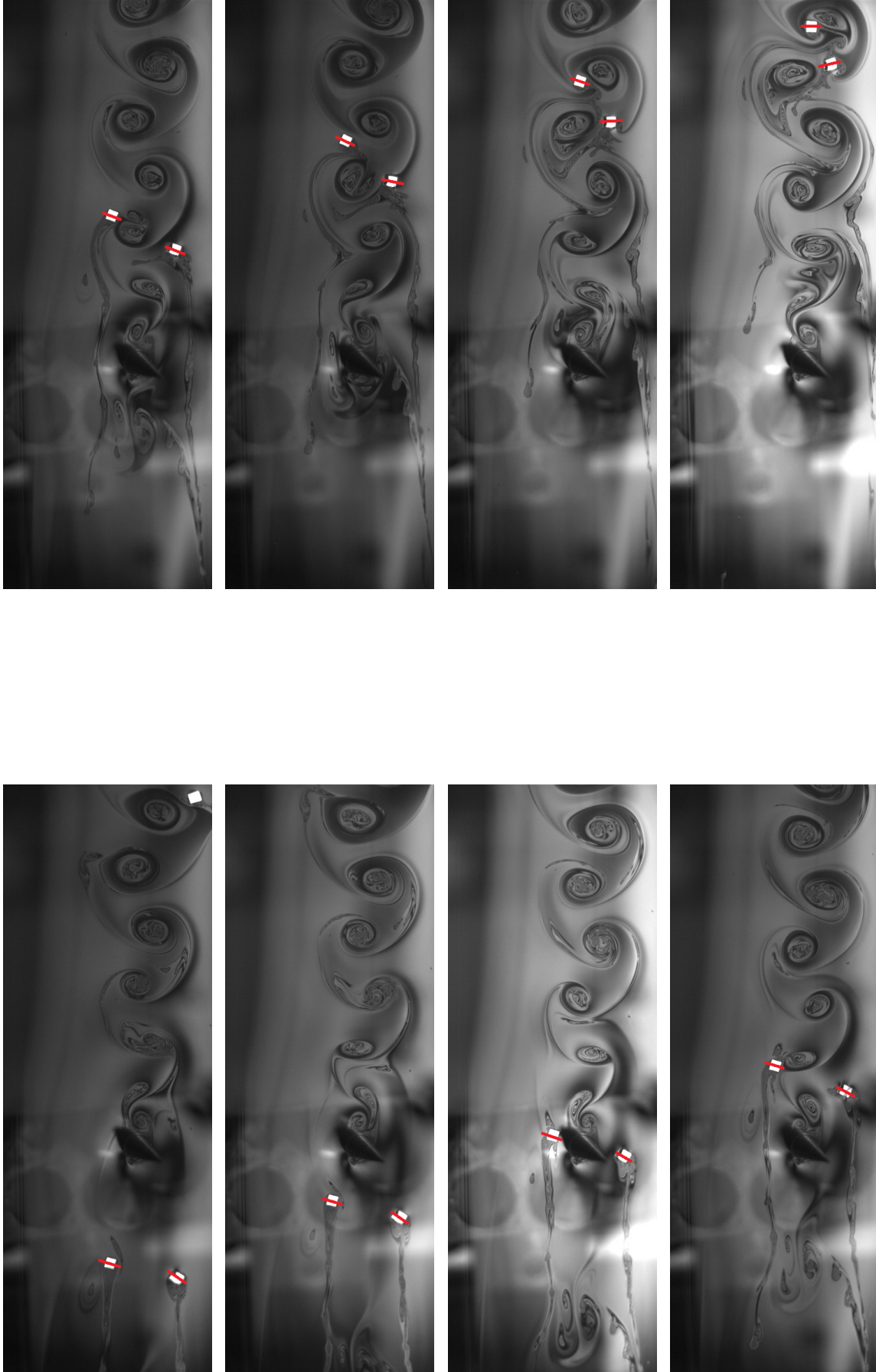
90

Figure 41: The spinning motion of a solid body immersed in the vortex street flow. (Left) from top to bottom: $t = 0, 10, 20$ and $30$ ms, (right) from top to bottom: $t = 40, 50, 60$ and $70$ ms. Two tracers does not rotate and maintain their initial orientation until $\sim 60$ ms when they touch one of vortex patches. The red marks guide eyes.

where $A_n$ and $B_n$ are coefficients to be determined.

When the mean flow is in $x$-direction, we can further consider a symmetry. In the case of the flow is $x$-axis symmetric, it is demanded that $\phi(r, \theta) = \phi(r, -\theta)$, since such a case a flow can be characterized by the properties $u_r(r, \theta) = u_r(r, -\theta)$ and $u_\theta(r, \theta) = -u_\theta(r, -\theta)$. Thus the solution has to be even for $\theta$ and this rules out all sine solutions. Now remaining part of the general solution is

$$\phi = U_0 r \cos\theta + \sum_n A_n r^{-n} \cos(n\theta). \tag{C.8}$$

A potential flow past a cylinder also a property that $u_r(r, \theta') = -u_r(r, -\theta')$ and $u_{\theta'}(r, \theta') = u_{\theta'}(r, -\theta')$ where $\theta'$ is measured from the positive $y$-axis. It is inferred that $\phi(r, \theta') = -\phi(r, -\theta')$. With the substitution $\theta' = \theta - \frac{\pi}{2}$, $\phi = U_0 r \cos\theta' \cos\frac{\pi}{2} - U_0 r \sin\theta' \sin\frac{\pi}{2} + \sum_n A_n r^{-n} \left[ \cos(n\theta') \cos(\frac{n\pi}{2}) + \sin(n\theta') \sin(\frac{n\pi}{2}) \right]$. Given that $\cos\frac{n\pi}{2} = 0$ for odd $n$ and $\sin\frac{n\pi}{2} = 0$ for even $n$, we can write as

$$\phi = -U_0 r \sin\theta' + \sum_{n=odd} A_n r^{-n} \sin(n\theta') \sin(\frac{n\pi}{2}) + \sum_{n=even} A_n r^{-n} \cos(n\theta') \cos(\frac{n\pi}{2}). \tag{C.9}$$

Since $\phi(\theta')$ is an odd function, it is demanded that $A_n = 0$ for even $n$. This symmetry doesn't hold for a shape without $y$-axis symmetry, like a triangle. Finally, the non-diverging $x$- and $y$-symmetric solution is

$$\phi = U_0 r \cos\theta + \sum_{n=odd} A_n r^{-n} \cos(n\theta). \tag{C.10}$$

The first term in Eq. ( C.10) corresponds the velocity field at the infinity, or the mean flow. Each term in the summation, $\frac{\cos(n\theta)}{r^n}$, corresponds to a multipole of order $n$ that is introduced in the flow, as they are depicted in Fig. 42. Figure 42 shows the contour plots of $\frac{\cos(\theta)}{r}$, $\frac{\cos(2\theta)}{r^2}$, $\frac{\cos(3\theta)}{r^3}$ and $\frac{\cos(5\theta)}{r^5}$, from left to right. In the $n = 1$ case, two poles - one sink and one source - are introduced. For $n = 2$, the potential function has four singularities, and this case is prohibited in our soap film flow because it breaks the symmetry. In (c) and (d), $n = 3$ and $n = 5$ cases are shown to have 6 and 10 singularities, respectively. Any potential flow in 2D can be expressed as a linear superposition of the flow induced by superimposed multipoles.

The strength of each terms can be determined by considering boundary conditions. By taking radial and azimuthal derivative of Eq. ( C.10), we get the velocity components in polar coordinate,

$$v_r = \partial_r \phi = U_0 \cos\theta - \sum_n n A_n r^{-n-1} \cos(n\theta), \tag{C.11}$$

92
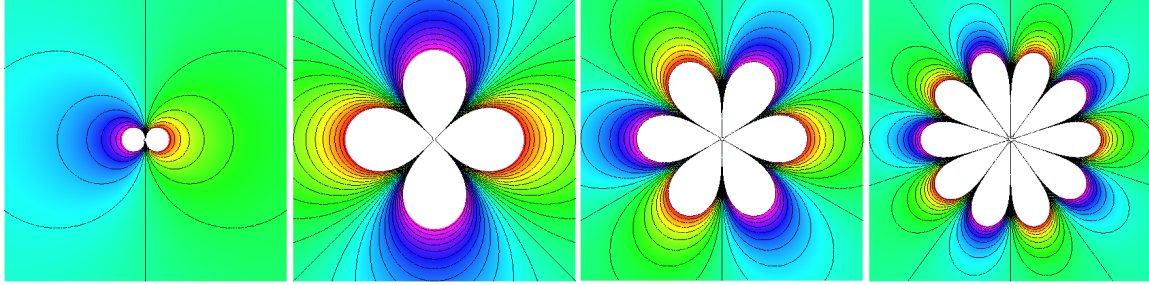
Figure 42: Equipotential lines (left to right) n=1, n=2, n=3 and n=5 modes. The flow flows from the small(blue) to large(red) value of the potential function. Not in scale.

$$v_\theta = \frac{1}{r}\partial_\theta \phi = -U_0 \sin\theta - \sum_n nA_n r^{-n-1}\sin(n\theta). \qquad (C.12)$$

In the case of the flow past a circular cylinder, the boundary condition on the surface of the cylinder is $v_r = 0$ at $r = D$. By using orthogonality of the $\{\cos(n\theta)\}$, $A_n = 0$, except $A_1 = U_0 D^2$ is obtained. Thus for the flow around a circle in 2-dimension can be derived from the potential function

$$\phi = U_0 r \cos\theta + U_0 D^2 \frac{\cos\theta}{r}. \qquad (C.13)$$

For flow past a circular cylinder of radius 0.5 (diameter 1), $D^2 = 1/4$.

## C.3   POTENTIAL FLOW PAST A NON-CIRCULAR CYLINDER

**Diamond shape:**

We consider the same Laplace equation, but with a different boundary condition from the previous section. The circular cylinder is replaced by a diamond cylinder, and this changes the boundary condition to the following:

1. The mean flow is in $\hat{x}$-direction: $\phi(r \to \infty) = U_0 r \cos\theta$,

2. The normal velocity around a diamond, placed at the origin, is zero.

93

We will use the same non-diverging $x$- and $y$-symmetric general solution that Eq. ( C.10) and the velocity components Eq. ( C.11) and Eq. ( C.12). So far only the first boundary condition is satisfied.

Since we applied $x$-axis symmetry already, we can consider only two boundary of the diamond: $y = x + D$ for the second quadrant, $y = -x + D$ for the first quadrant, where $D$ defines the size of the diamond. Those boundaries are $r = \frac{D}{\sin\theta - \cos\theta}$, $\pi/2 \leq \theta < \pi$, $r = \frac{D}{\sin\theta + \cos\theta}$, $0 \leq \theta < \pi/2$, respectively, in the polar coordinate.

The boundary conditions demand that the normal velocity across each segment of the shape has to be zero. In the first quadrant,

$$\vec{v} \cdot \hat{n} = \nabla\phi \cdot \frac{(\hat{i} + \hat{j})}{\sqrt{2}} = \left( U_0 \cos\theta - \sum_{n=odd} nA_n r^{-n-1} \cos(n\theta) \right) \cdot \left( \frac{\hat{r} \cdot \hat{i} + \hat{r} \cdot \hat{j}}{\sqrt{2}} \right) \quad \text{(C.14)}$$

$$+ \left( -U_0 \sin\theta - \sum_{n=odd} nA_n r^{-n-1} \sin(n\theta) \right) \cdot \left( \frac{\hat{\theta} \cdot \hat{i} + \hat{\theta} \cdot \hat{j}}{\sqrt{2}} \right) \quad \text{(C.15)}$$

$$= 0. \quad \text{(C.16)}$$

By using $\hat{r} \cdot \hat{i} = \cos\theta$, $\hat{r} \cdot \hat{j} = \sin\theta$, $\hat{\theta} \cdot \hat{i} = -\sin\theta$ and $\hat{\theta} \cdot \hat{j} = \cos\theta$,

$$\vec{v} \cdot \hat{n} = \frac{U_0}{\sqrt{2}} - \sum_{n=odd} nA_n r^{-n-1} \frac{\cos\left[(n+1)\theta\right] + \sin\left[(n+1)\theta\right]}{\sqrt{2}}. \quad \text{(C.17)}$$

Once we put the boundary equation $r = \frac{D}{\sin\theta + \cos\theta}$, and using $\sin\theta + \cos\theta = \sqrt{2}\sin(\theta + \pi/4)$, the equation becomes

$$\frac{U_0}{\sqrt{2}} - \sum_{n=odd} nA_n \frac{1}{D'^{n+1}} \sin^{n+1}\left(\theta + \frac{\pi}{4}\right) \sin\left[(n+1)\theta + \frac{\pi}{4}\right] = 0 \text{ for } 0 < \theta < \pi/2, \quad \text{(C.18)}$$

where $D' = D/\sqrt{2}$. We can do a similar calculation for a boundary in the second quadrant, and get

$$-\frac{U_0}{\sqrt{2}} - \sum_{n=odd} nA_n \frac{1}{D'^{n+1}} \sin^{n+1}\left(\theta - \frac{\pi}{4}\right) \sin\left[(n+1)\theta - \frac{\pi}{4}\right] = 0 \text{ for } \pi/2 < \theta < \pi. \quad \text{(C.19)}$$

Finally, a proper set of $A_n$s which satisfies above two equations should be computed numerically.

**Square shape:**

A square shape is bounded by, in a polar coordinate,

$$r\cos\theta = D, -\frac{\pi}{4} \le \theta < \frac{\pi}{4} \tag{C.20}$$

$$r\sin\theta = D, \frac{\pi}{4} \le \theta < \frac{3\pi}{4} \tag{C.21}$$

$$r\cos\theta = -D, \frac{3\pi}{4} \le \theta < \frac{5\pi}{4} \tag{C.22}$$

$$r\sin\theta = -D, \frac{5\pi}{4} \le \theta < \frac{7\pi}{4}. \tag{C.23}$$

Each boundary has the surface normal of $\hat{i}$, $\hat{j}$, $-\hat{i}$ and $-\hat{j}$.

We start from the non-diverging and symmetric solution in Eq. (C.6). Because of the symmetry, we only need to consider only two boundaries, i.g., boundaries from $-\frac{\pi}{4} \le \theta < \frac{3\pi}{4}$ would be enough to cover the whole space. Using similar arithmetic for the diamond case, boundary conditions demands

$$0 = U_0 - \sum_{n=odd} nA_n \frac{1}{D^{n+1}} \cos[(n+1)\theta] \cos^{n+1}\theta \text{ for } -\frac{\pi}{4} \le \theta < \frac{\pi}{4}, \tag{C.24}$$

$$0 = \sum_{n=odd} nA_n \frac{1}{D^{n+1}} \sin[(n+1)\theta] \sin^{n+1}\theta \text{ for } \frac{\pi}{4} \le \theta < \frac{3\pi}{4}. \tag{C.25}$$

Also, a proper set of $A_n$s which satisfies both above two equations should be computed.

## C.4 NUMERICAL SOLUTIONS

For a circular cylinder, there exists an exact solution. The solution is

$$\phi_{circle} = U_0 \left[ r\cos\theta + 0.25\frac{\cos\theta}{r} \right], \tag{C.26}$$

when the diameter of the cylinder is 1.

For a diamond rod, coefficients in the Eqs. (C.18) and (C.19) are obtained by a nonlinear regression. The result is

$$\begin{aligned}
\phi_{diamond} = {} & \phi_{circle} + U_0 \left[ -0.0019 \times \frac{\cos 3\theta}{r^3} + 0.00055 \times \frac{\cos 5\theta}{r^5} \right. \\
& \left. -8.3 \times 10^{-6} \times \frac{\cos 7\theta}{r^7} + 2.8 \times 10^{-6} \times \frac{\cos 9\theta}{r^9} + \dots \right].
\end{aligned} \tag{C.27}$$
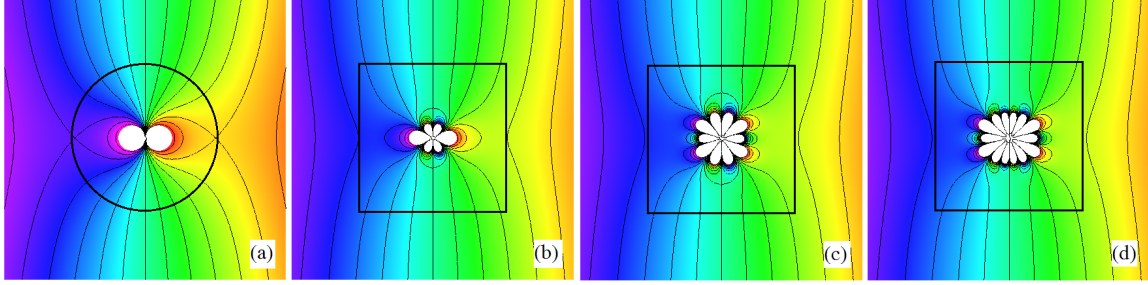
Figure 43: Equipotential lines of (a) $\phi_{circle}$ and $\phi_{square}$ with the series truncated at (b) $n = 3$, (c) $n = 5$ and (d) $n = 7$.

For a square cylinder, a similar analysis can be done for coefficients in Eqs. ( C.24) and ( C.25).

$$
\begin{aligned}
\phi_{square} \quad = \quad & \phi_{circle} + U_0 \left[ +0.052 \times \frac{\cos 3\theta}{r^3} - 0.0023 \times \frac{\cos 5\theta}{r^5} \right. \\
& \left. + 0.0045 \times \frac{\cos 7\theta}{r^7} - 0.00037 \times \frac{\cos 9\theta}{r^9} + \ldots \right].
\end{aligned} \tag{C.28}
$$

Figure 43 shows equipotential lines for a flow past (a) a circular cylinder and (b)-(d) a square cylinder. The potential flow near a circular cylinder is the superposition of the mean flow and the dipolar flow which is depicted in Fig. 43(a). The potential flow near a square cylinder, unlike the circular one, contains higher order poles. Figure 43(b) shows the potential flow near a square cylinder when it is summed up to the hexapolar term ($n = 3$). In (c) and (d), $n = 5$ and $n = 7$ terms are added to the flow, respectively. However the strength of such multipolar terms are weaker compared to the dipolar term, the flow pattern is similar to the flow near the circular cylinder.

# Bibliography

[1] http://earthobservatory.nasa.gov.

[2] L. Davidson Ahmad Sohankar, C. Norberg. Simulation of three-dimensional flow around a square cylinder at moderate reynolds numbers. *Physics of Fluids*, 11:288, 1999.

[3] G. R. Baker, S. J. Barker, K. K. Bofah, and P. G. Saffman. Laser anemometer measurements of trailing vortices in water. *J. Fluid Mech.*, 65:325, 1974.

[4] G. K. Batchelor. *An Introduction to Fluid Dynamics*. Cambridge Press, 1967.

[5] A. Belmonte, W. I. Goldburg, H. Kellay, M. A. Rutgers, B. Martin, and X. L. Wu. Velocity fluctuations in a turbulence soap film: The third moment in two dimensions. *Phys. Fluids*, 11:1196, 1999.

[6] E. Berger. Die bestimmung der hydrodynamischen grössen einen karmanshen wirbelstrausse aus hitzdrahtemesssungen. *Z. Flugwiss*, 12:41, 1964.

[7] G. Birkhoff. Formation of vortex streets. *J. Appl. Phys.*, 24:98, 1953.

[8] H. M. Blackburn and R. D. Henderson. A study of two-dimensional flow past an oscillating cylinder. *Journal of Fluid Mechanics*, 386:255, 1999.

[9] Phillip P. Brown and Desmond F. Lawler. Sphere drag and settling velocity revisited. *Journal of Environmental Engineering*, 129:222, 2003.

[10] S. Chandrasekhar. *Hydrodynamics and Hydromagnetic Stability*. Dover, 1981.

[11] M. Costa, Ary L. Goldberger, and C.-K. Peng. Multiscale entropy analysis of complex physiologic time series. *Phys. Rev. Lett.*, 89:068102, 2002.

[12] M. Costa, Ary L. Goldberger, and C.-K. Peng. Multiscale entropy analysis of biological signals. *Phys. Rev. E*, 71:021906, 2005.

[13] Y. Couder. Two-dimensional grid turbulence in liquid film. *J. Phys. (Paris), Lett.*, 45:L353, 1984.

[14] Y. Couder, J. M. Chomaz, and M. Rabaud. On the hydrodynamics of soap films. *Physica D*, 37:384, 1989.

[15] Y. Couder, E. Fort, C.-H. Gautier, and A. Boudaoud. From bouncing to floating: Noncoalescence of drops on a fluid bath. *Phys. Rev. Lett.*, 94:177801, 2005.

[16] L. Courbin and H. A. Stone. Impact, puncturing, and the self-healing of soap film. *Phys. Fluids*, 18:091105, 2006.

[17] C. P. Cox. Statistical principles for the line of best fit. *Laboratory Practice*, 1963.

[18] Jean Le Rond d'Alambert. *Essai d'une nouvelle théorie de la résistance des fluides*. 1752.

[19] Jean Le Rond d'Alambert. Memoir xxxiv. *Opuscules Mathématiques*, 5:132, 1768.

[20] M. E. Davies. A comparison of the wake structure of a stationary and oscillating bluff body, using a conditional averaging technique. *J. Fluid Mech.*, 75:209, 1976.

[21] P. G. Drazin and W. H. Reid. *Hydrodynamic Stability*. Cambridge.

[22] H. E. Edgerton and J. R. Killian. *Flash!* Hale, Cushman, and Flint, Boston, 1939.

[23] P. Engels. Observing the dance of a vortex-antivortex pair, step by step. *Physics*, 3:33, 2010.

[24] J. Nilsson et al. *Proc. μTAS 2001, Monterey, Canada*, page 75, 2001.

[25] Neil Schlager et al. *When Technology Fails: Significant Technological Disasters, Accidents, and Failures of the Twentieth Century*. Gale Research Inc, Detroit, 1986.

[26] A. Fage and F. C. Johansen. *Aero. Res. Ctee., Rep. and Mem.*, No. 1104, 1927.

[27] A. Fage and F. C. Johansen. *Phil. Mag.*, 5:417, 1928.

[28] U. Fey, Michael Konig, and Helmut Eckelmann. A new strouhal-reynolds number relationship for the circular cylinder in the range $47 < \mathrm{Re} < 2 \times 10^5$. *Phys. Fluids*, 10:1547, 1998.

[29] E. Hecht. *Optics*. Addison Wesley, 3rd edition edition, 1998.

[30] R. D. Henderson and D. Barkley. Secondary instability in the wake of a circular cylinder. *Physics of Fluids*, 8:1683, 1996.

[31] S. G. Hooker. On the action of viscosity in increasing the spacing ratio of a vortex street. *Proc. Roy. Soc. London A*, 154:67, 1936.

[32] Huosheng Hu. Biologically inspired design of autonomous robotic fish at essex. In *Proceedings of the IEEE SMC UK-RI Chapter Conference 2006 on Advances in Cybernetics Systems*, Sheffield, UK, 2006.

[33] P. A. Irwin. Vortices and tall buildings: A recipe for resonance. *Phys. Today*, 63:68, 2010.

[34] J. Jackson. *Classical Electrodynamics*. Cambrige Press, 1998.

[35] D. D. Joseph. Viscous potential flow. *J. Fluid Mech.*, 479:191, 2003.

[36] C. Josserand and S. Zaleski. Droplet splashing on a thin liquid film. *Phys. Fluids*, 15:1650, 2003.

[37] Ildoo Kim and X. L. Wu. Tunneling of micron-sized droplets through soap films. *Phys. Rev. E*, 82:026313, 2010.

[38] R. H. Kraichnan. Inertial ranges in two dimensional turbulence. *Phys. Fluid*, 10:1417, 1967.

[39] Douglas E. Lake, Joshua S. Richman, M. Pamela Griffin, and J. Randall Moorman. Sample entropy analysis of neonatal heart rate variability. *American Journal Physiology: Regulatory, Integrative and Comparative Physiology*, 283:R789, 2002.

[40] L. D. Landau and E. M. Lifshitz. *Mechanics, 3/e*. Butterworth-Heinemann, 1976.

[41] J. Ledolter and R. V. Hogg. *Applied Statistics for Engineers and Physical Scientists*. Pearson, 2000.

[42] N. Y. Liang, C. K. Chan, and H. J. Choi. Dynamics of the formation of an aureole in the bursting of soap films. *Phys. Rev. E*, 54:R3117, 1996.

[43] M. T. S. Lin, L. Pulkkinen, J. Uitto, and K. Yoon. The gene gun: current applications in cutaneous gene therapy. *Int. J. Dermatol.*, 39:161, 2000.

[44] J. Lucassen, M. Van den Tempel, A. Vrij, and F. Hesselink. *Proc. K. Ned. Akad. Wet., ser. B: Phys. Sci.*, 73(2):109, 124, 1970.

[45] Esfandiar Maasoumi and Jeff Racine. Entropy and predictability in the stock market returns. *J. Econometrics*, 107:291, 2002.

[46] B. K. Martin, X. L. Wu, W. I. Goldburg, and M. A. Rutgers. Spectra of decaying turbulence in a soap film. *Phys. Rev. Lett.*, 80:3964, 1998.

[47] K. J. Mysels, K. Shinoda, and S. Frankel. *Soap Films*. Pergamon, New York, 1959.

[48] C. Norberg. An experimental inverstigation of the flow around a circular cylinder: influence of aspect ratio. *J. Fluid. Mech.*, 258:287, 1994.

[49] H. Ockendon and J. R. Ockendon. *Viscous Flow*. Cambridge Texts in Applied Mathematics, 1995.

[50] D. J. Olinger and K. R. Sreenivasan. Nonlinear dynamics of the wake of an oscillating cylinder. *Phys. Rev. Lett.*, 60:797, 1988.

[51] L. Onsager. Statistical hydrodynamics. *Nuovo Cimento Suppl.*, 6:279, 1949.

[52] S. M. Pincus. Approximate entropy as a measure of system complexity. *Proc. Natl. Acad. Sci. USA*, 88:2297, 1991.

[53] S. M. Pincus and B. H. Singer. Randomness and degrees of irregularity. *Proc. Natl. Acad. Sci. USA*, 93:2083, 1996.

[54] Fernando L. Ponta and Hassan Aref. Strouhal-reynolds number relationship for vortex streets. *Phys. Rev. Lett.*, 93:084501, 2004.

[55] L. Prandtl. Über flüssigkeitsbewegung bei sehr kleiner reibung. *Verh. III, Int. Math. Kongr., Heidelberg*, page 484, 1904.

[56] M. Provansal, C. Mathis, and L. Boyer. Benard-von karman instability : transient and forced regimes. *J. Fluid. Mech.*, 182:1, 1987.

[57] Sofiane Ramdani, Benoit Seigle, Julien Lagarde, Frederic Bouchara, and Pierre Louis Bernard. On the use of sample entropy to analyze human postural sway data. *Med. Eng. Phys.*, 31:1023, 2009.

[58] L. Rayleigh. Aeolian tones. *Philos. Mag.*, 29:433, 1915.

[59] L. Rayleigh. The principle of similatude. *Nature*, 95:66, 1915.

[60] D. Richard and D. Quéré. Bouncing water drops. *Europhysics Letters*, 50:768, 2000.

[61] J. S. Richman and J. R. Moorman. Physiological time-series analysis using approximate entropy and sample entropy. *Am. J. Physiol.: Heart. Circ. Physiol.*, 279:H2039, 2000.

[62] Rosenhead and Schwabe. *Proc. Roy. Soc. London A*, 129:115, 1930.

[63] A. Roshko. On the development of turbulent wakes from vortex streets. *NACA Report*, Report 1191, 1954.

[64] A. Roshko. On the drag and sheddding frequency of two-dimensional bluff body. *NACA Report*, Technocal Note 3169, 1954.

[65] A. Roshko. Perspectives of bluff body aerodynamics. *Journal of Wind Engineering and Industrial Aerodynamics*, 49:79, 1993.

[66] N. Rott. Note on the history of the reynolds number. *Ann. Rev. Fluid Mech.*, 22:1, 1990.

[67] P. Roushan and X. L. Wu. Structure-based interpretation of the strouhal-reynolds number relationship. *Phys. Rev. Lett.*, 94:054504, 2005.

[68] P. Roushan and X. L. Wu. Universal wake structures of kÃ¡rmÃ¡n vortex streets in two-dimensional flows. *Phys. Fluids*, 17:073601, 2005.

[69] M. Rutgers, X. L. Wu, and W. B. Daniel. Conducting fluid dynamics experiments with vertically falling soap films. *Rev. Sci. Instrum.*, 72:3025, 2001.

[70] M. A. Rutgers, X. L. Wu, R. Bhagavatula, A. A. Petersen, and W. I. Goldburg. Two-dimensional velocity profiles and laminar boundary layers in flowing soap films. *Phys. Fluids*, 8:2847, 1996.

[71] P. G. Saffman. *Vortex Dynamics*. Cambridge University Press, 1995.

[72] P. G. Saffman and J. C. Schatzman. *SIAM Journal on Scientific and Statistical Computing*, 2:285, 1981.

[73] P. G. Saffman and J. C. Schatzman. An inviscid model for the vortex-street wake. *Journal of Fluid Mechanics*, 122:467, 1982.

[74] P. G. Saffman and J. C. Schatzman. Stability of a vortex street of finite vortices. *Journal of Fluid Mechanics*, 117:171, 1982.

[75] H. Schlichting. *Boundary-Layer Theory*. McGraw-Hill Book Company.

[76] M. Sfakiotakis, D. M. Lane, and J. B. Davies. Review of fish swimming modes for aquatic locomotion. *IEEE Journal of Oceanic Engineering*, 24:237, 1999.

[77] A. Sharma and E. Ruckenstein. Finite-amplitude instability of thin free and wetting films: Prediction of lifetimes. *Langmuir*, 2:480, 1986.

[78] Li Shuangchen, Zhou Qiaofu, Wu Shaohong, and Dai erfu. *Int. J. of Climatol.*, 26:2131, 2006.

[79] V. Strouhal. Über eine besondere art der tonerregung. *Ann. Physik*, 5:216, 1878.

[80] J. L. Synge. *Proc. Roy. Irish Acad.*, 37:95, 1927.

[81] S. Taneda. Downstream development of the wakes behind cylinders. *J. Phys. Soc. Jpn.*, 11:302, 1956.

[82] G. I. Taylor. The dynamics of thin sheets of fluid. ii. waves on fluid sheets. *Proc. R. Soc. Lond. A*, 253(1274):296, 1959.

[83] G. I. Taylor and D. H. Michael. On making holes in a sheet of fluid. *J. Fluid Mech.*, 58:625, 1973.

[84] S. T. Thoroddsen. The ejecta sheet generated by the impact of a drop. *J. Fluid Mech.*, 451:373, 2002.

[85] Milton van Dyke. *An Album of Fluid Motion 12/e*. Parabolic Press, 2008.

[86] Th. von Kármán. Über den mechanismus des widerstandes, den ein bewegter körper in einer flüssigkeit erfährt. *Göttinger Nachr.*, page 509, 1911.

[87] Th. von Kármán. *Physik. Z.*, 13:49, 1912.

[88] Theodore von Karman. The wind and beyond. In *Pioneer in Aviation and Pathfinder in Space*, pages 61–65. Little, Brown and Company, 1967.

[89] P. Vorobieff, M. Rivera, and R. E. Ecke. Soap film flows: Statistics of two-dimensional turbulence. *Phys. Fluids*, 11:2167, 1999.

[90] D. A. Weiss and A. L. Yarin. Single drop impact onto liquid films: neck distortion, jetting, tiny bubble entrainment, and crown formation. *J. Fluid Mech.*, 385:229, 1999.

[91] C. H. K. Williamson. Defining a universal and continuous strouhal-reynolds number relationship for the laminar vortex shedding of a circular cylinder. *Phys. Fluids*, 31:3165, 1988.

[92] C. H. K. Williamson. Vortex dynamics in the cylinder wake. *Ann. Rev. Fluid Mech.*, 48:477, 1996.

[93] C. H. K. Williamson and G. L. Brown. A series in $1/\sqrt{Re}$ to represent the strouhal-reynolds number relationship of the cylinder wake. *J. Fluids Struct.*, 12:1073, 1998.

[94] C. H. K. Williamson and R. Govardhan. Vortex induced vibrations. *Ann. Rev. Fluid Mech.*, 36:413, 2004.

[95] X. L. Wu, R. Levine, M. Rutgers, H. Kellay, and W. I. Goldburg. Infrared technique for measuring thickness of a flowing soap film. *Rev. Sci. Instrum.*, 72:2467, 2001.

[96] L. Xu. Liquid drop splashing on smooth, rough, and textured surfaces. *Phys. Rev. E*, 75:056316, 2007.

[97] L. Xu, W. W. Zhang, and S. R. Nagel. Drop splashing on a dry smooth surface. *Phys. Rev. Lett.*, 94:184505, 2005.

[98] Hong-Quan Zhang, Uwe Fey, Bernd R. Noack, Michael König, and Helmut Eckelmann. On the transition of the cylinder wake. *Phys. Fluids*, 7:779, 1994.

[99] R. Zheng and T. A. Witten. Feasibility of large free-standing liquid films in space. *Phys. Rev. E*, 74:051602, 2006.